THE RECOIL PROTON POLARIZATION IN π^- PHOTOPRODUCTION FROM DEUTERIUM BETWEEN 450 AND 950 MeV AND A PARTIAL WAVE ANALYSIS OF $\gamma n \rightarrow \pi^- p$ IN THE RESONANCE REGION

Thesis by

William J. Metcalf

In Partial Fulfillment of the Requirements

For the Degree of

Doctor of Philosophy

California Institute of Technology

Pasadena, California

1974

(Submitted February 20, 1974)

ACKNOWLEDGMENTS

I would like to express my deep appreciation for the advice and support of Professor R. L. Walker during this research. He not only helped with the analysis of the experiment, but he is also responsible for much of the knowledge that I possess about pion photoproduction. The phenomenological analysis in this thesis is largely due to work carried out in collaboration with Prof. Walker and this joint research has been an especially rewarding experience for me.

Leon Rochester deserves special credit for the experiment described in this thesis. Without his instigation and hard work during the early stages this experiment would never have been performed. Pat Walden and Paul Scheffler, who performed a π^- cross section experiment in conjunction with the present experiment, are responsible for much of the apparatus used as well as much of the analysis of deuterium and background effects. I will always appreciate their friendship as well as their contribution to the present experiment. During the analysis stages of this work the author has benefitted from many helpful discussions with Prof. Alexander Firestone, Joel Mellema, and especially with Bruce Winstein who gave freely of his time in explaining many of the features of the polarization analysis.

In addition to Pat Walden and Paul Scheffler, I wish to acknowledge the assistance of Gary Murata and Chip Smith during the running of this experiment. To the entire crew of the synchrotron laboratory, especially Al Neubieser and Earle Emery, go my special thanks for keeping the accelerator running smoothly and maintaining

the deuterium target. Also, I would like to express my appreciation to my scanners, headed by Mike Curtis, for their efforts on my behalf.

For financial support I am indebted to the Atomic Energy Commission, the California Institute of Technology, and to NDEA and California State Fellowships.

I would like to thank my parents for their encouragement and to express my deep and sincere appreciation for the encouragement and the very real contributions to this work given by my wife, Jane.

ABSTRACT

In an experiment performed at the Caltech synchrotron the recoil proton polarization in the reaction $\gamma n \rightarrow \pi^- p$ has been measured at CM pion angles of 90° and 120° in the region from 450 to 900 MeV in lab photon energy. A deuterium target was used and the observed reaction $\gamma d \rightarrow \pi^- pp$ was related to $\gamma n \rightarrow \pi^- p$ by a simple spectator model. The polarization was determined from the distribution in the azimuthal scattering angle, ϕ, of the recoil protons from carbon in a range-scattering chamber consisting of alternate spark gaps and carbon plates. A maximum likelihood method was used to extract the polarization from the observed ϕ distribution of the p-C scatters. The π^- coincident with the recoil proton was detected in a magnetic spectrometer where its momentum was quite accurately determined. Background contamination was less than 2% and the inelasticity of the p-C scatters was included in the calculation of the carbon analyzing power. However, the uncertainty in this inelasticity was the primary source of systematic error.

The resulting polarizations were fit, along with other data on the reaction $\gamma n \rightarrow \pi^- p$, using a resonance-background model of pion photoproduction in order to determine the couplings of many $I = 1/2$ nucleon isobars to this reaction. These couplings, several of which are better determined than in previous studies, are compared to quark model predictions. The quark model is found to give a very good description of many of these couplings.

TO JANE

TABLE OF CONTENTS

Table of Contents (Continued)

APPENDICES

LIST OF TABLES

LIST OF FIGURES

List of Figures (Continued)

1. INTRODUCTION

In the past several years there has been a marked renewal of interest in pion photoproduction in the resonance region. The origin of this interest is the fact [1, 2, 3, 4] that the electromagnetic widths of the nucleon isobars are a particularly good place to study the constituent quark model. Despite their almost naive simplicity, several such models with the quarks bound by harmonic oscillator potentials have been found to explain, at least qualitatively, many of the features of pion photoproduction in the resonance region [3]. Furthermore, the pattern of agreements and disagreements between the data on photoproduction and quark model predictions provides a useful test of the various features of these models.

Pion photoproduction and the study of πN resonances have, of course, long been connected [5, 6]. However, photoproduction data cannot hope to compete with data on πN scattering in statistics or, until the introduction of relatively monochromatic photon beams, in resolution. Therefore, photoproduction has played a relatively minor role in the "discovery" of πN resonances. Earlier phenomenological studies of $\gamma N \rightarrow \pi N$ have been mainly directed toward: (1) determining how the known resonances affect the photoproduction reaction [7, 8, 9]; and (2) pursuing topics such as dispersion relations [10, 11, 12] or pastimes such as looking for isotensor photons [13]. More recently, a dramatic increase in the amount of photoproduction data in the resonance region -- largely due to experiments performed at laboratories in Europe and Japan -- has made possible greatly improved phenomenological analyses of pion photoproduction in this kinematic region.

(A list of these new experiments may be found in reference [15]). The results of such studies [14, 15] are now mainly directed toward improving knowledge of the electromagnetic couplings of nucleon resonances and comparing these results to quark model predictions.

All of these analyses suffer from a lack of data on photoproduction from neutrons. For the reaction $\gamma n \rightarrow \pi^o n$ this lack of data is understandable. The reaction $\gamma n \rightarrow \pi^- p$, however, has two charged particles in the final state, and the only excuse for not having more and better data on this reaction is that such experiments require the use of targets at least as complicated as deuterium. The manner in which "deuterium effects" complicate the analysis of such experiments is discussed in Section 2.

For isospin 3/2 resonances, this lack of data has not been a serious issue because, assuming the photon to be a mixture of I = 0 and I = 1 components, the photoproduction amplitudes may be written as [9]

$$\begin{aligned} A^{+} &= \sqrt{\frac{1}{3}}\, A^{v3} - \sqrt{\frac{2}{3}}\, (A^{v1} - A^{s}) \\ A^{po} &= \sqrt{\frac{2}{3}}\, A^{v3} + \sqrt{\frac{1}{3}}\, (A^{v1} - A^{s}) \\ A^{-} &= \sqrt{\frac{1}{3}}\, A^{v3} - \sqrt{\frac{2}{3}}\, (A^{v1} + A^{s}) \\ A^{no} &= \sqrt{\frac{2}{3}}\, A^{v3} + \sqrt{\frac{1}{3}}\, (A^{v1} + A^{s}) \end{aligned} \qquad (1.1)$$

where A^{+}, A^{po}, A^{-}, and A^{no} are the amplitudes for $\gamma p \rightarrow \pi^+ n$, $\gamma p \rightarrow \pi^o p$, $\gamma n \rightarrow \pi^- p$, and $\gamma n \rightarrow \pi^o n$, respectively. A^{v3} is the amplitude for the I = 1 component of the photon to interact with the nucleon in a total isospin 3/2 state; A^{v1} is the amplitude for this component to interact

in a total isospin 1/2 state; and A^s is the amplitude for the photon to interact via its I = 0 component.

For I = 1/2 resonances the existence of the independent amplitudes A^{vl} and A^s means that A^- and A^{no} are not determined by A^+ and A^{po}. A separate determination of the contribution of these resonances to the reaction $\gamma n \rightarrow \pi^- p$ is therefore necessary. Aside from testing quark model predictions, such a determination also allows one to say something about the isoscalar, A^s, versus the isovector, A^{vl}, contributions to such resonances. This is an interesting issue in photoproduction physics due to apparent inconsistencies when these resonances are observed in different final states [3, 16].*

It is well known [17, 18] that a knowledge of the recoil proton polarization is very helpful in determining the contribution of various resonances to pion photoproduction. This is particularly true for the polarization at CM pion angles of 90^o if resonances of opposite parity are interfering with each other. The region from 400 to 1200 MeV in laboratory photon energy contains the odd parity resonances $S_{11}(1530)$, $S_{31}(1660)$, $S_{11}(1700)$, $D_{13}(1510)$, and $D_{15}(1650)$ as well as the even parity resonances $P_{11}(1470)$, $P_{11}(1650)$, and $F_{15}(1688)$. Also, the tails of the even parity resonances $P_{33}(1233)$ and $F_{37}(1925)$ strongly affect this region so there is ample scope for interferences leading to non-zero recoil polarizations at 90^o as well as at other CM pion angles where the interference of resonances of the same parity can also contribute. An experiment to measure the recoil proton polarization for the reaction $\gamma n \rightarrow \pi^- p$ in this region thus offers an oppor-

---

*The most well studied of these "different" final states is $\gamma N \rightarrow \eta N$.

tunity to improve the knowledge of the photoexcitation from neutrons of many of the I = 1/2 nucleon resonances. Such an experiment was performed at the Caltech synchrotron, and the analysis of this experiment is discussed in Sections 2 through 4 of this thesis.

The manner in which this experiment was performed may be briefly outlined as follows. The final state $\pi^- p$ was photoproduced from neutrons in a deuterium target, a simple spectator model being used to relate the observed reaction $\gamma d \rightarrow \pi^- pp$ to $\gamma n \rightarrow \pi^- p$. The final state was identified by a coincidence between the pion detected in a magnetic spectrometer, where its momentum and angles were quite accurately determined, and the recoil proton detected in a scintillation counter. The recoil proton was allowed to scatter from carbon in the plates of a range-scattering spark chamber and its energy was measured by bringing it to rest in this chamber. The azimuthal angular distribution of these p-C scatters, as reconstructed from pictures taken of each event, determined the polarization of the recoil proton. A maximum likelihood calculation, based on the spin 0 - 1/2 scattering formalism, was used to extract this polarization from the azimuthal distribution.

Unfortunately, there exist far too many I = 1/2 resonances in the region being studied for the results of this experiment alone to determine the coupling of any of them to this reaction. Therefore, in discussing the results of this experiment (Section 5), the following procedure is used. A phenomenological fit to a large sample of $\gamma n \rightarrow \pi^- p$ data including the results of this experiment is made in the region from 400 to 1200 MeV in laboratory photon energy using the

same model as in several previous studies [9, 15]. It is hoped that the inclusion of the present polarization results in this analysis will improve the knowledge of the coupling of at least some of the I = 1/2 resonances to this reaction. The degree to which this hope is realized will be discussed after the results of this analysis are presented.

Finally, the resonance couplings determined by this analysis will be compared to the results of certain quark model calculations to see how successful a particular version of this model [4] is in predicting these couplings. A discussion of this comparison will indicate where modifications of this model might be necessary.

2. THE EXPERIMENTAL METHOD

The quantity being measured in this experiment is the polarization of the recoil proton in the reaction

$$\gamma n \rightarrow \pi^- p \quad . \tag{2.1}$$

There are, of course, no neutron targets, and the reaction actually observed was

$$\gamma d \rightarrow \pi^- pp \quad , \tag{2.2a}$$

which was interpreted as a photon interacting with the loosely bound neutron in the deuterium nucleus (to form the π^- and a recoil proton) with the proton, p_s, in this nucleus being unaffected by the interaction. Thus, the reaction is viewed as

$$(\gamma n)p_s \rightarrow (\pi^- p)p_s \quad . \tag{2.2b}$$

The assumptions made in this simple "spectator" model of (2.2a) are: (1) the binding energy of the neutron is negligible, serving only to define the momentum distribution of the spectator proton and the initial neutron via the Hulthén wave function*; (2) the radius of the interaction is small compared to the inter-nucleon distances in deuterium; and (3) the spectator does not interact with the other particles in the initial and final states. (1) is certainly a reasonable assumption; (2) and (3) are less obvious. The possible initial and final state interactions of the spectator proton are discussed in Section 2.3. Even in this simple model, the fact that the initial neutron has a momentum

* The momentum distribution given by this wave function peaks near 45 MeV/c. It gives a reasonably good description of the observed spectator momentum distribution for the beam energies used in this experiment [19]. The coincidence between the pion and the recoil proton which we require discriminates against events with high spectator momenta (since these are the furthest "off center" from the angles given by two-body kinematics) and therefore the high momentum region in

not negligible compared to that of the other particles causes kinematical complications which are discussed in Section 2.3 and which will affect many aspects of the analysis.

2.1 Outline of Experimental Procedure

The manner in which this experiment was carried out at the Caltech synchrotron was as follows.

(1) A Bremstrahlung beam, produced by accelerating electrons and then allowing them to strike a tantalum target, was directed onto a liquid deuterium target.

(2) Pions from reaction (2.2a) were then detected in a 600 MeV/c spectrometer where their momenta were quite accurately determined. Protons traversing this spectrometer could be rejected by their large pulse heights in certain counters of the spectrometer system. There was, however, no means of distinguishing electrons or muons from pions. (The effects of this lack of identification are discussed in Appendix B).

(3) Protons from the reaction (2.2a) were detected in coincidence with the π^- by a single scintillation counter. The signals from this counter were also pulse height discriminated, this time to reject minimum ionizing particles and accept only proton signals.

(4) The proton then entered a range-scattering chamber consisting of alternating spark gaps and carbon plates. If the fast electronics indicated a coincidence between a pion signal in the spectrometer and a signal in the proton counter, the spark chambers were fired

---

which the Hulthén wave function is known to have problems [20] is not important in this experiment. An expression for the Hulthén wave function in momentum space is given in Appendix D.

and a picture was taken showing, via a system of lenses and mirrors, two 90^{o} stereoscopic views of the proton's track. Shown in each picture was a set of reference fiducials and also a coded set of lights to indicate which channel of the spectrometer recorded the pion.

(5) The information on each picture, along with the known position of the apparatus in the laboratory, was sufficient to completely reconstruct each event. However, the counting rates of various important coincidences were also monitored as a means of quickly detecting any problems with the apparatus.

The layout of the apparatus is shown in Figure 1 and the various components of the apparatus are discussed in more detail in Appendix A. All of this apparatus had been used in previous experiments, most recently those of Walden and Scheffler [21, 22] and of Bruce Winstein [23]. The unique feature of this experiment was that it was the first in which one of the large magnetic spectrometers was used in obtaining a very clean trigger for the spark chamber apparatus. It was also the first experiment on the recoil proton polarization in π^- photoproduction done at Caltech.

In all, some 361 rolls of film, with about 780 exposures per roll, were taken at seven different kinematical settings. These settings are tabulated in Table 1 along with pertinent data on each.

(6) The film was then scanned, and only those frames in which the proton underwent an "acceptable" proton-carbon (p-C) scatter and stopped in the range chamber were considered further. The scanning procedure is described in more detail in Section 3.1, where an acceptable p-C scatter is defined. Some 32,000 events passed the

scanning criteria.

(7) These events were then measured. This consisted of using a projection table with movable cross-hairs to digitize the proton's track as well as several of the reference fiducials in both views.

(8) Using this information along with the momentum channel of the pion and the surveyed position of the apparatus in the laboratory, a computer analysis program reconstructed the kinematics of each event. This reconstruction is discussed in Section 3.2. The coordinate system used in describing the observed events is depicted in Figure 2. The polarization of the recoil protons is determined from the $\phi_{p'}$ distribution in the observed p-C scatters, each weighted according to a known function of $T_{p'}$ and $\theta_{p'}$ called the "analyzing power" of carbon. The manner in which this $\phi_{p'}$ distribution is related to the recoil proton polarization is described in Section 2.2.

Finally, a word on terminology. Data were taken at seven different settings shown in Table 1. However, in calculating the polarization, all the data at a given CM pion angle were grouped together and then divided into equal bins in laboratory photon energy. Whenever the term "kinematical setting" is used in this thesis, it will refer to one of the settings in Table 1; and whenever the term "kinematical bin" is used, it will refer to one of the bins for which the results are reported (see Table 3).

2.2 The p-C Scattering Formalism and the Polarization Calculation

The proton-carbon scatterings observed in the range chamber can be dealt with using the well known [24] formalism for spin 0 - spin 1/2 scattering processes.

The most general parity conserving amplitude for such a scattering is given by

$$M = f + g(\vec{\sigma}\cdot\hat{n}) \ . \tag{2.3}$$

In this formula, f and g are functions of the scattering angle θ and energy E ; $\hat{n}$ is the normal to the scattering plane, $\hat{n} = \frac{\vec{p}\times\vec{p}'}{|\vec{p}\times\vec{p}'|}$, where $\vec{p}$ and $\vec{p}'$ are the initial and final momenta, respectively; and $\vec{\sigma} = (\sigma_x, \sigma_y, \sigma_z)$ are the Pauli spin matrices.

If the initial beam of spin 1/2 particles has a polarization $\vec{P}_I$, then the initial density matrix, ρ_i, is given by

$$\rho_i = \tfrac{1}{2}(1 + \vec{P}_I\cdot\vec{\sigma}) \ , \tag{2.4a}$$

while the final density matrix is given by

$$\rho_f = M\rho_i M^+ \ . \tag{2.4b}$$

The normalization in (2.4a) is chosen such that the cross section for this scattering is given by

$$\sigma(\theta, \phi) = Tr\rho_f = TrM\rho_i M^+ \ . \tag{2.5}$$

Inserting (2.3) into (2.5) gives the basic formula of our analysis:

$$\sigma(\theta, \phi) = \sigma_o(\theta)(1 + \vec{P}_I\cdot\hat{n}A(E, \theta)) \tag{2.6}$$

where

$$A(E, \theta) \equiv 2\,Re\,(f^* g)/\sigma_o(\theta)$$

is called the analyzing power of the spin 0 target and

$$\sigma_o(\theta) \equiv |f|^2 + |g|^2$$

is the cross section for an unpolarized incident beam.

Let us now apply this formalism to the p-C scatters observed in our range chamber. Since parity is conserved in the strong and in the electromagnetic interactions, the polarization of the initial

proton beam, i.e., the recoil protons from the photoproduction reaction, would be entirely along the direction $\hat{k} \times \hat{p}_R$ (see Figure 2) if the initial neutron were at rest. However, the Fermi motion of our initial neutron, as well as possible final state interactions between the recoil and spectator protons, can produce a small but non-zero polarization in the $\hat{k} \times \hat{p}_R$ plane (see Sections 2.3 and 3.3). Our apparatus would be sensitive only to the component of this polarization "in the plane" perpendicular to the proton momentum $\hat{p}_R$. Therefore, assume that the polarization of the recoil proton beam has the form

$$\vec{P}_I = \vec{P}_\perp(\vec{k}\times\vec{p}_R)/|\vec{k}\times\vec{p}_R| + P_\parallel(\vec{p}_R\times(\vec{k}\times\vec{p}_R))/|\vec{p}_R\times(\vec{k}\times\vec{p}_R)|$$

Then using (2.6) and the coordinate system of Figure 2, we have

$$\sigma(\theta_{p'}, \phi_{p'}) = \sigma_o(\theta_{p'})\left(1+P_\perp A_c(T_{p'}, \theta_{p'})\cos\phi_{p'}+P_\parallel A_c(T_{p'}, \theta_{p'})\sin\phi_{p'}\right) \tag{2.7}$$

which is the desired relation between the recoil polarization and the $\phi_{p'}$ distribution of the observed p-C scatters. A_c is the analyzing power of the carbon in the chamber. The properties of this analyzing power and the accuracy to which it is known for a given event are discussed in Appendix E.

In applying (2.7) to determine $P_\perp$ and $P_\parallel$ we use the maximum likelihood method; namely, if these polarizations have values of $P'_\perp$ and $P'_\parallel$ respectively, the "likelihood" of observing a given p-C scatter is proportional to the quantity

$$1+P'_\perp A_c(T_{p'}, \theta_{p'})\cos\phi_{p'} + P'_\parallel A_c(T_{p'}, \theta_{p'})\sin\phi_{p'}$$

where the variables $T_{p'}$, $\theta_{p'}$, and $\phi_{p'}$ are measured from the events reconstructed track. The "likelihood" of the N p-C scatters observed

in any kinematical bin is then given by

$$L(P_\perp', P_\parallel') = \prod_{i=1}^{N} \left(1+P_\perp' A_c(T_{p'}, \theta_{p'})\cos\phi_{p'}+P_\parallel' A_c(T_{p'}, \theta_{p'})\sin\phi_{p'}\right)_i. \quad (2.8)$$

The values of $P_\perp'$ and $P_\parallel'$ which maximize this likelihood are the best estimates obtainable from the data for the quantities $P_\perp$ and $P_\parallel$ respectively.*

2.3 Deuterium Effects

Even with a target nucleon at rest (H_2 target), photoproduction experiments with a Bremstrahlung beam suffer from a rather broad resolution in photon energy (typically of the order of 20 MeV if only the pion is detected) due to finite apertures and target size coupled with the fact that essentially all values of k are present in the beam. A deuterium target with its spread in the initial neutron momentum makes this resolution even worse (by at least a factor of 2) if only the pion is detected. Detection of the recoil proton in coincidence with the pion significantly improves this situation [22], because a proton detector, centered on the recoil angles for an initial neutron at rest, discriminates against events with large neutron Fermi momenta. This improves the resolution in photon energy and also in CM pion angle. In the experiment of Walden and Scheffler [21, 22], the size of the recoil proton detector was chosen by a compromise between the improvement in these resolutions and the resulting decrease in counting rates. In our experiment, the proton

*Assuming the distribution given in (2.7), an estimate of $P_\perp$ can also be made from the average of $\cos\phi_{p'}$ over the observed events ($P_\perp \approx 2\overline{\cos\phi_{p'}}/\overline{A}$ where $\overline{A}$ is the average analyzing power for the events in a given bin), but this estimate is not as good [23] as the one given by the maximum likelihood method.

counter size was chosen such that as few events as possible left the sides of the scattering chamber; however, the solid angle covered was approximately the same as theirs so that nearly the same improvement in resolution was obtained.

The fact that in our experiment the total range of the recoil proton in carbon was measured might be thought to offer an even larger improvement in resolution due to knowledge of the proton energy. However, this is not really the case, since each event contained a proton-carbon scatter with an undetermined inelasticity and therefore the resolution in proton energy was not better than about 25 MeV. In fact, the main deuterium problem in this experiment was that the broad resolution due to the Fermi motion of the neutron made the inelasticity of the p-C scatters unmeasurable, and this in turn caused a large uncertainty in the value of the carbon analyzing power used for each event (see Section 4.2).

The other types of deuterium effects are those caused by the spectator proton. In the initial state, the main concern is the shadowing of the target neutron by the spectator proton. This shadowing, or Glauber effect, is not expected to be an important effect in the energy region of this experiment [21, 25]. Furthermore, any shadowing is presumably uncorrelated to the recoil proton polarization.

In the final state, the most obvious "interaction" of the spectator and recoil protons is the reduction in the number of possible final states due to the Pauli exclusion principle. This reduction is proportional to the deuterium form factor F(D)* [21]. In our kine-

* $F(D) = \int \exp[-(\vec{k}-\vec{q})\cdot\vec{r}\,]\mu^2(\vec{r})d^3\vec{r}$, where $D = |\vec{k}-\vec{q}\,|$ is the Hulthén

matic region $F(D) \approx 0$, and so the exclusion principle fortunately has a negligible effect on our results.

The possible strong interaction between the recoil and spectator protons is far harder to assess. We can say: (1) the charge independence of the strong interaction coupled with the fact that in our kinematic region $\sigma_{\pi^+}(\text{off } H_2)/\sigma_{\pi^+}(\text{off } D_2) \approx 1$ (after the Pauli principle is corrected for) would indicate that the effect is small; (2) the spectator momentum distribution observed in the data did not differ significantly from the prediction of the Hulthén wave function modified by our acceptances (see Section 3.3) which would also indicate a small effect; (3) detecting the recoil proton in coincidence with the pion discriminates against large spectator momenta which might be expected to have the largest final state interactions; and (4) the few theoretical calculations which exist [26, 27, 28] also indicate a small final state interaction at our energies. However, all these arguments are rather imprecise, and the best that can be said is that this effect is certainly well below the statistical errors of about 10 per cent. This also means that any polarization in the $\hat{k} \times \hat{p}_R$ plane due to this effect should be negligible within the statistical errors.

2.4 Backgrounds

The most serious potential background in this experiment would be a reaction that would produce a π^- and a proton in the final state, thus giving a "real" trigger, albeit from a false source. The

---

wave function [21]. In our experiment D is large, and therefore F(D) is quite small. (In the forward direction, on the other hand, $F(D) \approx 1$ and this leads to a 1/3 reduction in the cross section off deuterium from what it would be off free neutrons).

only important candidate is 2π photoproduction from deuterium. The contamination due to this background, as discussed in Appendix B, is fortunately very small. It is estimated to be less than 1 per cent when a coincidence is required between the pion and the recoil proton.

Another potentially annoying source of contamination is the fact that the spectrometer was unable to distinguish among pions, muons, and electrons. The effects of this lack of particle identification are discussed in Appendix B. It is found that electron contamination is very small ($\lesssim$1 per cent). The only important source of muons is the reaction under study, and their detection is found only to broaden the resolution in pion momentum somewhat.

Empty target background runs were not made in this experiment since the running time necessary to get meaningful statistics would have been enormous. The small counting rates for empty target runs indicate that such backgrounds are quite negligible.

TABLE 1

Kinematical Settings*

Setting	θ_π^{CM} (Deg)	k (MeV)	θ_π (Deg)	θ_p (Deg)	q (MeV/c)	T_p Bite (MeV)	Amount of carbon in front of chamber (cm)	Number of exposures	Number of events measured	Number of events in final sample
1	90°	650	64.64	41.43	447.60	90-270	.5	36,700	3510	2146
2	90°	750	62.60	41.12	508.0	90-290	.5	39,000	4017	2594
3	90°	800	61.63	41.02	538.16	110-300	2.5	43,700	4485	2819
4	90°	900	59.85	39.72	583.18	130-315	4.5/5.5†	46,000	5714	3176
5	120°	550	97.31	27.53	309.71	90-285	.5	39,000	3588	2361
6	120°	650	94.88	27.30	352.17	110-320	3.5	39,000	4405	2819
7	120°	750	92.61	26.99	391.99	210-360	14.5	39,000	5744	3658

*Values are nominal ones for two-body kinematics. All values refer to the lab frame (see Figure 2) unless otherwise specified.

† Approximately 1/2 of the exposures were taken with 4.5 cm of carbon in front of the range chamber and 1/2 with 5.5 cm.

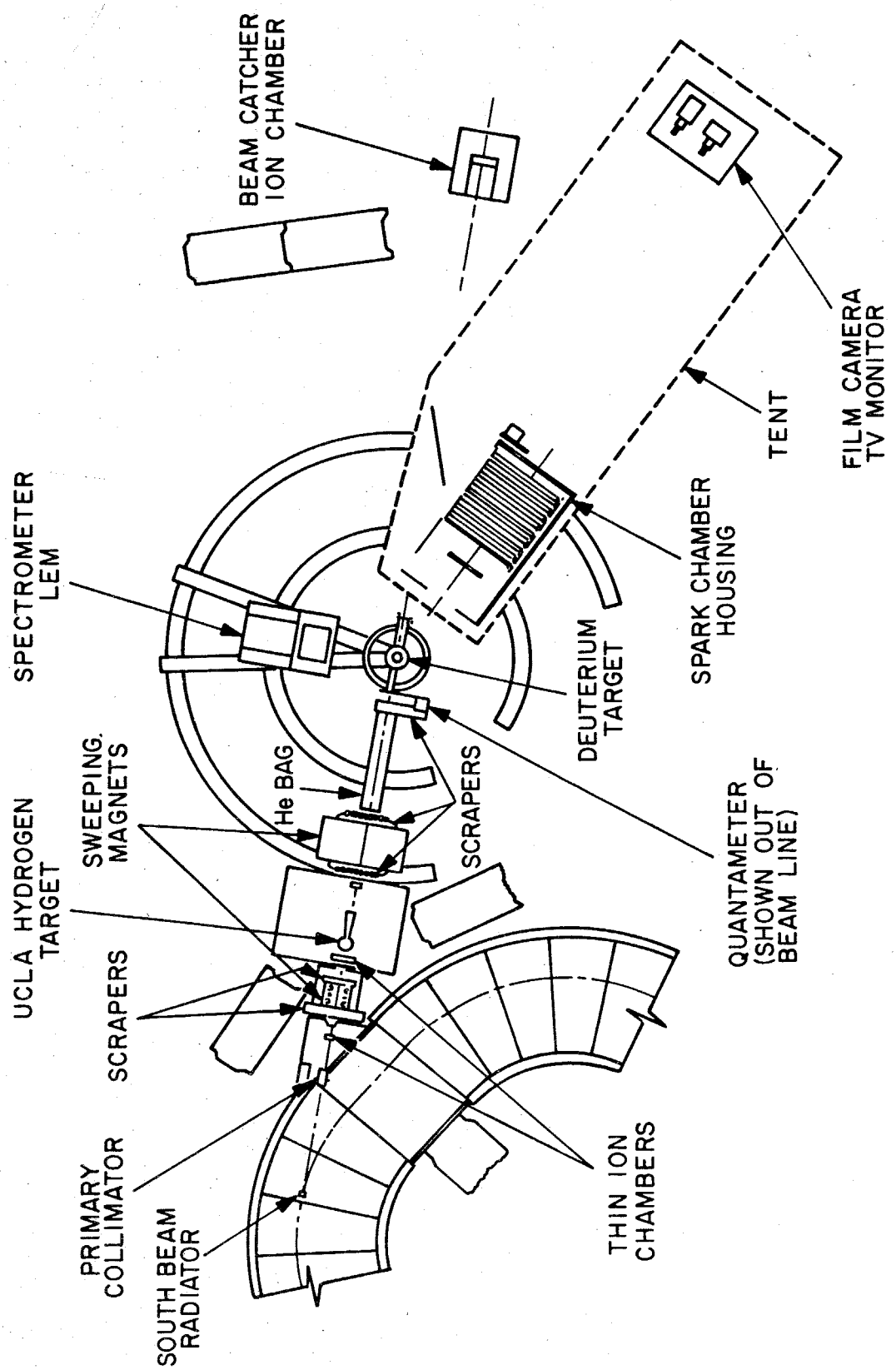

FIGURE 1 Beam and Experimental Area

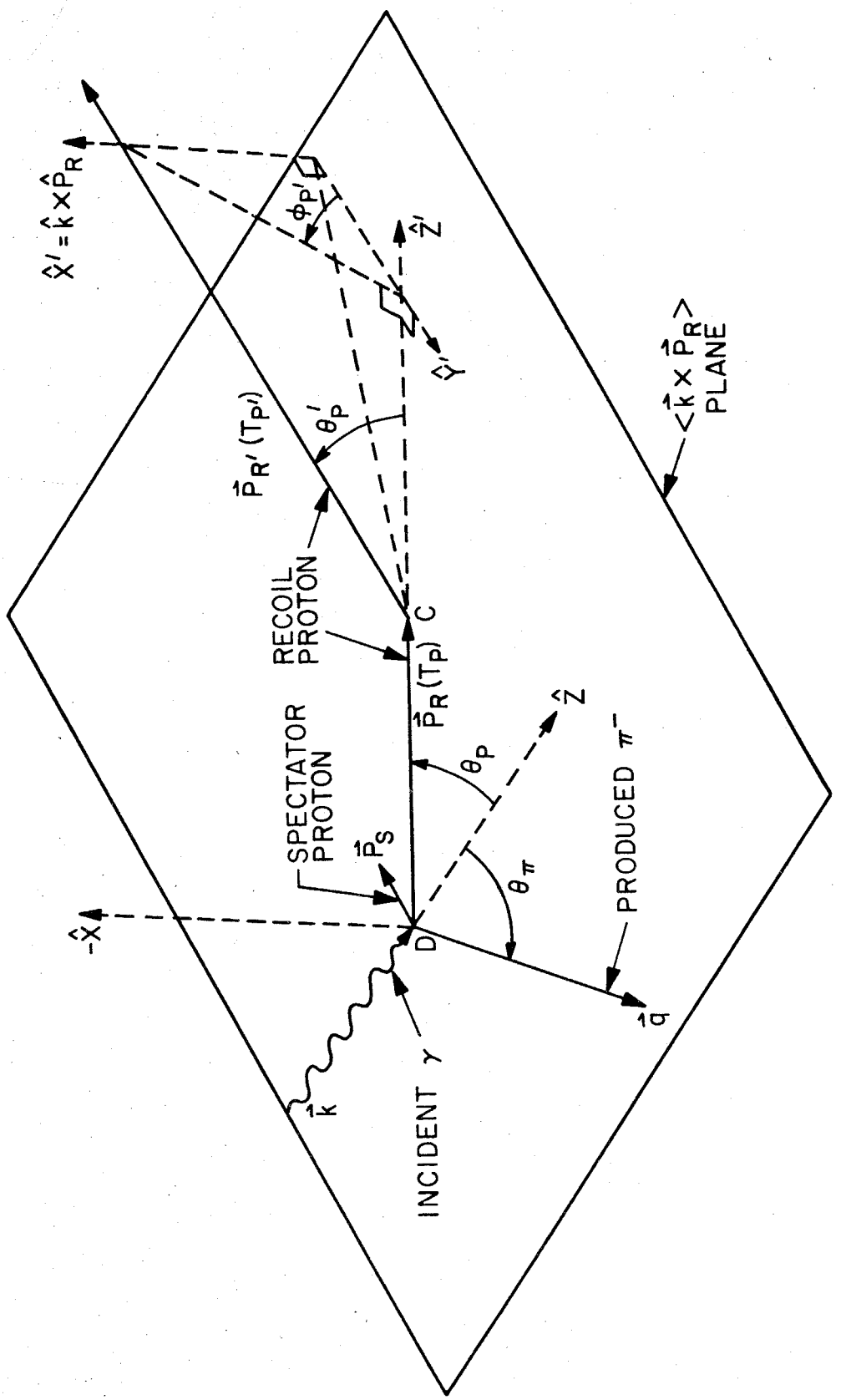

FIGURE 2 γd and p-C Interaction Kinematics

3. DATA REDUCTION

The procedure by which the exposures in this experiment were scanned to select those suitable for analysis as well as the method in which the information on these pictures was used to obtain polarization values will now be described. All of the kinematical variables referred to below are defined in Figure 2.

3.1 The Scanning and Measuring Process

The first step was to scan the 361 rolls of film taken during the running and select those events that were suitable for analysis. The criteria that defined a suitable event were as follows.

(1) The frame had to have not more than one track in each view, excluding obvious electron tracks. The information available for each event did not allow the determination of the proper track if there were two possible ones. Such events were fortunately rare, and resulted in the elimination of $\lesssim 3$ per cent of the original sample for each setting.

(2) The track had to (appear to) stop inside the range chamber in both views. Since the Fermi motion of the neutron made the initial energy of the recoil proton unknown, its energy after the p-C scatter had to be measurable in order to compute the analyzing power for that event. Therefore, the total range of the particle after the p-C scatter had to be known. This resulted in the rejection of 5 - 10 per cent of the original sample depending on the beam energy.

(3) The event had to have one proton-carbon scatter of at least 3 degrees in one of the views and of not more than 30 degrees in either view. The limit of 3 degrees is used because the analyzing

power of carbon is small and poorly known for angles less than this. Also, detection efficiency and the resolution in $\phi_{p'}$ become problems for such small scatters. Because of this cut, which eliminated 35 - 40 per cent of the original sample, only events with $\theta_{p'} \geq \sqrt{2} \times 3^{o}$ are used in the actual analysis. The 30 degree cut, which eliminated 12 - 15 per cent of the events, is again because the analyzing power is poorly known for angles larger than this. These scattering criteria were the main cause of events being rejected during scanning. Many frames simply did not have a significant p-C scatter.

(4) The event could not have a significant double scatter. The indeterminancy in the inelasticity of the p-C scatters caused the kinematics to be too poorly determined in such events, which were, in any case, rare. This cut caused the elimination of less than 5 per cent of the original sample.

(5) Finally, each track had to have at least three sparks after the scatter. There are two reasons for this criterion: (a) it took at least three sparks to get a good fit on the final trajectory of the proton; and (b) the carbon analyzing power is poorly known for energies less than 90 MeV so that only events which penetrated through at least two carbon modules after the scatter are useful. This criterion eliminated 12 - 18 per cent of the events which passed criteria (1) - (4).

Besides the rejections due to these criteria, there were the frames (15 - 20 per cent, depending on the setting) which had no discernible track or in which the track failed to penetrate more than two modules into the chamber.

The scanning was performed by two independent groups of

scanners and any conflicts were resolved by the most experienced of our scanners (who did not participate in either of the initial scans). It is very important that no artificial bias be introduced into the data during the scanning process. Appendix C discusses this point and shows why it is believed that no serious bias of this nature exists in the present experiment.

The events which passed the scanning step were next measured. This process consisted of digitizing the proton track in each view along with three of the reference fiducials and punching these spark coordinates onto computer cards. These cards also contained the event number as well as the momentum hodoscope channel of the pion. The information on these cards was immediately put on a magnetic tape to serve as input for the program which reconstructed the events.

3.2 Event Reconstruction

This tape, containing all the information known about each event, was now processed in order to calculate the values of those variables necessary in obtaining the polarizations as well as others used in making various checks on the data sample. Table 2 gives a list of those quantities of particular interest in the analysis along with the estimated resolution in each.

The procedure used in obtaining these quantities from the information on the tape is outlined below.

(1) The coordinates of the reference fiducials for each event were fit to a master grid.* This fit preserved straight lines, but al-

*This master grid was recalibrated after every 10 to 15 rolls by repeated fiducial measurements on a particularly good exposure. This recalibration allowed for drifts in the digitizing equipment during the measuring process, as well as changes in film holder positions.

lowed correction for any movement of the film holder or misalignment of the lens - mirror system. Events with too large a χ^2 for this "grid fit" were considered poorly measured and were not used in the polarization calculation.

(2) Using the coordinates of the sparks in the proton track (translated into the "master grid frame"), the trajectories of the proton before and after the proton-carbon scatter were determined. For those settings with a large amount of carbon in front of the chamber the resolution in the initial trajectory was noticeably degraded by multiple scattering. Also, it was hard to get a good fit to the trajectory if there were only 2 or 3 sparks before the scatter. These effects are illustrated in Figure 3, which shows the distributions in the $\hat{x}$ and $\hat{x} \times \hat{p}_{Ro}$ intercepts of the initial trajectory in the median plane of the target where $\hat{p}_{Ro}$ is the value of $\hat{p}_R$ along the center line of the range chamber (see Figure 2). The large tails on the curves in Figure 3 do not come from events that originate outside the target but are due to the error in the initial trajectory. Any event in which the reconstructed track missed the target by more than one standard deviation in the resolution of the initial trajectory was considered to be poorly measured and was not used in the polarization calculation.

Figure 3 contains only events with at least two sparks before the scatter. The initial trajectory of events which scattered sooner than this can be reconstructed only by assuming that the event originated in the center of the target and (for events which scatter before entering the chamber) by assuming that it scattered in the median plane of the carbon in front of the chamber. As indicated in Table 2, such events,

especially if there is much carbon involved, have rather poor resolutions. Except for these special cases, the trajectories are calculated by a straight-line fit to the sparks in the track. Events in which the χ^2 of this fit was too large were not used in the polarization calculation.

(3) The initial lab angles, θ_p and ϕ_p, of the proton are immediately calculable from the fitted trajectories using the surveyed position of the spark chamber apparatus.

(4) Also, from the initial and final trajectories, the vertex of p-C scatter as well as the angles, $\theta_{p'}$ and $\phi_{p'}$, of this scatter can be calculated. The resolution in the position of the vertex was on the order of 0.5 cm, and all events in which the closest approach of the reconstructed initial and final trajectories lay outside a distribution with this width were not used in the polarization calculation.

(5) The final trajectory was checked to be certain that the particle did truly stop within the desired fiducial volume and thus had a known range. Events which left this volume or which would have left it if $\phi_{p'} \rightarrow \phi_{p'}+180^\circ$ were not used in calculating the polarization. The reason for the exclusion of events whose reflection in $\phi_{p'}$ left the chamber is discussed in Section 3.4 and in Appendix C.

(6) From the length of the initial and final trajectories and the type of material traversed, the energy of the recoil proton after the p-C scatter, $T_{p'}$, as well as its initial energy, T_p, can be calculated. In these calculations the formula used is

$$(\log_{10}T) = \sum_{i=0}^{4} a_i(\log_{10}R)^i , \qquad (3.1)$$

where R is the range in gm/cm^2. The constants a_i are determined empirically from range-energy curves.

The resolution in $T_{p'}$ is reasonably good except in cases where the proton scattered before the chamber, making the vertex rather poorly defined (especially if there was much carbon in front of the chamber). The resolution in T_p is severely limited by the lack of knowledge of the inelasticity of the p-C scatter, equation (3.1) giving this energy properly only if the scatter was elastic.

(7) The lab angles of the pion, θ_π and ϕ_π, for a given spectrometer placement, are well determined by the spectrometer aperture. The momentum of the pion, q, is also well determined from the hodoscope channel and the magnet setting of the spectrometer. An exception to this is any case (due, presumably, to knock-on electrons) where two or more momentum channels counted in a given event. In these, fortunately rare, cases the central momentum setting had to be assumed, and the resolution became the full width of the spectrometer. Finally, for some fraction (about 10 per cent) of the events, the pion decayed before completely traversing the spectrometer. These indistinguishable events also have a somewhat broader resolution in q (see Appendix B).

(8) Once the above quantities are known, the remaining quantities of interest can be calculated from the kinematics. These quantities include the lab photon energy, the pion angle and the total energy in the CM frame of the π^- and the recoil proton, and the momentum and angles of the spectator.

All of the above information about each reconstructed event was

placed on magnetic tape to serve as input for the program which did the actual polarization calculations.

3.3 Monte Carlo Calculations

In the process $\gamma d \rightarrow \pi^- pp$, there are 5 four-momenta involved and therefore twenty quantities are needed to determine the kinematics. The masses of the particles and energy-momentum conservation give 9 of these. The fact that the initial deuteron is at rest plus the known lab angles of the photon give 5 of the remaining 11 quantities needed. The other 6 are obtained from the measured momentum (or energy) and angles of the recoil proton and the pion. But this exhausts the list of measurable quantities, and at least one of these, T_p, is rather poorly known since each event contains a p-C scatter of unknown inelasticity. Thus, from the observed kinematical distributions alone, it is hard to make any sort of consistency check on the data. Such a check is highly desirable to be sure that the reconstruction procedures are giving sensible answers as well as to check the assumption that the various backgrounds are small.

In order to have a check on the analysis, Monte Carlo calculations were made of the expected distributions in various kinematical quantities. These calculations were based on the spectator model of the process $\gamma d \rightarrow \pi^- pp$ and used the $\gamma n \rightarrow \pi^- p$ cross sections of Scheffler and Walden [21,22]. The manner in which these calculations were performed is discussed in detail in Appendix D.

Some of the results of such calculations for each of the kinematical settings are shown in Figures 4 - 11. For each setting, the proton energy and spectator momentum distributions are shown along

with two other distributions selected from among the pion momentum and the proton and spectator angles to give an idea of the type of agreement obtained. Figure 11 shows the agreement for the proton energy after the p-C scatter for: (a) all of the $\theta_{\pi}^{CM} = 90^{o}$ data, and (b) all of the $\theta_{\pi}^{CM} = 120^{o}$ data grouped together. In general, the Monte Carlo distributions agree with the observed data distributions. However, some of these distributions deserve special comment.

In the Monte Carlo calculations, the position in the spectrometer is randomly chosen, whereas in the real data the pion is, of course, assumed to have gone through the center of the hodoscope channel. This accounts for the apparent difference in resolution in these curves.

The curves for total proton energy agree quite well. The "structure" in the proton energy curves, especially those in Figure 11, is strictly due to the binning coupled to the fact the energies are "quantized" by the fact that we assume the proton scatters and stops at the center of the modules in question. This effect has nothing to do with any real "structure" in these quantities. The agreement obtained for the proton energy is the best indication we have that the event reconstruction process is giving sensible results.

The Monte Carlo calculation made no correction for any final state interactions with the spectator proton. Therefore, the agreement with the observed spectator momentum distributions (excluding differences due to the T_p inelasticity) would seem to indicate that such final state interactions have at most a small effect on the results of this

experiment.

Finally, it might be mentioned that the reasonable agreement between the Monte Carlo simulations and the observed data distributions in the type of curves shown is sufficient to guarantee a similar agreement for any other kinematical distribution such as the lab photon energy or CM pion angle. This is a result of the fact that (given the narrow resolutions in the lab pion and photon angles as well as the fact that the deuteron is at rest) the quantities shown are sufficient to determine the kinematics.

3.4 The Polarization Calculations

The output of the event reconstruction program was then submitted to another program which actually calculated the polarization values. First of all, those events which did not reconstruct well were deleted. Most of these rejections have already been mentioned in Section 3.2. They include events with too large a χ^2 for the "grid fit," events with too large a χ^2 for the proton trajectory fits, events which missed the target by more than one standard deviation in the resolution of the initial trajectory, events which left the fiducual volume, and events in which the vertex was too poorly defined.

Next, events which reconstructed properly but which were not useful in the polarization calculation were rejected. These included all events outside of the scanning cuts of 4.2° and 30° in $\theta_{p'}$ (see Section 3.1), events outside of the range 90 MeV $\leq T_{p'} \leq$ 300 MeV (since the analyzing power is poorly known outside this range), and all events with an analyzing power of less than 0.1 since the uncertainty in the analyzing power is always about this large. They also included events

which would have left the chamber if $\phi_{p'} \rightarrow \phi_{p'}+180^{o}$ in order to avoid an artificially induced bias in the $\phi_{p'}$ distribution due to the rejection of events which left the chamber. This point is discussed in more detail in Appendix C.

The events which survived these cuts were then divided into bins of 50 MeV in lab photon energy at CM pion angles of 90^{o} and 120^{o}. For each bin, the likelihood function, as defined in Section 2.2, is

$$L(P_{\perp}, P_{\parallel}) = \prod_{i=1}^{N} (1+P_{\perp}A_c(T_{p'}, \theta_{p'})\cos\phi_{p'} + P_{\parallel}A_c(T_{p'}, \theta_{p'})\sin\phi_{p'})_i \qquad (3.2)$$

where N is the number of events in the bin. The analysis program used Newton's method to calculate the values of $P_{\perp}$ and $P_{\parallel}$ which maximize this function, these being the best estimates of the polarizations obtainable from the observed $\phi_{p'}$ distribution. The results of these calculations are summarized in Table 3. In Figures 12 and 13, the likelihood functions $L(P_{\perp})$ and $L(P_{\parallel})$ are shown for several of the bins. In Figure 14 a three-dimensional plot of the function $L(P_{\perp}, P_{\parallel})$ is shown for one of the bins.* These curves are all normalized to be equal to unity at their maximums.

The statistical error in the polarization values calculated in this manner is given by

$$\Delta P = \frac{1}{\bar{A}} \sqrt{\frac{2}{N}} , \qquad (3.3)$$

where N is the number of events in the bin and $\bar{A}$ is the average

* The sign of $P_{\perp}$ in Figures 12-14 as well as in Table 3 has been reversed. The reasons for this are discussed in Section 4.

carbon analyzing power for these events; that is,

$$\overline{A} \equiv \frac{1}{N} \sum_{i=1}^{N} A_c(T_{p'}, \theta_{p'})_i \ .$$

If we were observing a true two-body interaction, parity conservation would require that only $P_\perp$ (the component of polarization along $\hat{k} \times \hat{p}_R$) be non-zero. However, in the present experiment a non-zero value for the polarization in the $\hat{k} \times \hat{p}_R$ plane can result from a final state interaction with the spectator proton or from the initial Fermi momentum of the neutron. The first effect was discussed in Section 2.3 and is felt to be well below the statistical errors. A non-zero value of $\vec{p}_n$ means that we now have available independent axial vectors such as $\hat{k} \times \hat{p}_n$, in addition to $\hat{k} \times \hat{p}_R$. These products can also be combined with $\vec{\sigma}$ to give a scalar amplitude and can lead to non-zero values for $P_{||}$. The size of this effect will now be discussed.

To estimate $P_{||}$ one must begin in the rest frame of the proton for the 2-body reaction $\gamma n \rightarrow \pi^- p$. In this frame the proton's polarization may be described by a four-vector whose time component is zero. By parity conservation the recoil polarization in this two-body reaction is perpendicular to the plane of the reaction, so that in the CM frame the polarization vector still has no time component and its space component is perpendicular to $\hat{k}^{CM} \times \hat{p}_R^{CM}$.

Now we transform the polarization vector into the lab frame using $\vec{\beta} = (\vec{p}_n + \vec{k})/(E_n + k)$ (where $\vec{p}_n \neq 0$ since we do not actually have a two-body reaction). If this is done and the resulting polarization transformed to the protons rest frame, this polarization will be found

to now have components in the plane $\hat{k} \times \hat{p}_R$ as well as perpendicular to it. (This is just the familiar precession of a four-vector under non-commuting orentz transformations.)

For $\vec{p}_n = 0$, $P_\perp = P_\perp^{CM}$ and $P_\parallel = 0$. But in our case the above effect can cause a $P_\parallel \neq 0$ and also $P_\perp \neq P_\perp^{CM}$. However, a calculation of the magnitude of $P_\parallel$ and $(P_\perp - P_\perp^{CM})$ in our kinematic region* [29] indicates that this effect is less than 1 percent, far below the statistical errors (as are the effects due to final state interactions with the spectator). This means $P_\parallel$ should be consistent with zero within the limits set by its errors.

* $k \sim 750$ MeV, $T_p \sim 300$ MeV, $|\vec{p}_n| \sim$ MeV/c .

TABLE 2. Experimental Resolutions

Kinematical Quantity [a]	How Determined	Main Sources of Uncertainty	Resolution
initial beam angle; θ_γ [b]	surveyed beam line and beam pictures	survey error; beam drift	$<0.2^\circ$
initial deuteron momentum; $\vec{p}_D$	at rest	thermal motion	negligible
pion angle; θ_π	spectrometer setting	spectrometer aperture; origin of event in target	$< 1.5^\circ$
pion angle; ϕ_π	spectrometer setting	spectrometer aperture; origin of event in target	3.9°
pion momentum; q	spectrometer setting and hodoscope channel	spectrometer acceptance	2.5 % [c]
recoil proton angle; θ_p	initial trajectory in range chamber	measurement error; vertex error; multiple scattering	$.6^\circ$ [d]
recoil proton angle; ϕ_p	initial trajectory in range chamber	measurement error; vertex error; multiple scattering	$.6^\circ$ [d]
recoil proton kinetic energy; T_p	range in carbon	inelasticity of p-C scatter	20-25 MeV [e]
photon energy; k	kinematics	error in quantities of which it is a function	25-40 MeV [f]
CM pion angle; θ_π^{CM}	kinematics	error in quantities of which it is a function	$\lesssim 2^\circ$ [f]
spectator momentum; p_s	kinematics	error in quantities of which it is a function	~10 % [f]
recoil proton kinetic energy (after p-C scatter); $T_{p'}$	range in carbon	uncertainty in range due to resolution in vertex and stopping point	10 MeV [g]

TABLE 2. Experimental Resolutions (continued)

Kinematical Quantity[a]	How Determined	Main Sources of Uncertainty	Resolution
angle of p-C scatter; $\theta_{p'}$	initial and final trajectories in range chamber	measurement error; vertex uncertainty; multiple scattering	1.3°[h]
angle of p-C scatter; $\phi_{p'}$	initial and final trajectories in range chamber	measurement error; vertex uncertainty; multiple scattering	$\Delta\cos\phi_{p'} \sim .07$[j]

[a]Unless otherwise specified, all quantities refer to the laboratory frame (defined in Figure 2). The settings referred to are those defined in Table 1.

[b] $\theta_\gamma = 0$, so ϕ_γ is undefined.

[c]This increases to 10% for the (indistinguishable) π-μ decay events (Appendix B) and for events with knock-on electrons, i.e., two channels counting. The former make up ~10% of the sample and the latter < 1%.

[d]For setting 7 multiple scattering increases this to 0.75°. Events that scatter in or before the first carbon module must be assumed to have originated in the center of the target, involving an uncertainty of $\lesssim 1.5°$. If they scatter before the first spark gap, the vertex error leads to an uncertainty of from 0.2° to 2.0°, depending on the setting.

[e]The error due to the uncertainty in range is at most 8% (for $T_p \lesssim 100$ MeV) and decreases as T_p increases, averaging ~ 4%.

[f]Dominated by the uncertainty in T_p, these values refer to individual events. The spread for a given setting is much greater, due to the large T_p bite (Table 1).

[g]This error varies from 18% to 3% as $T_{p'}$ increases such that $\Delta T_{p'}$ is approximately constant and 10 MeV is a good average. For events scattering before the first spark gap the vertex error can make $\Delta T_{p'}$ much larger. The upper limit on such events ranges from 12 to 35 MeV depending on the setting. The typical error is some 5 to 10 MeV smaller.

[h]For events scattering before the second spark gap, the origin (and in some cases the vertex) error again degrades this resolution. The upper limit becomes 2.5° for settings 1 to 6 and 4.1° for setting 7.

[j]This is a typical value ($\theta_{p'} \sim 10°$, $10° \leq \phi_{p'} \leq 80°$). The upper limit ($\theta_{p'} = 4.2°$, $\phi_{p'} = 0°$ or 180°) is generally $\Delta\cos\phi_{p'} \approx 0.11$, but for events with poor resolution on the initial trajectory due to origin and vertex errors this upper limit can become as large as $\Delta\cos\phi_{p'} \sim 0.25$.

PROTON TRAJECTORY TARGET INTERCEPTS
ALL SETTINGS

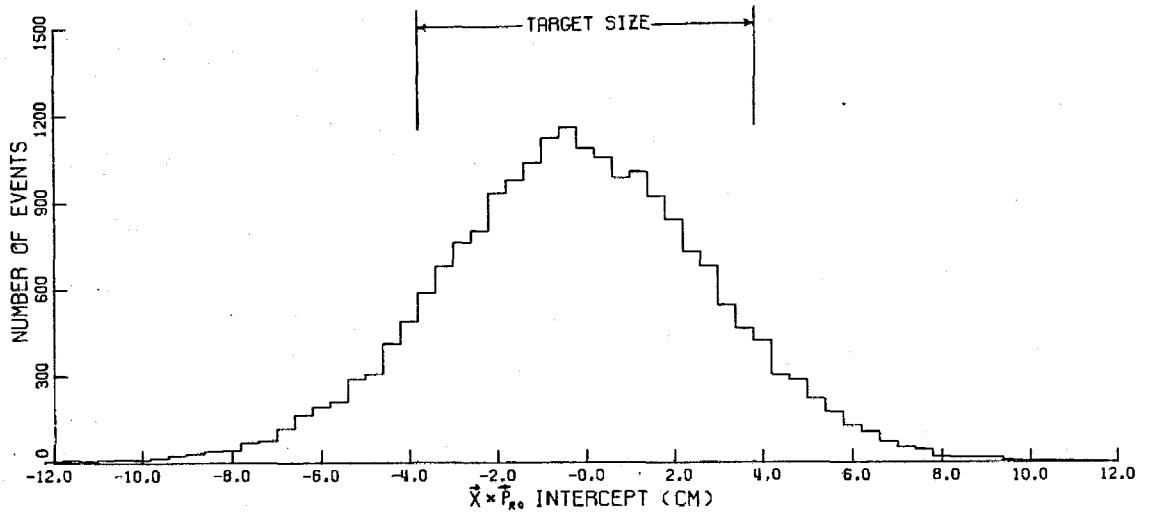

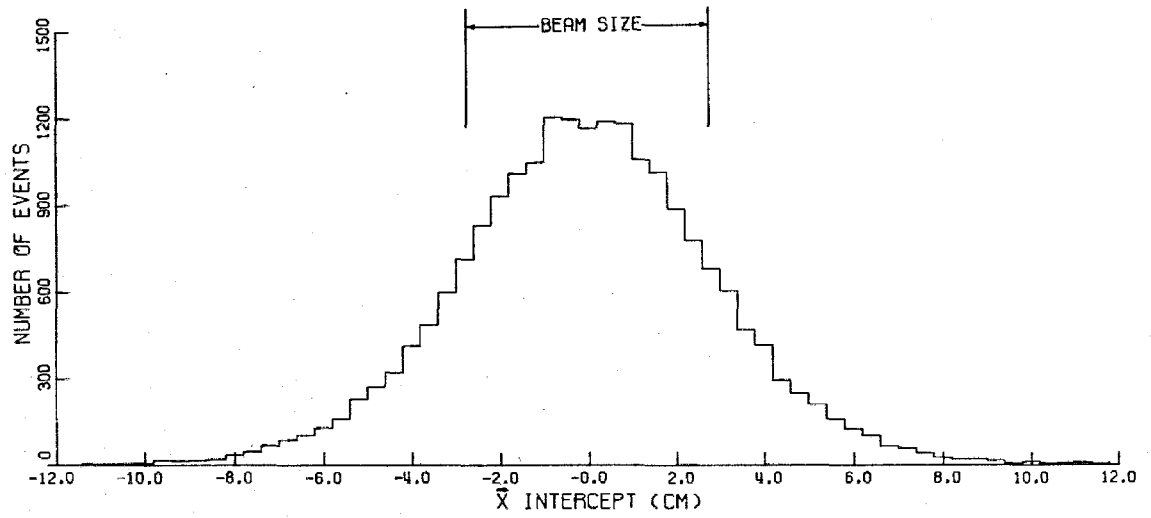

FIGURE 3

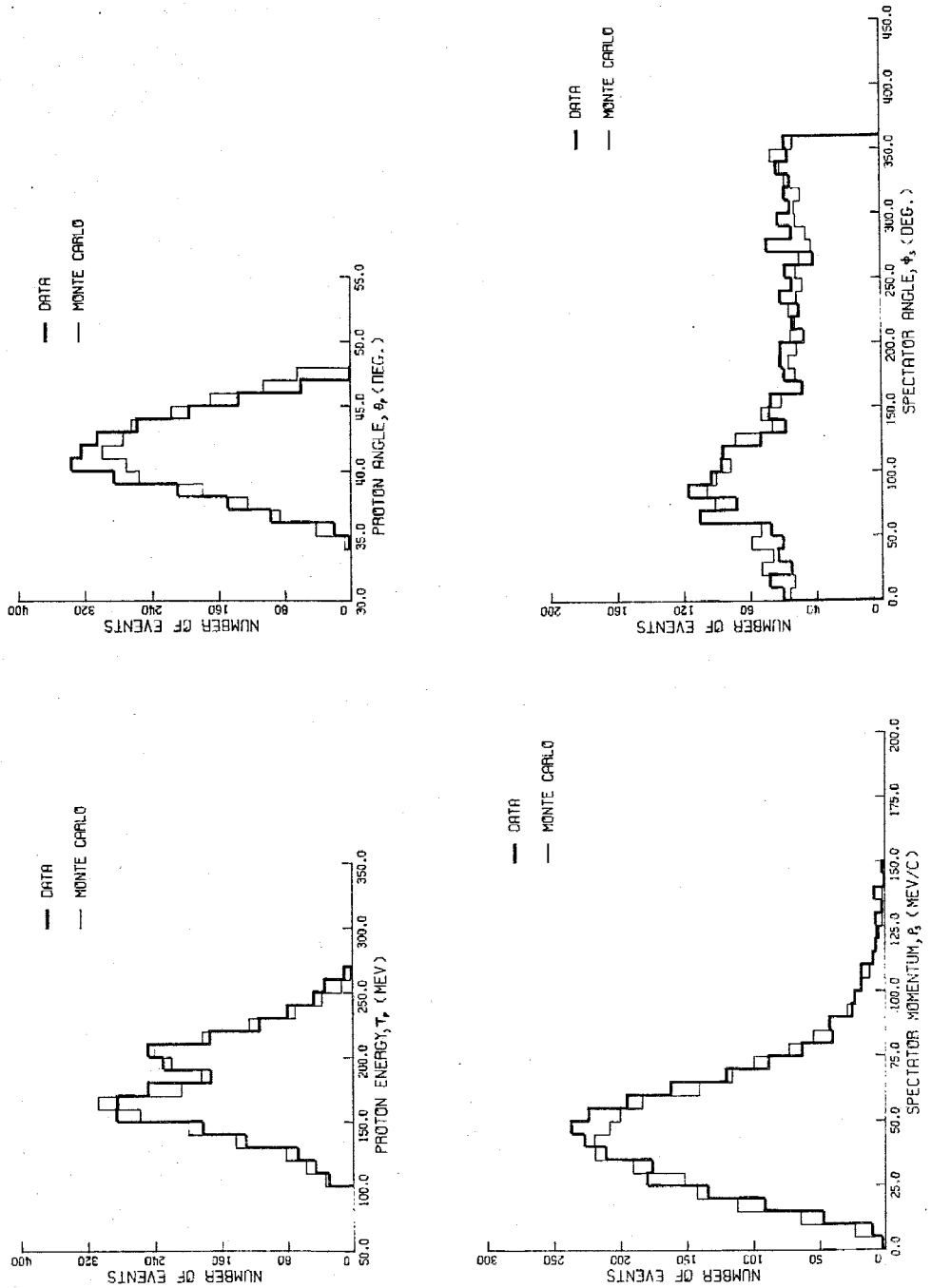
DATA AND MONTE CARLO MODEL COMPARISON DISTRIBUTIONS
650 MEV - 90 DEG. SET
DATA
MONTE CARLO
NUMBER OF EVENTS
PROTON ENERGY, T_p (MEV)
PROTON ANGLE, θ_p (DEG.)
SPECTATOR MOMENTUM, p_s (MEV/C)
SPECTATOR ANGLE, ϕ_s (DEG.)

FIGURE 4

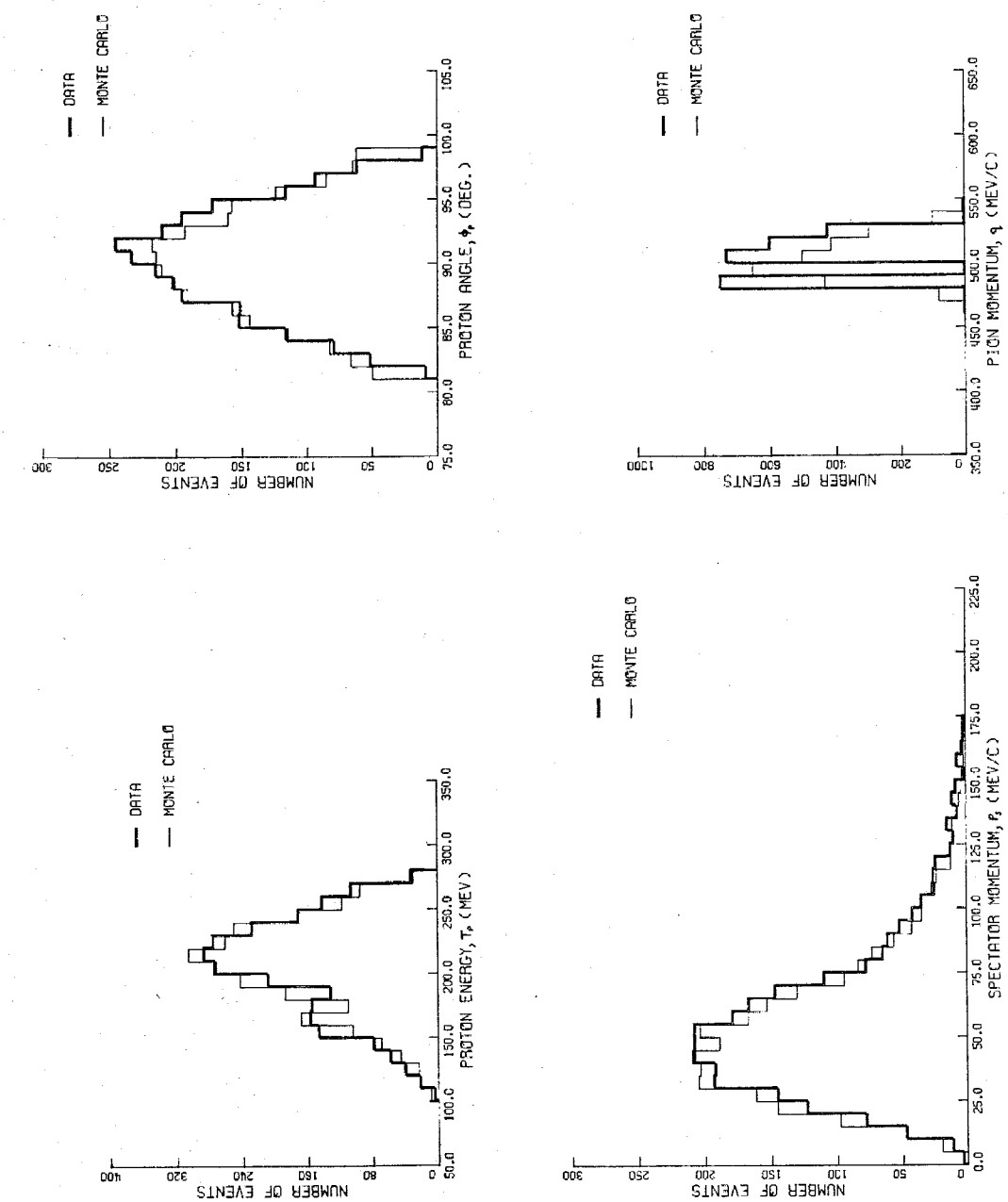
DATA AND MONTE CARLO MODEL COMPARISON DISTRIBUTIONS
750 MEV - 90 DEG. SET
DATA
MONTE CARLO
NUMBER OF EVENTS
PROTON ENERGY, T_p (MEV)
PROTON ANGLE, ϕ_p (DEG.)
PION MOMENTUM, q (MEV/C)
SPECTATOR MOMENTUM, P_s (MEV/C)

FIGURE 5

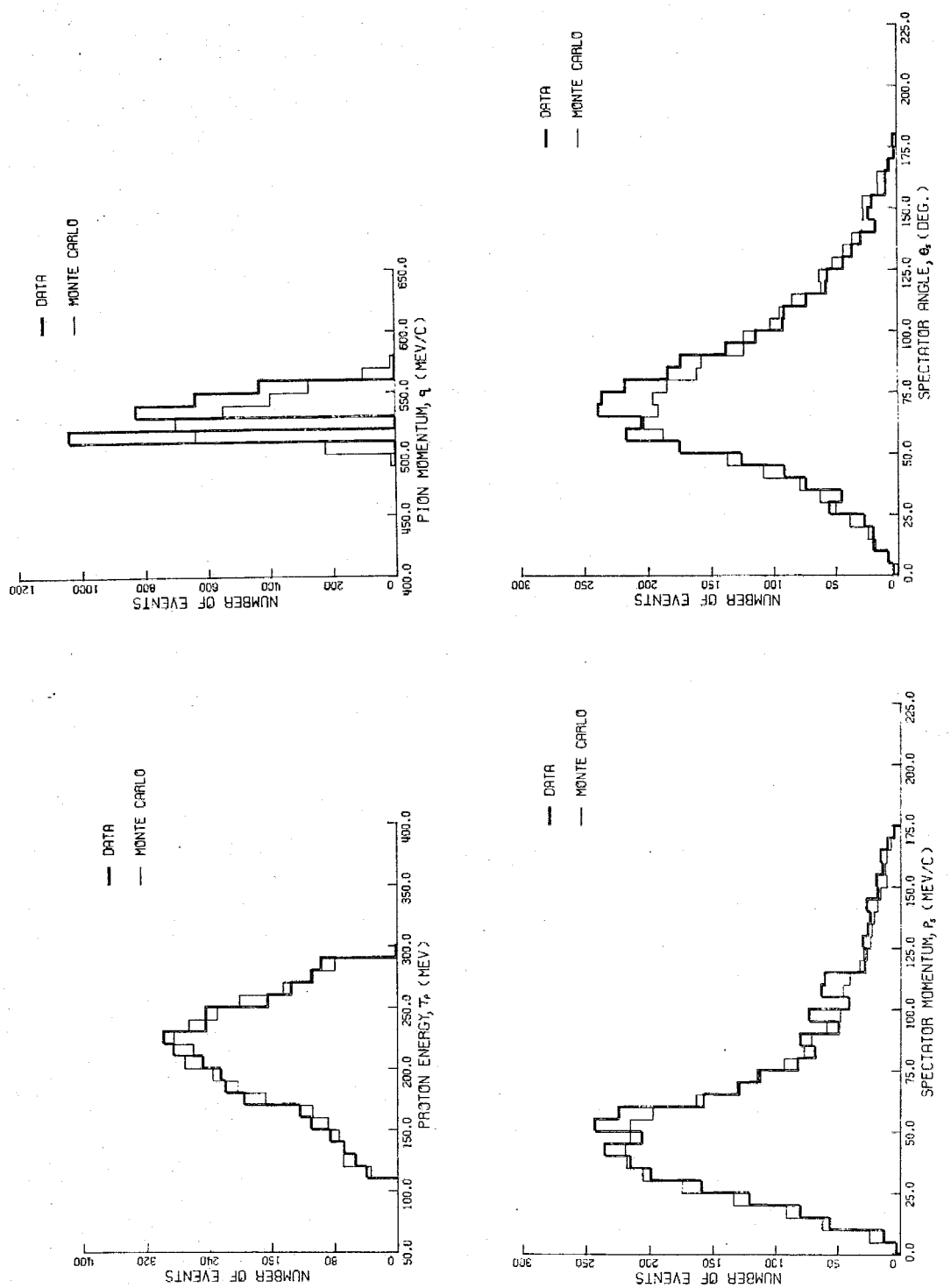
DATA AND MONTE CARLO MODEL COMPARISON DISTRIBUTIONS
800 MEV - 90 DEG. SET
DATA
MONTE CARLO
NUMBER OF EVENTS
PION MOMENTUM, q (MEV/C)
PROTON ENERGY, T_p (MEV)
SPECTATOR ANGLE, θ_s (DEG.)
SPECTATOR MOMENTUM, P_s (MEV/C)

FIGURE 6

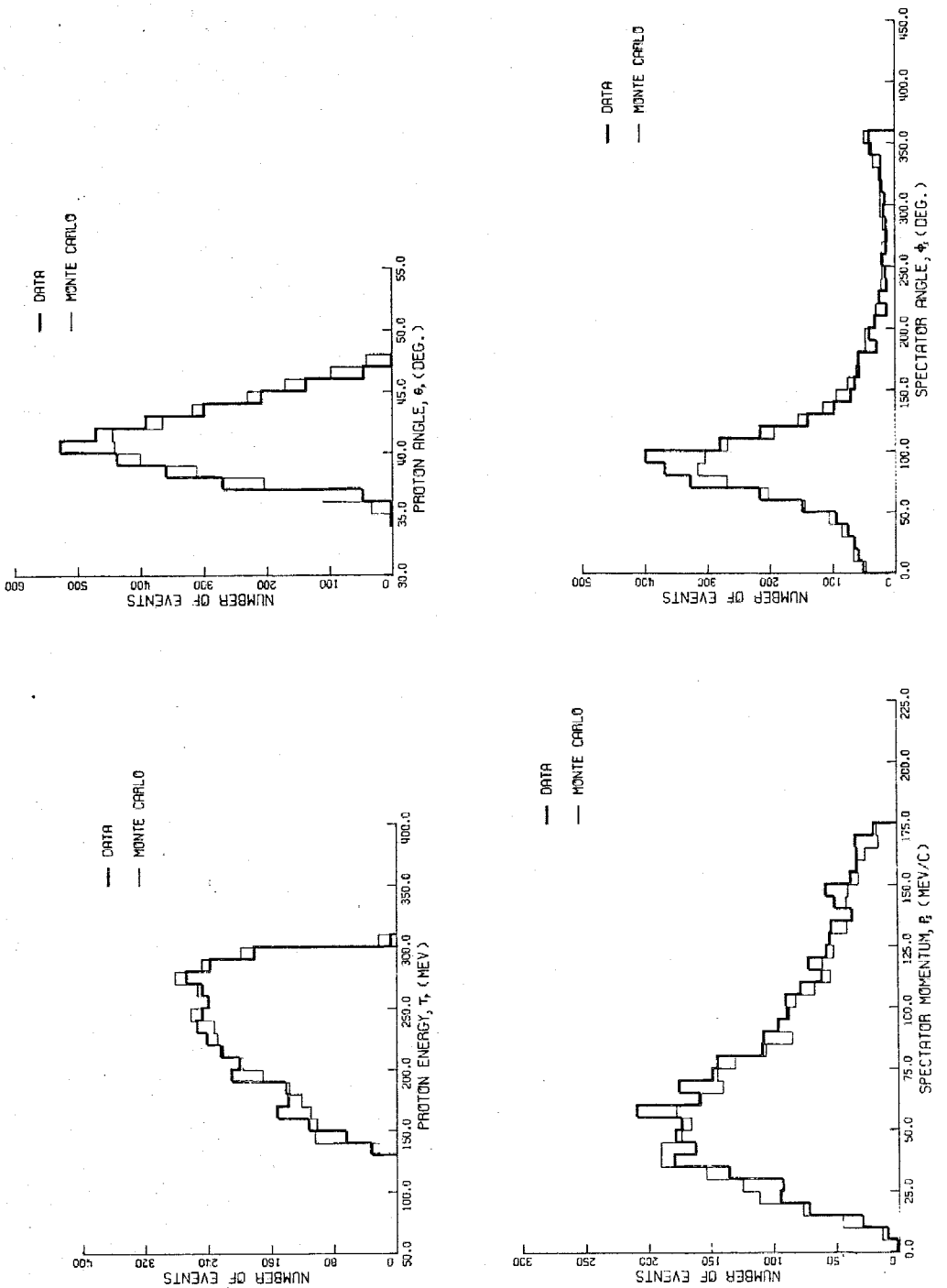
DATA AND MONTE CARLO MODEL COMPARISON DISTRIBUTIONS
900 MEV - 90 DEG. SET
DATA
MONTE CARLO
NUMBER OF EVENTS
PROTON ENERGY, T, (MEV)
PROTON ANGLE, θ, (DEG.)
SPECTATOR MOMENTUM, p, (MEV/C)
SPECTATOR ANGLE, φ, (DEG.)

FIGURE 7

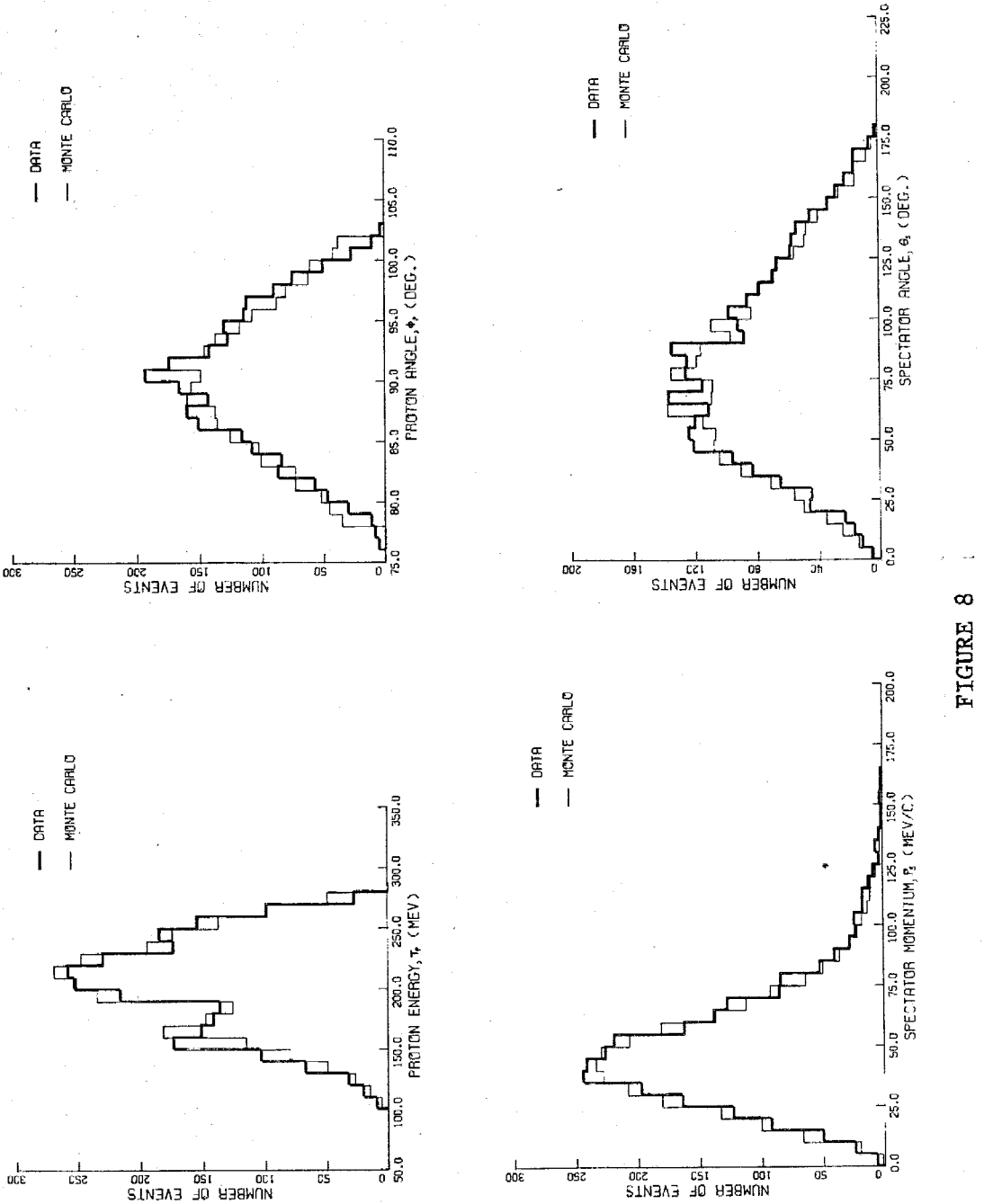
DATA AND MONTE CARLO MODEL COMPARISON DISTRIBUTIONS
550 MEV - 120 DEG. SET
DATA
MONTE CARLO
NUMBER OF EVENTS
PROTON ENERGY, T_p (MEV)
PROTON ANGLE, ϕ_p (DEG.)
SPECTATOR MOMENTUM, P_s (MEV/C)
SPECTATOR ANGLE, θ_s (DEG.)

FIGURE 8

DATA AND MONTE CARLO MODEL COMPARISON DISTRIBUTIONS

650 MEV - 120 DEG. SET

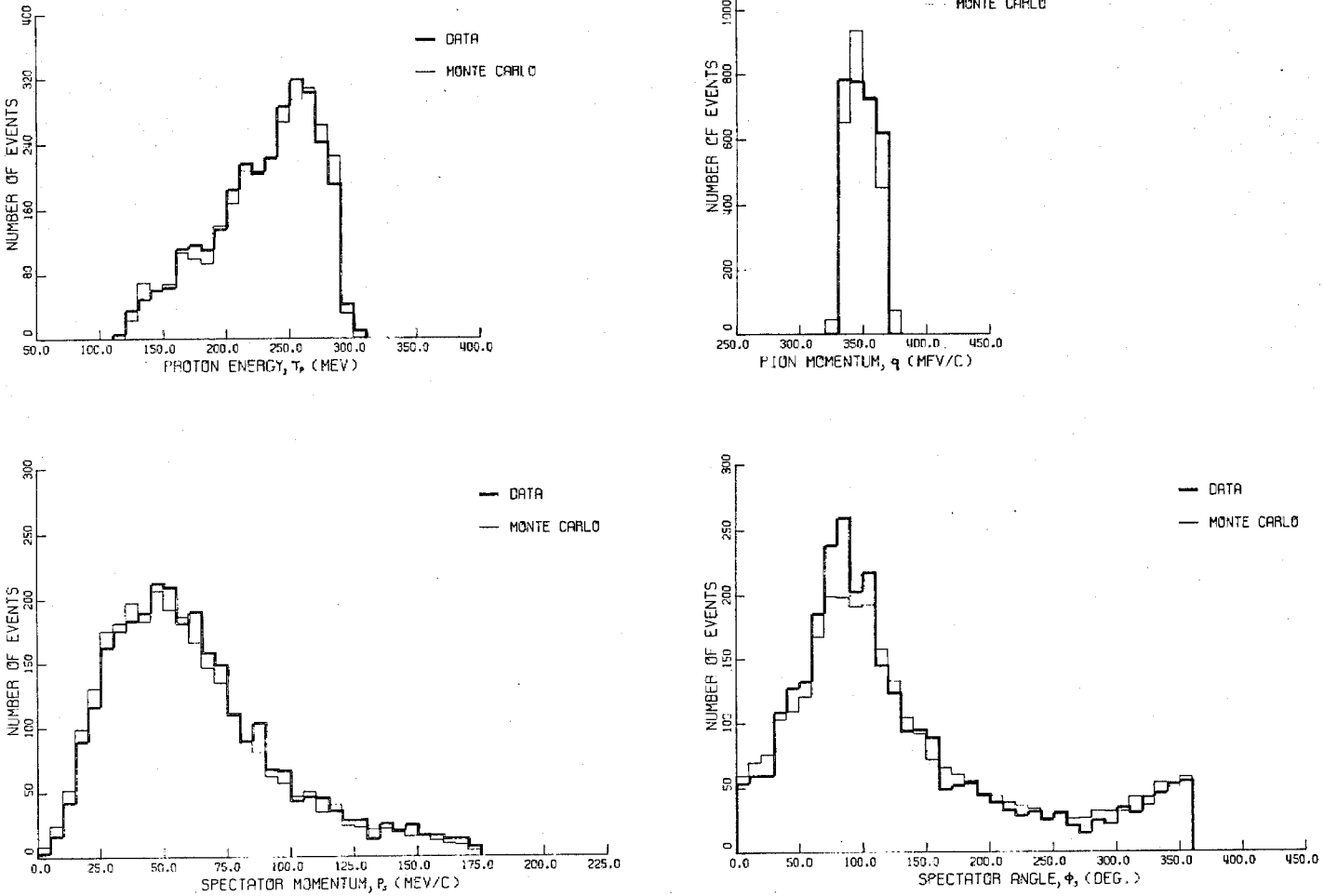

FIGURE 9

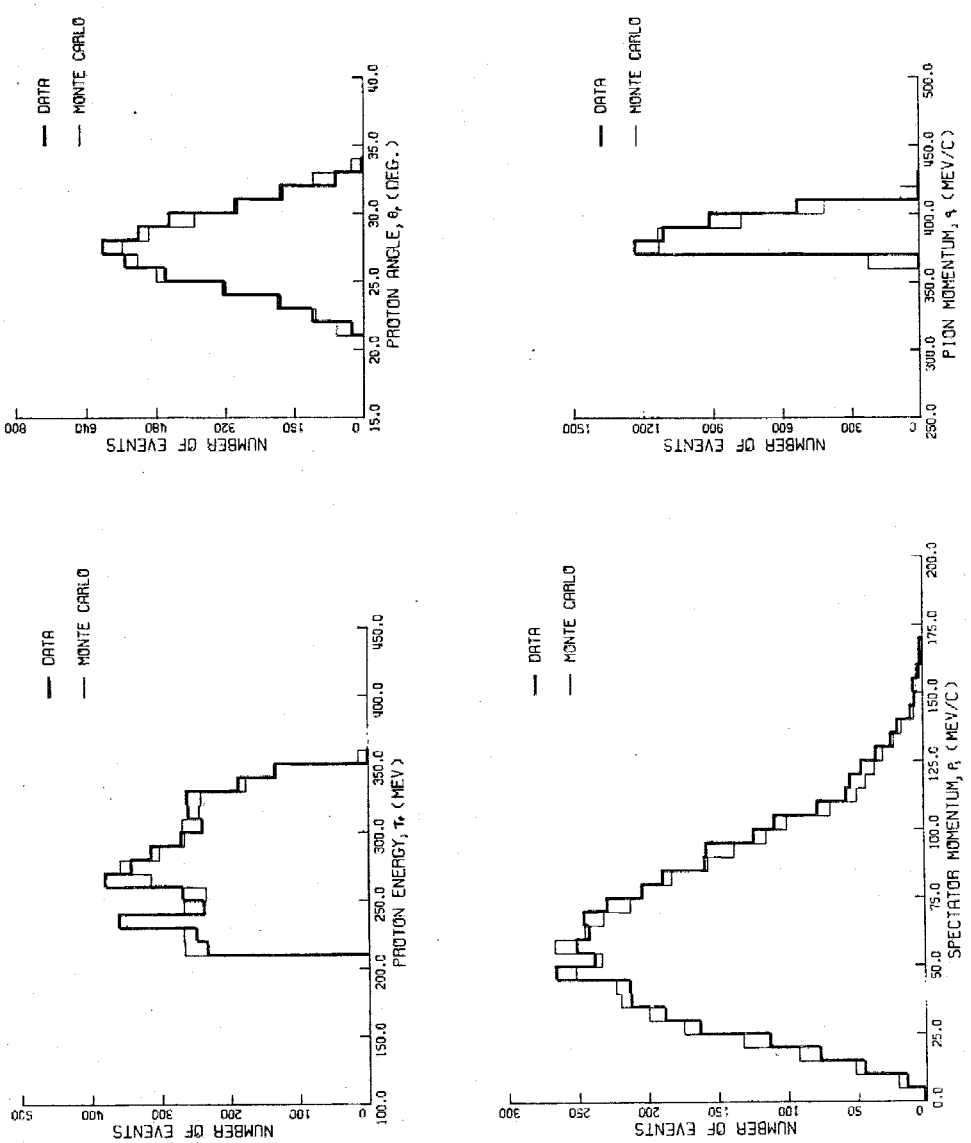
DATA AND MONTE CARLO MODEL COMPARISON DISTRIBUTIONS
750 MEV - 120 DEG. SET
DATA
MONTE CARLO
NUMBER OF EVENTS
PROTON ENERGY, T_p (MEV)
PROTON ANGLE, θ_p (DEG.)
PION MOMENTUM, q (MEV/C)
SPECTATOR MOMENTUM, q (MEV/C)

FIGURE 10

DATA AND MONTE CARLO MODEL COMPARISON DISTRIBUTIONS

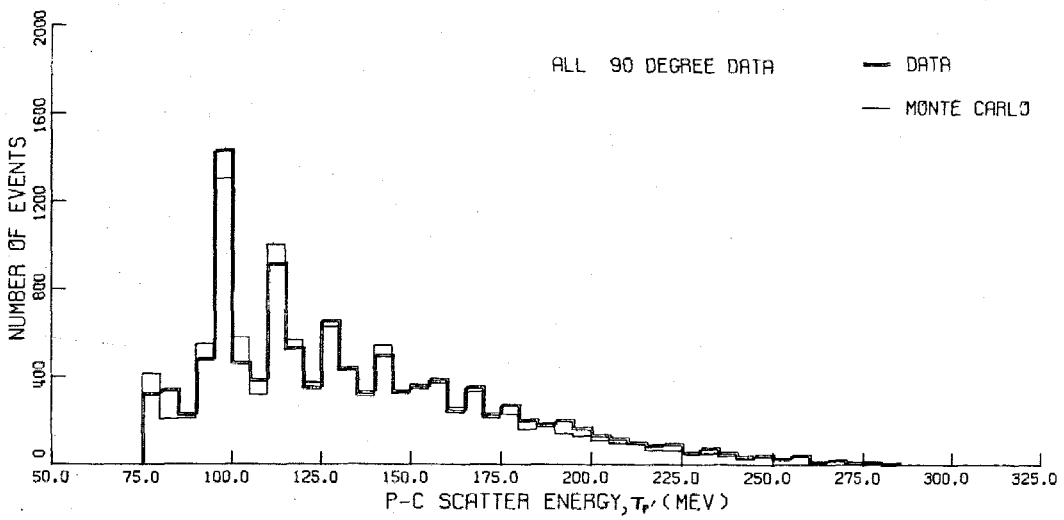

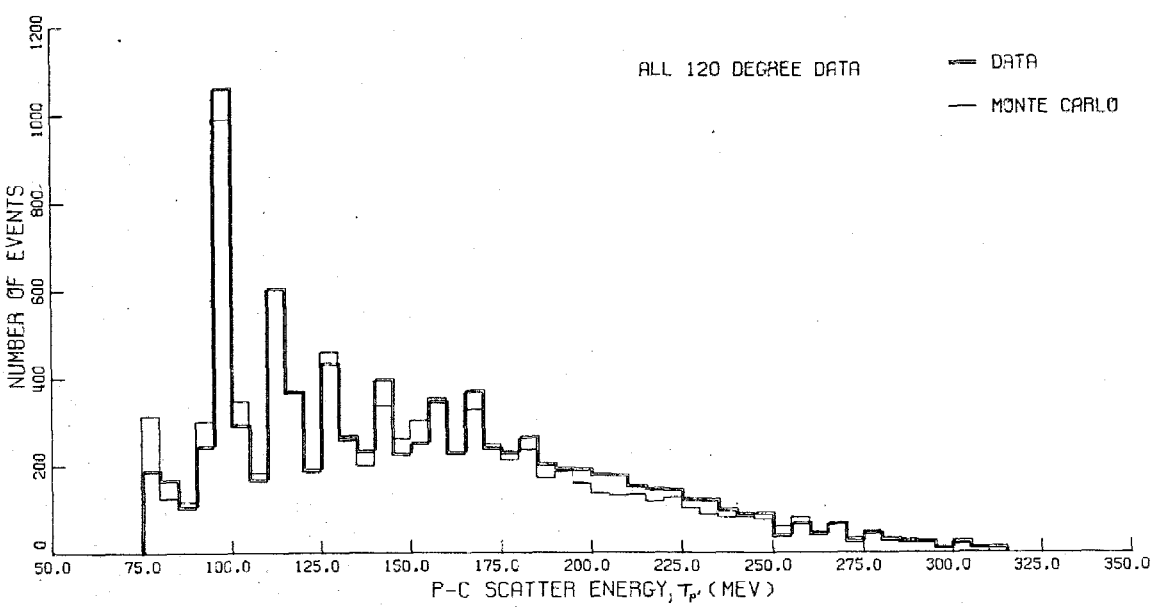

FIGURE 11

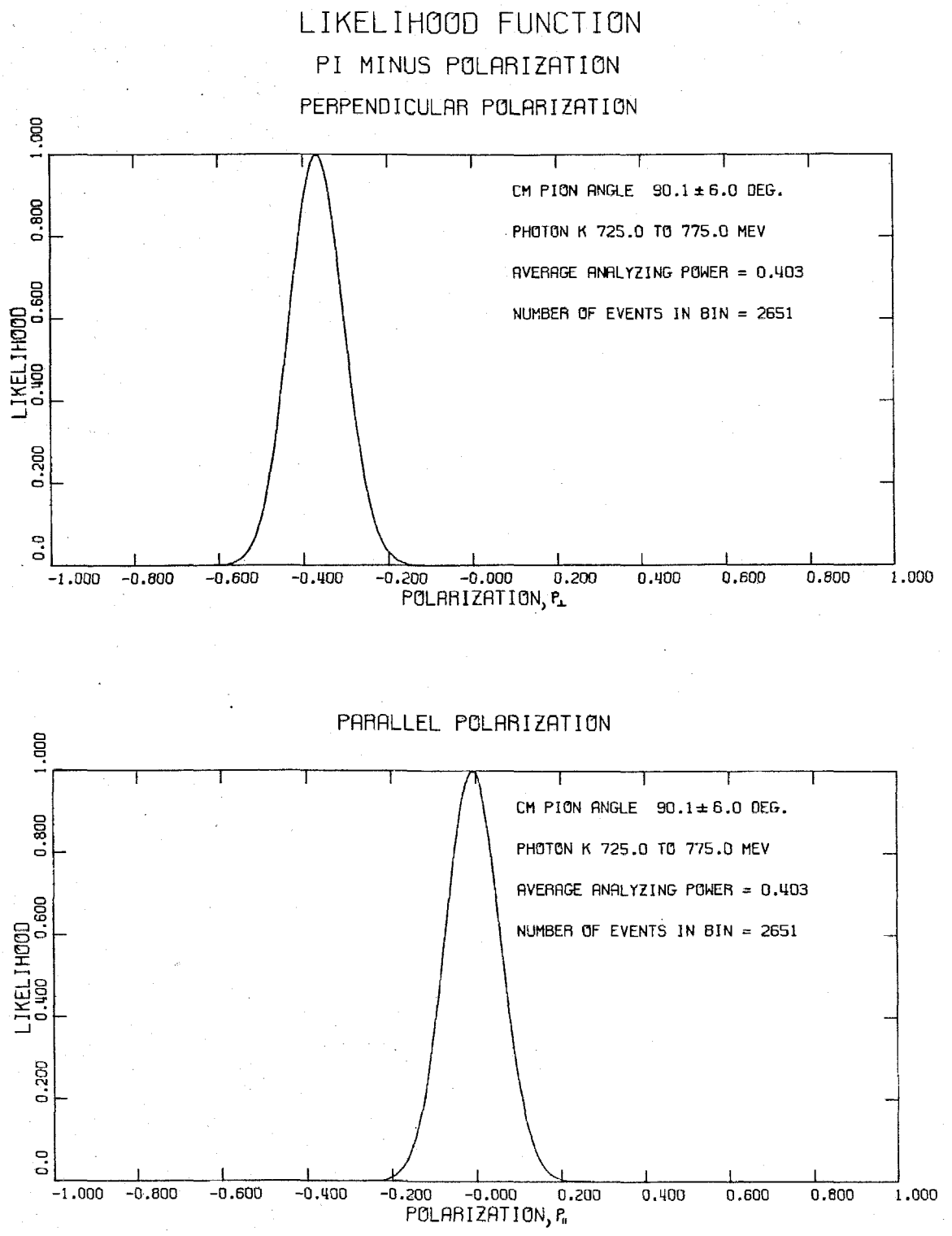
LIKELIHOOD FUNCTION
PI MINUS POLARIZATION
PERPENDICULAR POLARIZATION
CM PION ANGLE 90.1 ± 6.0 DEG.
PHOTON K 725.0 TO 775.0 MEV
AVERAGE ANALYZING POWER = 0.403
NUMBER OF EVENTS IN BIN = 2651
LIKELIHOOD
0.0
0.200
0.400
0.600
0.800
1.000
-1.000
-0.800
-0.600
-0.400
-0.200
-0.000
0.200
0.400
0.600
0.800
1.000
POLARIZATION, $P_\perp$
PARALLEL POLARIZATION
CM PION ANGLE 90.1 ± 6.0 DEG.
PHOTON K 725.0 TO 775.0 MEV
AVERAGE ANALYZING POWER = 0.403
NUMBER OF EVENTS IN BIN = 2651
LIKELIHOOD
POLARIZATION, $P_\parallel$

FIGURE 12

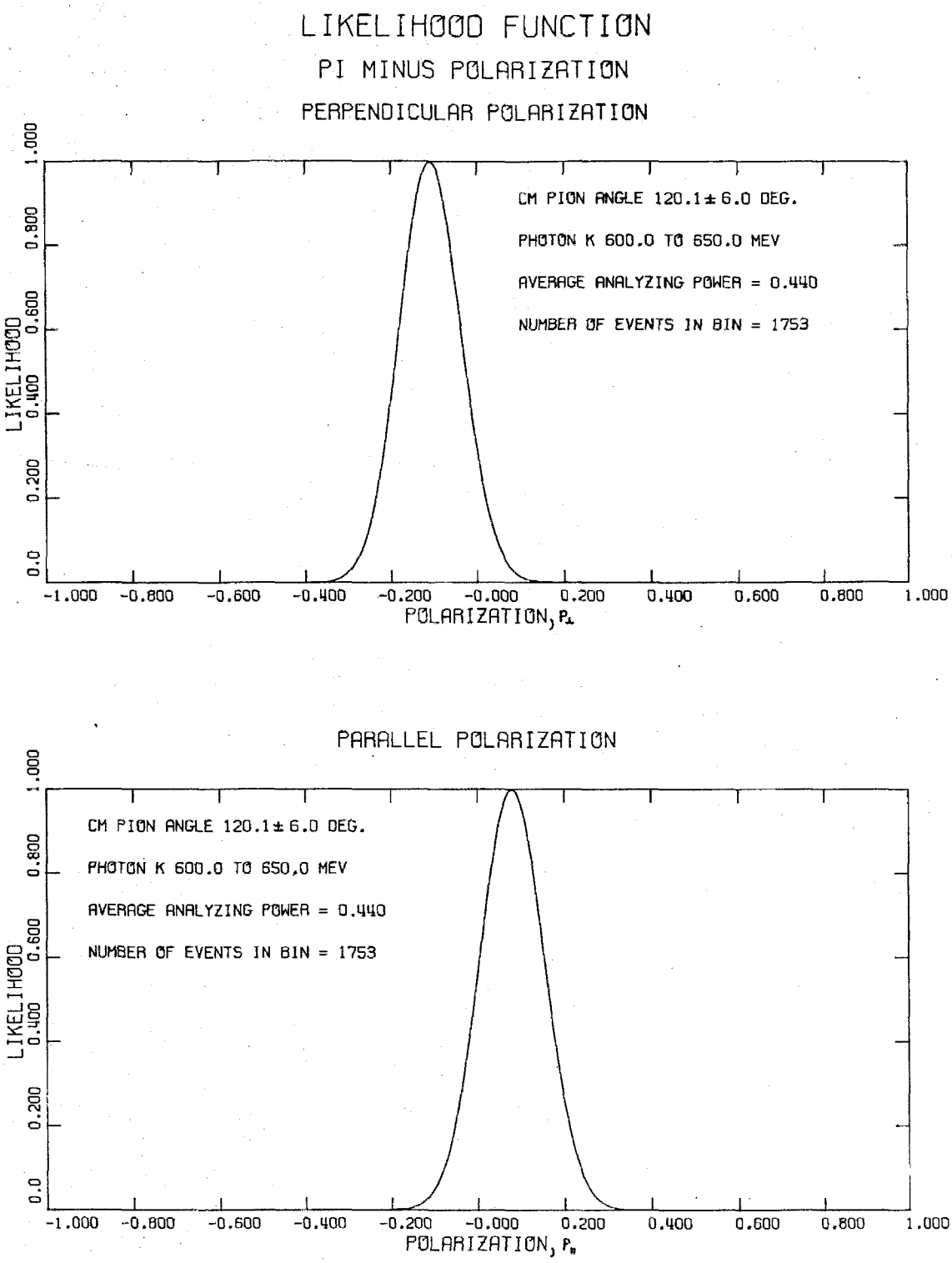
LIKELIHOOD FUNCTION
PI MINUS POLARIZATION
PERPENDICULAR POLARIZATION
CM PION ANGLE 120.1 ± 6.0 DEG.
PHOTON K 600.0 TO 650.0 MEV
AVERAGE ANALYZING POWER = 0.440
NUMBER OF EVENTS IN BIN = 1753
LIKELIHOOD
0.0
0.200
0.400
0.600
0.800
1.000
-1.000
-0.800
-0.600
-0.400
-0.200
-0.000
0.200
0.400
0.600
0.800
1.000
POLARIZATION, $P_\perp$
PARALLEL POLARIZATION
CM PION ANGLE 120.1 ± 6.0 DEG.
PHOTON K 600.0 TO 650.0 MEV
AVERAGE ANALYZING POWER = 0.440
NUMBER OF EVENTS IN BIN = 1753
LIKELIHOOD
POLARIZATION, $P_\parallel$

FIGURE 13

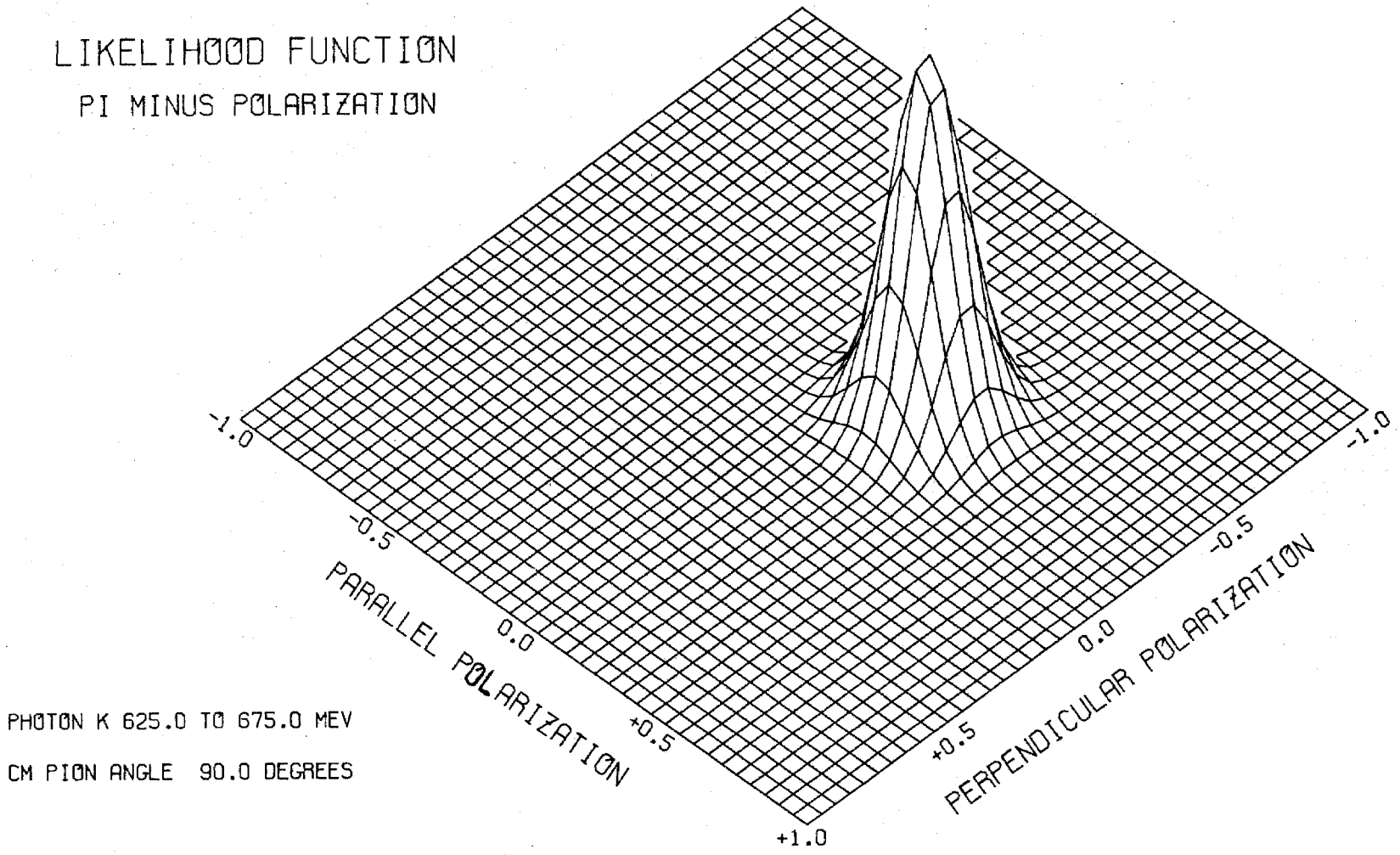
LIKELIHOOD FUNCTION
PI MINUS POLARIZATION
PHOTON K 625.0 TO 675.0 MEV
CM PION ANGLE 90.0 DEGREES
PARALLEL POLARIZATION
-1.0
-0.5
0.0
+0.5
+1.0
PERPENDICULAR POLARIZATION
-1.0
-0.5
0.0
+0.5

FIGURE 14

4. RESULTS

The Fermi momentum of the neutron means that perfect two-body kinematics do not hold in the reaction $\gamma n \rightarrow \pi^- p$ observed from deuterium. This, in turn, causes some ambiguity in exactly which variables to use in reporting the polarization results. In photoproduction from hydrogen the variables generally chosen are the CM angle of the pion and the laboratory photon energy. In order to use analogous variables in the deuterium case, we focus attention on the CM frame of the pion and the recoil proton. The angle between the pion and the incident photon, θ_π^{CM}, in this frame will be one of the variables used in reporting the results.* Next, let W be the total energy of the pion and the recoil proton in this frame, and let k_N be defined as the energy that a photon would need in striking a free neutron at rest in order to give the observed value of W. k_N is then analogous to the laboratory photon energy in photoproduction from hydrogen and is used as the other variable in reporting our results.

4.1 The Polarizations

With these definitions for k_N and θ_π^{CM}, the recoil polarization results for this experiment are given in Table 3. These results are also shown in Figures 15 and 16. The data for all of the kinematical settings at a given CM pion angle have been grouped together and then divided into bins of 50 MeV in k_N and the polarization values calculated for each bin (see Section 3.4).

*In fact, this angle, θ_π^{CM}, has been referred to somewhat loosely as the CM pion angle throughout this thesis. The connection is now made more precise.

In our analysis we actually calculated the value of $P_\perp$ along $\hat{k}\times\hat{p}_R$ (Figure 2). However, in order to be consistent with the preferred notation, the results in Table 3 give the value of $P_\perp$ with respect to $\hat{k}\times\hat{q}$. Since the kinematics are not quite those of a two-body reaction, $\hat{k}\times\hat{p}_R = -\hat{k}\times\hat{q}$ is only an approximation, and a small error (less than 1 per cent) is made in simply reversing the sign of $P_\perp$, as has been done. This error has been added to the statistical errors. Since the direction of $P_\parallel$ has no particular significance, its sign has not been reversed in going to the $\hat{k}\times\hat{q}$ plane.

The effects which can give a non-zero value for $P_\parallel$ (see Sections 2.3 and 3.4) are felt to be quite small in this experiment. Thus, it is reassuring that in almost every case the resulting value of $P_\parallel$ is within one standard deviation (in the statistical error) of zero.

4.2 Systematic Errors

The errors $\Delta P_\perp$ and $\Delta P_\parallel$ given in Table 3, as well as the error bars shown in Figures 15-18, include only the statistical error in the likelihood calculation and the small error involved in reversing the sign of the polarization. Table 3 also quotes an estimated systematic error for each bin and the sources of this error will now be discussed.

One contribution to the systematic error is the contamination due to backgrounds. The various backgrounds have been discussed in Section 2.4 and in Appendix B. The only potentially serious ones -- 2π photoproduction and electron contamination in the spectrometer -- were both found to be at most 1 per cent effects when a coincidence is required between the pion and the recoil proton. Empty target back-

grounds are believed, on the basis of empty target counting rates, to be negligible.

The other important contribution to the systematic error is the resolution in the various quantities that determine the polarization, namely $\cos \phi_{p'}$ and $A_c(T_{p'}, \theta_{p'})$ (see Section 3.4). The resolution in $\cos \phi_{p'}$ (quoted in Table 3) is felt to be reasonably good, especially for those scatters with larger analyzing powers ($\theta_{p'} \gtrsim 8^o$).

The resolution in analyzing power comes from three sources: (1) the errors in the experimental data on the carbon analyzing power; (2) the resolution errors in the quantities $T_{p'}$ and $\theta_{p'}$, of which the analyzing power is a function; and (3) the indeterminacy of the inelasticity in the p-C scatters. The error due to each source is discussed in Appendix E. Except in cases where the uncertainty in the initial trajectory is large, the unknown inelasticity of the p-C scatters, which can lead to an uncertainty of the order of 20 per cent in the analyzing power, dominates all the other systematic errors.

The systematic errors quoted in Table 3 are an estimate for each bin of the maximum probable combined effect of these errors in either direction. The best method in which to eliminate the dominant contribution to this error -- the undetermined inelasticity of the p-C scatters -- in future work would be to use beams of known photon energy such that the kinematics are overdetermined and the inelasticity of each scatter therefore measurable within a few MeV. The large error in the initial trajectory for certain events could have been avoided with a set of hodoscope chambers placed in front of any carbon used.

4.3 Comparison to Other Experiments

The only other measurements of the recoil proton polarization for the reaction $\gamma n \rightarrow \pi^- p$ are those of Beneventano, et al. [31], and Kenemuth and Stein [30]. Both are at $\theta_\pi^{CM} = 90^o$ in the region 500 MeV $\leq k_N \leq$ 725 MeV. These data are plotted in Figure 17 along with the 90^o results of the present experiment. The bin widths in energy are indicated in this figure. The results within the region of overlap appear to be reasonably consistent within the statistical errors. The only exception is the 700 - 90^o point which may be a little high in the present experiment.

Figure 18 compares our results to the values predicted by a recent phenomenological fit to photoproduction data [15]. The results of this experiment were <u>not</u> used in obtaining these fits and they are, therefore, a valid prediction of our results. The agreement is fairly impressive in most cases. This shows that the polarization values measured in this experiment are generally consistent with what other data exist on the reaction $\gamma n \rightarrow \pi^- p$ and on the related photoproduction reactions $\gamma p \rightarrow \pi^+ n$ and $\gamma p \rightarrow \pi^o p$.

In the next section, this procedure will be reversed, and our results used in an attempt to improve the phenomenological analysis of this reaction. Thus, the discrepancies in Figure 18 (especially in the $\theta_\pi^{CM} = 90^o$ curve) may give new information on the nucleon resonances contributing to this polarization.

TABLE 3. Polarization Values

Kinematical Bins and Widths				Average Values for Bins		Polarization along $\hat{k} \times \hat{q}$		Polarization in $\hat{k} \times \hat{q}$ Plane		Estimated Systematic Error* (%)
k_N	Δk_N	θ_π^{CM}	$\Delta\theta_\pi^{CM}$	$\langle k_N \rangle$	$\langle \theta_\pi^{CM} \rangle$	$P_\perp$	$\Delta P_\perp$	$P_\parallel$	$\Delta P_\parallel$	
600	± 25	90°	± 6°	609.0	90.3	.10	.20	-.18	.20	21.0
650	"	"		650.1	90.3	-.23	.10	.21	.10	18.5
700	"	"		702.5	90.2	-.02	.09	-.09	.09	20.0
750	"	"		750.8	90.1	-.37	.07	0.0	.07	18.5
800	"	"		798.7	90.4	-.52	.07	-.06	.07	18.0
850	"	"		847.7	90.9	-.78	.08	.06	.08	18.0
900	"	"		895.6	90.9	-.68	.12	-.07	.12	18.5
950	"	"		938.9	90.3	-.27	.30	-.14	.30	21.0
475	± 25	120°	± 6°	487.5	120.6	.62	.34	.32	.34	19.5
525	"	"		529.4	120.4	.13	.11	.10	.11	19.5
575	"	"		574.0	120.3	.21	.08	-.09	.08	19.5
625	"	"		626.4	120.1	-.11	.08	.08	.08	20.0
675	"	"		674.7	119.8	-.17	.07	-.08	.07	20.0
725	"	"		721.3	119.8	-.62	.08	-.05	.08	22.0
775	"	"		764.2	119.6	-.88	.18	.04	.18	21.0

*This estimate is likely to be too small as the polarization approaches zero, and the systematic error is always felt to be at least of the order of 0.07.

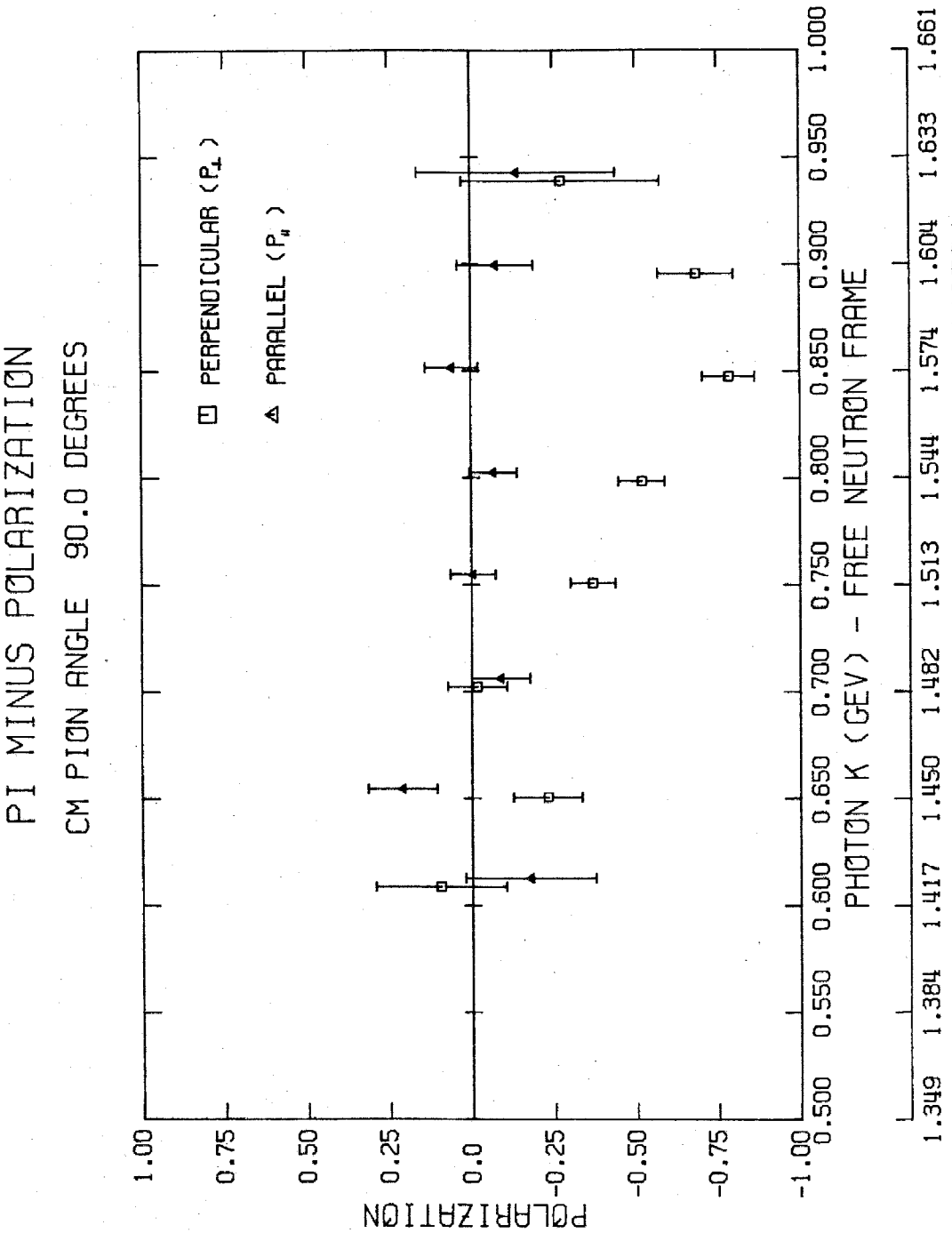
PI MINUS POLARIZATION
CM PION ANGLE 90.0 DEGREES
PERPENDICULAR (P⊥)
PARALLEL (P∥)
POLARIZATION
1.00
0.75
0.50
0.25
0.0
-0.25
-0.50
-0.75
-1.00
0.500 0.550 0.600 0.650 0.700 0.750 0.800 0.850 0.900 0.950 1.000
PHOTON K (GEV) - FREE NEUTRON FRAME
1.349 1.384 1.417 1.450 1.482 1.513 1.544 1.574 1.604 1.633 1.661
CM ENERGY (GEV) - OF PION, RECOIL PROTON

FIGURE 15

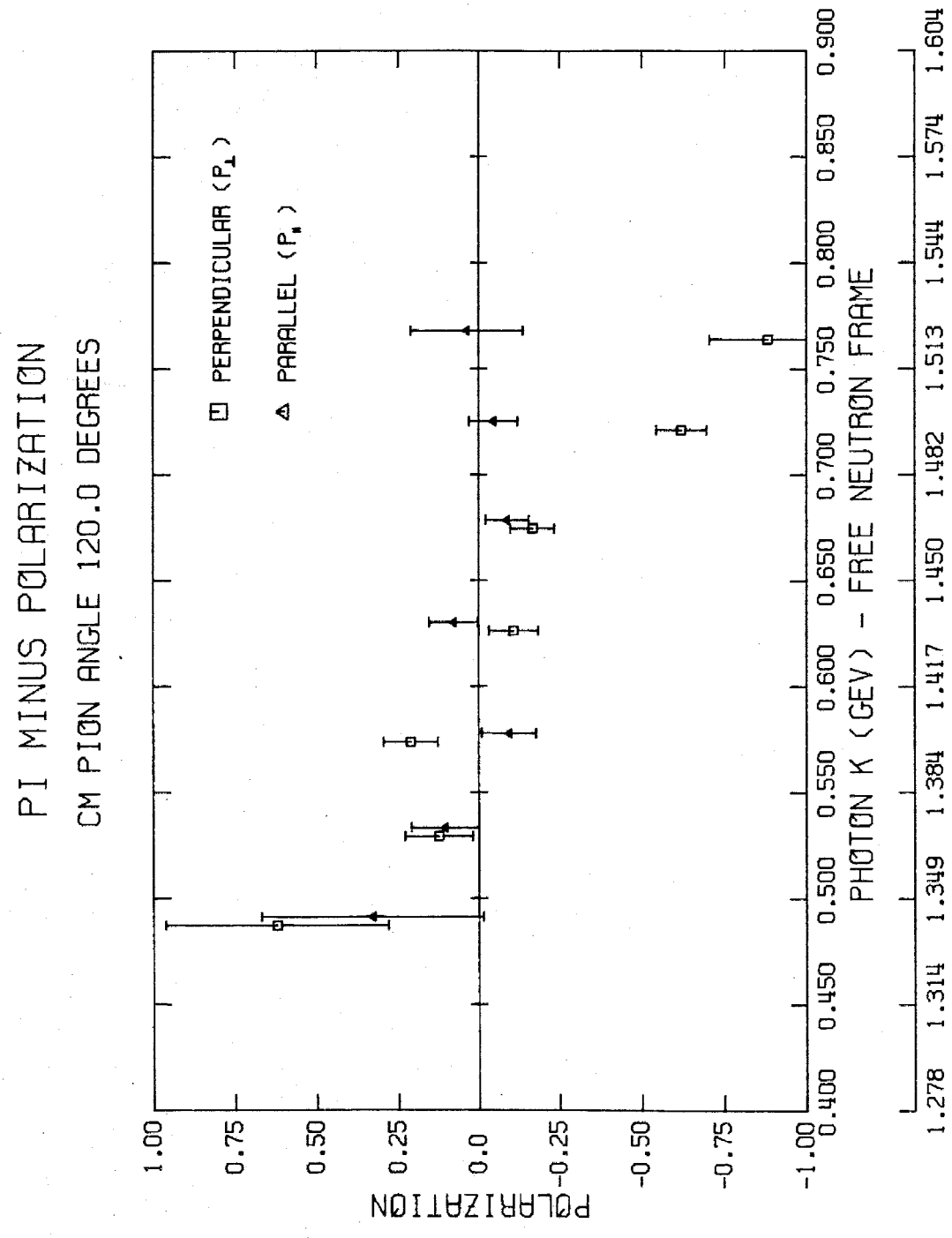
PI MINUS POLARIZATION
CM PION ANGLE 120.0 DEGREES
PERPENDICULAR (P⊥)
PARALLEL (P∥)
POLARIZATION
1.00
0.75
0.50
0.25
0.0
-0.25
-0.50
-0.75
-1.00
0.400 0.450 0.500 0.550 0.600 0.650 0.700 0.750 0.800 0.850 0.900
PHOTON K (GEV) - FREE NEUTRON FRAME
1.278 1.314 1.349 1.384 1.417 1.450 1.482 1.513 1.544 1.574 1.604
CM ENERGY (GEV) - OF PION, RECOIL PROTON

FIGURE 16

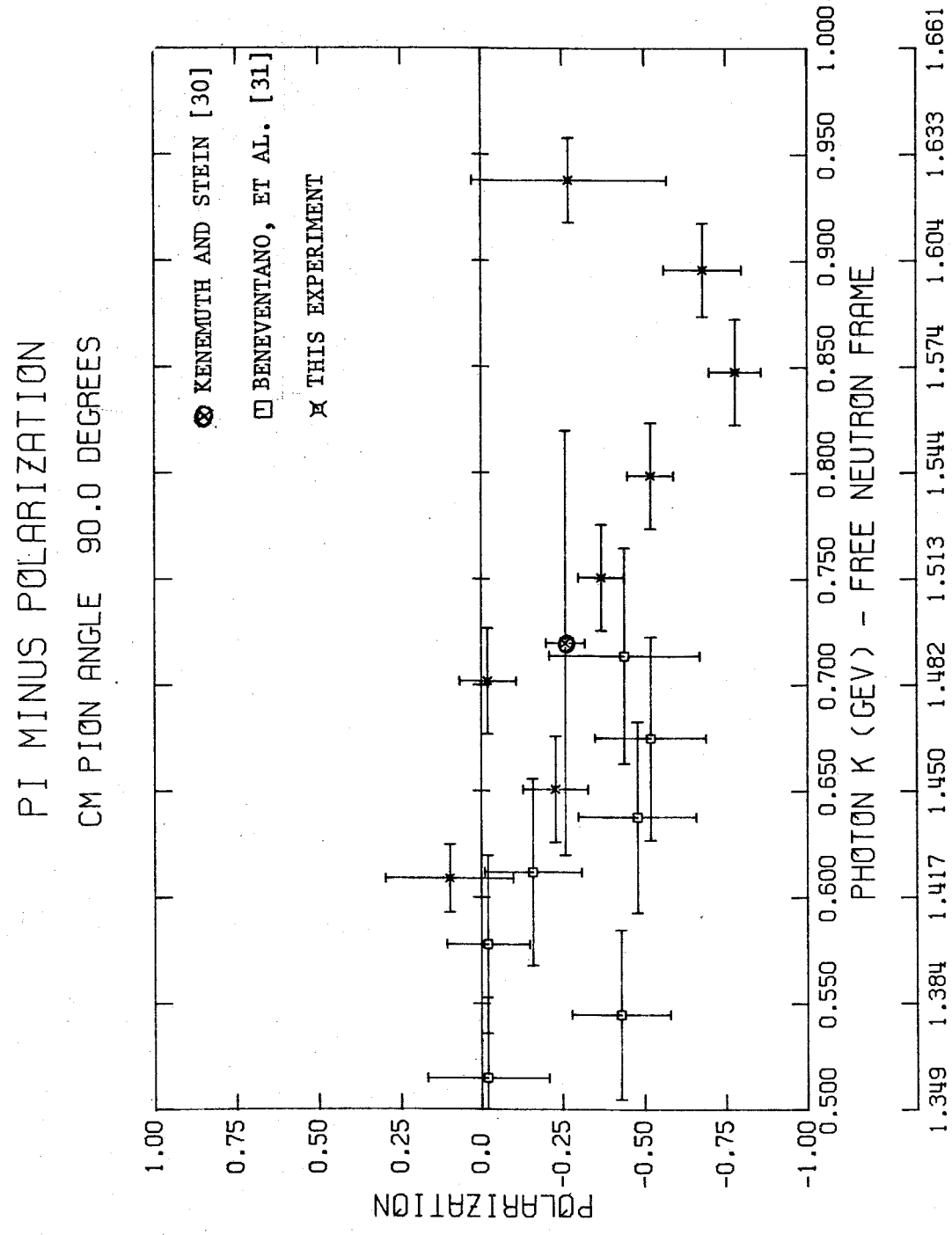

FIGURE 17 Comparison to Other Experiments

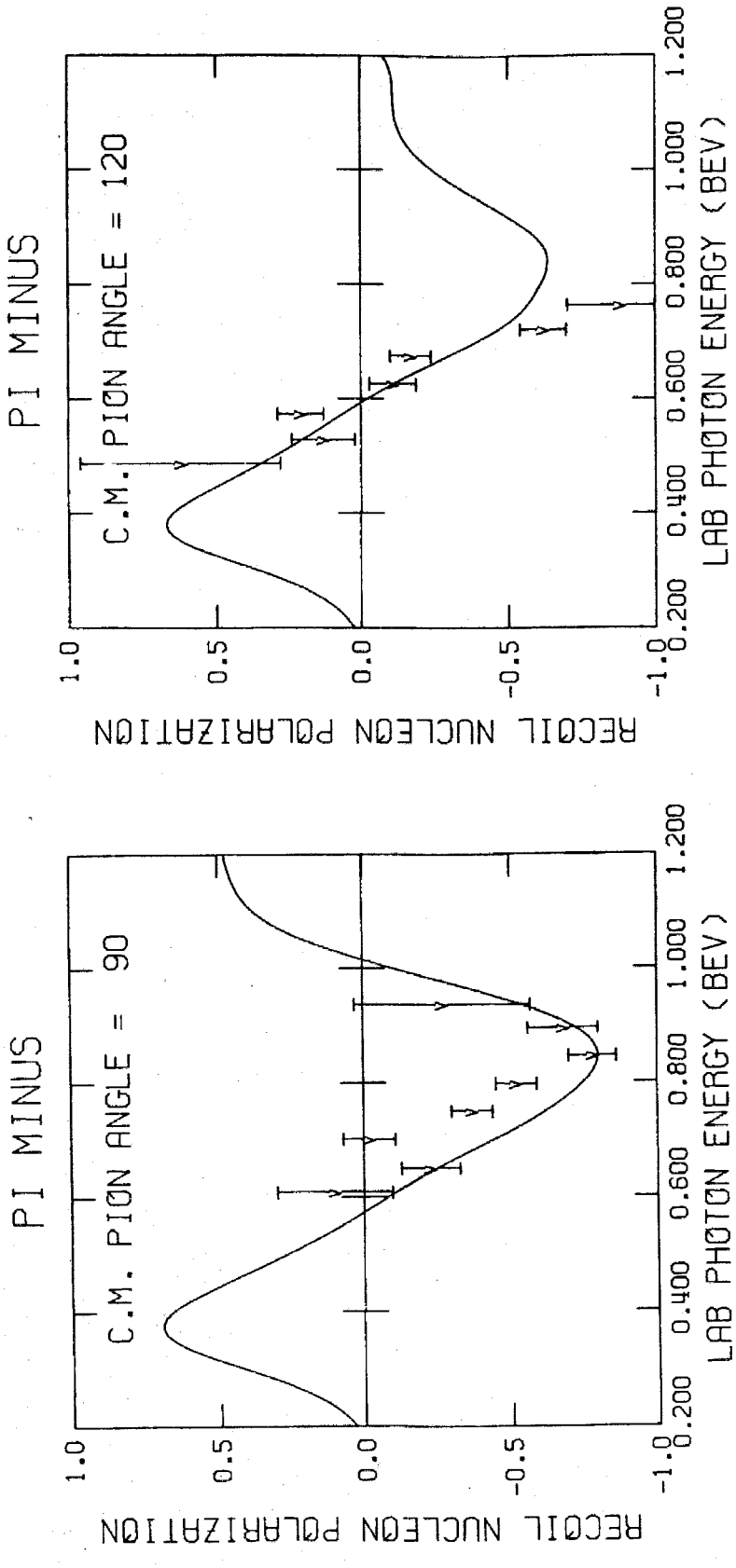

FIGURE 18

Comparison to Phenomenological Fit in Reference [15]

5. PHENOMENOLOGY OF π^- PHOTOPRODUCTION

Having obtained a set of values for the recoil proton polarization in the reaction $\gamma n \rightarrow \pi^- p$, we shall now see to what extent these values make possible a better determination of the electromagnetic couplings of certain I = 1/2 nucleon resonances. The first part of this section describes the model of pion photoproduction that will be used to describe the π^- data. This is followed by a discussion of the actual fitting procedure and the results that were obtained by the present analysis. In the last part of this section a very brief sketch is given of how the quark model can be used to predict the electromagnetic couplings of nucleon resonances. The results of one such quark model calculation are introduced and compared to the values obtained in the fitting analysis in order to see how well this model describes the photoproduction of these resonances.

5.1 The Model

Photoproduction phenomenology has been actively pursued for the past decade, and there are as many models as there are groups engaged in this research. Most of these models use some physical principle (dispersion relations, resonance saturation, etc.) to limit the number of parameters used to fit the typically sparse and frequently inconsistent data on photoproduction. These models fall into two main groups depending on whether or not dispersion relations are used.

Early dispersion relation models [10, 11, 12] generally projected fixed-t dispersion relations into multipole amplitudes to obtain a set of coupled equations which could then (in principle) be solved

self-consistently without reference to any data. Such calculations, though quite successful at least in the low energy region, were necessarily approximate (using assumptions such as the dominance of the M_{1+} multipole in first resonance region) and were constantly being adjusted to accommodate new data. More recent work with dispersion relations [14, 34] frequently assumes resonance saturation of the imaginary part of the photoproduction amplitudes and then uses a fixed-t dispersion relation (with a pion pole term) to obtain the real part. In one of these models [14] some of the "resonances" -- i.e., poles in the K-matrix -- occur outside the physical region so "resonance saturation" is not completely realized. However, the use of the K-matrix formalism allows the effect of other channels to be properly taken into account.

Models not using dispersion relations [9, 15, 32, 33] employ a Breit-Wigner form for the resonances and include complex background terms in the partial waves. The exact Breit-Wigner form used depends on the model, the main difference being the inclusion of an arbitrary phase (with respect to the Born terms) in some cases [32, 33]. The background terms may be essentially free parameters [32, 33] or may be constrained to vary smoothly (to some degree) in energy [9, 15]. The background terms are limited to the lower partial waves ($j \leq 5/2$ or $7/2$) with the electric Born terms (Figure 19b) supplying the contribution of the higher partial waves. The one exception to Breit-Wigner resonances in these models [32] is the use of a K-matrix formalism for the A_{0+} amplitude in the second resonance region in order to properly describe the η-

threshold. The present analysis uses the same model as reference [15] with strictly Breit-Wigner resonances and smoothly varying background terms.

The reaction $\gamma n \rightarrow \pi^- p$ will be analyzed in the center of mass frame in terms of the helicity amplitudes $A_{\mu\lambda}$ where μ is the final helicity along the pion direction and λ is the initial helicity along the photon direction* (see Figure 19a). Although there are eight such amplitudes in pion photoproduction, only four of them are independent. This is because conservation of parity in the strong and electromagnetic interactions demands that [9]

$$A_{-\mu,-\lambda}(\theta,\phi) = -e^{i(\lambda-\mu)(\pi-2\phi)} A_{\mu,\lambda}(\theta,\phi) \quad . \tag{5.1}$$

The various experimentally measurable quantities describing this reaction -- the cross section, the recoil proton polarization, the polarized photon symmetry, and the polarized target asymmetry -- are then expressible in terms of these amplitudes. Precise definitions of these experimental observables are given in Appendix F. This appendix also contains expressions for these quantities in terms of helicity amplitudes $A_{\mu\lambda}$.**

The helicity amplitudes are then partial wave analyzed in terms of helicity coefficients $a_{\mu\lambda}(W)$. This partial wave analysis is summarized by the expression [9, 35]

---

*If λ_k, λ_i, and λ_f are the helicities of the photon, initial nucleon, and final nucleon respectively, then $\mu = -\lambda_f = 1/2, -1/2$, and $\lambda = \lambda_k - \lambda_i = 3/2, 1/2, -1/2, -3/2$.

**The $A_{\mu\lambda}$ are understood to be functions of the total CM energy, W, and the CM angles of the pion, θ and ϕ.

$$A_{\mu\lambda}(W, \theta, \phi) = \sum_j a^j_{\mu\lambda}(W)(2j+1)d^j_{\lambda\mu}(\theta)e^{i(\lambda-\mu)\phi} \quad . \tag{5.2}$$

The helicity coefficients are re-expressed in terms of helicity elements which describe final states of definite parity and are, therefore, more useful in the present analysis. These helicity elements $A_{\ell\pm}$ and $B_{\ell\pm}$ are related to the helicity coefficients by the following expressions

$$\begin{aligned} A_{\ell\pm} &= \mp 1/\sqrt{2}\,(a^j_{1/2,\,1/2} \pm a^j_{-1/2,\,1/2}) \\ B_{\ell\pm} &= \pm\sqrt{2/n(n+2)}\,(a^j_{1/2,3/2} \pm a^j_{-1/2,3/2}) \quad (\ell \geq 1) \end{aligned} \tag{5.3}$$

In these expressions ℓ is the relative orbital angular momentum of the pion and the nucleon in the final state. The parity of these helicity elements is thus $-(-1)^\ell$. The quantity $n = j - 1/2$ and $j = \ell \pm 1/2$ for $\ell\pm$ respectively. The elements $A_{\ell\pm}$ obviously refer to states with initial helicity 1/2 and the $B_{\ell\pm}$ to states with initial helicity 3/2 (and thus $\ell \geq 1$).

We are now in a position to describe the various components of the photoproduction model used in the present analysis and how they contribute to the helicity amplitudes.

The first contribution comes from the electric Born terms represented by the diagrams in Figure 19b. In these diagrams, e signifies the minimal electromagnetic coupling and g the πN coupling (see Appendix F. 3). The magnetic Born terms, which arise from the anomalous magnetic moments of the strongly interacting particles, are not explicitly included in this analysis since they contribute significantly only to the lower partial waves ($j \leq 7/2$) where the other com-

ponents of the model are expected to dominate. The electric Born terms, especially the pion pole term, are included primarily to take care of the contribution of higher partial waves ($j \geq 7/2$) not included in the other components of the model. However, no attempt is made to explicitly "absorb out" their contribution to the lower partial waves. Explicit expressions for the contribution of the diagrams in Figure 19b to the helicity amplitudes $A_{\mu\lambda}$ are given in Appendix F.3.

The next contribution is that of the resonances. A particular resonance, $(L)_{2I2J}$,* will contribute to either the A_{L+} (and B_{L+} if $j \geq 3/2$) helicity element or the A_{L-} (and B_{L-} if $j \geq 3/2$) helicity element depending on J . For example, a D_{13} resonance contributes to the A_{2-} and B_{2-} helicity elements, while a D_{15} resonance contributes to the A_{2+} and B_{2+} elements. (Recall that L ± means $j = L \pm 1/2$.)

The contribution to a given helicity element of a particular resonance is given explicitly in Appendix F. 4 . It is a modified Breit-Wigner form. The resonances used in this analysis are listed in Table 4 along with the values of the various parameters that appear in this Breit-Wigner expression. Only resonances with $j \leq 7/2$ are used. The masses and widths of the resonances are taken from πN scattering phase shift analyses with slight modifications resulting from a recent phenomenological analysis of the reactions $\gamma p \rightarrow \pi^+ n$ and $\gamma p \rightarrow \pi^o p$ [15]. The statistics and the resolution in such data are far superior to those in the present reaction and, therefore, no attempt is made to adjust these parameters in the present analysis.

---

*In this notation J is the spin and I the isospin of the resonance. L is the final orbital angular momentum if the resonance decays into a πN final state.

The couplings* of the I = 3/2 nucleon resonances to the reactions $\gamma n \rightarrow \pi^- p$, $\gamma p \rightarrow \pi^+ n$ and $\gamma p \rightarrow \pi^o p$ are simply related by isospin conservation (see Section 1). Therefore, the values of these couplings determined from an analysis [15] of these latter two reactions are used (again because the π^+ and π^o data are more numerous and of a better quality). No significant evidence for any change in these values was found in the present analysis.

The couplings of the I = 1/2 nucleon resonances are of course varied and their determination is the main goal of this analysis. They are <u>not</u> varied in the sense that a computer program varies them to minimize a χ^2. Only the backgrounds (as discussed below) are varied in this manner. Depending on the resulting shapes of these backgrounds, however, the I = 1/2 resonance couplings are changed in a manner described in Section 5.2 to obtain the "best" values. The main point is that the model attempts to relate any rapid energy variation in the data to resonant behavior and to remove such variations from the backgrounds by modifying the couplings of the resonances.

The addition of our Breit-Wigner resonances to each other (when they occur in the same partial wave) and to the background terms without the use of a K-matrix formalism means, among other things, that the effect of other channels is not properly taken into account [36]. Except in the case of the effect of the η-threshold on the

---

* The "coupling" of a resonance to a particular helicity element is equal to its contribution (purely imaginary) to this element at the resonance energy (see Appendix F.4).

A_{o+} amplitude, this failure to use the K-matrix is not expected to be a serious problem. Some compensation for this effect may be expected to show up in the background, but would be difficult to distinguish as such.

The above mentioned background terms are the last component of the model. Independent real and imaginary background terms are included for each helicity element up to $j = 7/2$ and $\ell = 4$. They account for any non-resonant contribution to the reaction without being too precise about the source of this contribution. Such a contribution could arise from, for example, the tails of resonances outside of the region covered by the analysis, absorption of the electric Born terms in the lower partial waves, or the contribution of the magnetic Born terms. The only assumption made is that these background terms vary smoothly in energy compared to the energy variations due to the resonances. The hope is to isolate any rapid energy variations in the experimental data in terms of the contribution of the resonances and in this way rather accurately determine the coupling of these resonances to the reaction $\gamma n \rightarrow \pi^- p$. The parameterization used to ensure a smooth energy variation in the backgrounds is discussed in Appendix F. Briefly, it consists of specifying the value of each background term at each of seven reference energies (see Table 5) and then using a smooth interpolation to get the value at any other energy.

Since the present analysis begins above several inelastic thresholds, no attempt is made to enforce Watson's theorem [37] on any of the amplitudes. Each resonant and background term contains a proper threshold dependence, but since we begin well above threshold

these factors are not important. Finally, since the effect of the η-threshold is felt to be below the present resolution in the $\gamma n \rightarrow \pi^- p$ data, it is not explicitly taken into account; however, some effect of this threshold might be expected to appear in the A_{o+} background, at least to the extent that the data "know" about this threshold.

5.2 The Fitting Procedure

The procedure by which the above model was used to obtain fits to the data on the reaction $\gamma n \rightarrow \pi^- p$ is basically the same that was used in several previous analyses [9, 15]. It will now be described in outline form.

(1) Data on this reaction were collected at intervals of 50 MeV in laboratory photon energy, k_L, from k_L = 400 MeV to 1200 MeV. The region below 400 MeV was not included because it is completely dominated by the $P_{33}(1236)$ resonance whose coupling to photoproduction is very well determined by the low energy data on the reaction $\gamma p \rightarrow \pi^o p$ [9, 14, 15]. The π^- data in this region are internally inconsistent and of poor resolution. Above 1200 MeV the data are too scarce to permit any significant analysis. The types of data used were cross sections,* recoil proton polarizations, and polarized photon asymmetries. A precise definition of each of these experimental quantities is given in Appendix F. Table 14 gives a list of all of the experiments from which data were taken along with the symbol by which the data from a particular experiment are distinguished in

*Data on π^-/π^+ ratios from deuterium are also used. These data are converted into π^- cross sections by multiplying by the π^+ cross sections determined in reference [15].

Figures 20-26.

(2) The background terms were all set to zero initially by specifying zero values at the reference energies. The couplings of the I = 1/2 resonances were also set to zero. The couplings of the I = 3/2 resonances were fixed at the values determined from analysis of the reactions $\gamma p \rightarrow \pi^+ n$, $\pi^o p$ [15]. The electric Born terms were included in the amplitudes.

Then, at each energy where a fit was made (i.e., every 50 MeV beginning at 400 MeV), the amplitudes $A_{\mu\lambda}$ are computed from these pieces and used to calculate the theoretical value of each data point. From these theoretical values and the experimentally measured values (and their errors) a total χ^2 for that energy is obtained.

(3) The background terms Re A_{o+}, Im A_{o+}, Re A_{1-}, Re B_{1+}, and Re B_{2-} were then allowed to vary in order to minimize this χ^2. The computer algorithm which performed this minimization was a modification of a program written by Paul Scheffler [22] and is outlined in Appendix F.6. The reason why only these backgrounds were allowed to vary at first is that they are the ones which tend to become large in any case*, and it was found that far more stable solutions were obtained in this manner.

In varying these backgrounds, their initial values were also

*The reason that these Re parts become large is that these are the helicity elements which have big contributions from the electric Born terms. In this reaction the Born terms tend to be largely absorbed out in the low partial waves and therefore the Re parts of these backgrounds have about the same size but are opposite in sign to the contribution of the Born terms.

included as data along with the experimental data points. This use of the "parameters as data" was the way in which the criterion of smooth backgrounds was enforced and was absolutely necessary if any consistency from energy to energy was to be maintained in the background terms in view of the fact that in the following steps, where all of the background terms were allowed to vary, the number of parameters was often greater than the number of experimental data points. Using the parameters as data tends to keep them close to their smoothly varying initial values unless a change causes a significant reduction in the χ^2 due to the experimental data to compensate the increase in χ^2 due to the change in the parameter. The errors assigned to the backgrounds when they were used as data were scaled such that a change of one standard deviation corresponded to a change of $(0.5)(1/2)^{j-\frac{1}{2}}$ μb in the differential cross section.

The resulting background terms were then plotted as functions of energy. These curves were checked for any energy variation interpretable as being due to one of the resonances. This variation was then removed by changing the coupling of this resonance. After the removal of such variations smooth curves were drawn through the resulting backgrounds and the values of these curves at the reference energies formed the new parameterization of these backgrounds.

(4) Using the new values for the background terms and the resonance couplings the helicity amplitudes were recalculated and a new set of initial χ^2's computed. The full set of background terms (up to $j = 7/2$, $\ell = 4$) were now allowed to vary in order to minimize

this χ^2 at each energy where a fit was made. The resulting backgrounds were again plotted and inspected for resonant behavior. After any such variations were removed by appropriate changes in the resonant couplings, smooth curves were drawn through all the backgrounds and the values of these curves at the reference energies again determined the new initial values for these backgrounds at all energies (see Appendix F. 5).

(5) Step (4) was repeated until the changes in the backgrounds in a given iteration were all within their errors or else varied so randomly from energy to energy (even after any variations attributable to the known resonances had been removed) that some smooth average had to be settled on. This stage was reached after some six to eight iterations.

(6) At this point a "fit" was made in which the backgrounds were not allowed to vary. The initial χ^2 and the values of the experimental observables at intervals of 10° in CM pion angle were calculated at each energy. If these quantities gave a reasonable description of the data, the fitting process was complete. If there was a serious disagreement with any of the experimental data, one or more of the backgrounds and/or resonances were forced to take on radically different values, based on an estimate of what the trouble was due to, and the search for a solution began again at step (4). Fortunately, this was not necessary in the present analysis.

The results of the present analysis of the reaction $\gamma n \to \pi^- p$ are contained in Tables 4 and 5. Table 4 gives the resulting resonant couplings. The errors quoted in these couplings were deter-

mined in the following, admittedly subjective, manner. Once the final solution had been obtained, the couplings of the various resonances were changed one at a time until the resonance began to show up in the corresponding background term. This procedure -- the only one readily available -- certainly gave an upper limit on these errors and often a far smaller change would induce undesirable features into the fits. Table 5 gives the values of the background terms at the selected reference energies. It will be noted that most of them are, indeed, smoothly varying in energy.

Table 6 gives the final χ^2 at each energy. To indicate how much of this χ^2 comes from inconsistencies in the data, this table also includes a quantity called χ^2_{free} which was obtained by allowing the final background terms to vary once a solution had been obtained. The fit obtained in this manner has no smooth behavior in energy but is usually as good a fit as can be obtained to the given data. To illustrate how good the fits obtained in the present analysis were, Figures 20 - 26 show the resulting fits to the experimental data for all types of data at various CM pion angles and lab photon energies throughout the region being studied. The experiment corresponding to each plotting symbol in these figures is listed in Table 14. In general, the resulting fits are at least as good as those of several previous analyses [9, 14, 15, 22] and often much better. The fits to the recoil proton polarization data are especially satisfying.

To demonstrate how much, if any, this analysis (with the new polarization data included) has improved the knowledge of the elec-

tromagnetic couplings of the I = 1/2 nucleon resonances, Table 7 compares the results of the present analysis to several other analyses.* The results indicate a significant change in several of the couplings and an improved resolution in many of these couplings.

5.3 The Quark Model

Among the first to use an L-excitation quark model to calculate the electromagnetic decay widths of nucleon resonances were Faiman and Hendry [1]. Their non-relativistic model, with harmonic oscillator potentials binding the quarks, has been the basis of several successful descriptions of many of the features of photoproduction in the resonance region, notably those of Copley, et al. [2] and Walker [3]. None of these calculations, however, include the important recoil term [39]. In principle, such a term is easily incorporated in a non-relativistic model, but recent interest has centered on the relativistic model of Feynman, et al. [4]. More will be said below about this important model, to which the present results on the electromagnetic couplings of several nucleon resonances will be compared.

In a simple version of this model [1, 2, 3] the baryon is viewed as being a composite of three quarks bound to each other by harmonic oscillator potentials. The state of the baryon is then a combination of a space state describing the excitation of the oscillators, a total spin state (each quark having spin 1/2), and an internal charge-strangeness state given by SU(3). The total state is assumed to be symmetric

*The table includes the results for $\gamma p \rightarrow \pi^+ n$ from reference [15] in order that statements may be made on the isoscalar-isovector character of these resonances (see Section 6).

under the group S_3, i. e., under permutation of any two of the quarks. As is well known [24], the possible SU(3) states of three quarks fall in the following representations: a $\underset{\sim}{1}$ anti-symmetric, A, under the group S_3; a $\underset{\sim}{10}$ symmetric, S, under S_3; and two $\underset{\sim}{8}$'s of mixed symmetry, M, under S_3. Similarly, the total SU(2) states of three spin 1/2 particles fall into a $\underset{\sim}{4}$ (s = 3/2) of S symmetry under S_3, and two $\underset{\sim}{2}$'s (s = 1/2) of M symmetry under S_3. The total spin-internal wave function of the baryon is found by combining these pieces, a process made far simpler by use of the Clebsch-Gordan series for S_3 [38]. When this is done, the results are found to fall into the following SU(6) representations: a $\underset{\sim}{20}$ of A symmetry under S_3 and of SU(3) (SU(2)) components $\underset{\sim}{8}$ (1/2) and $\underset{\sim}{1}$(3/2); a $\underset{\sim}{56}$ of S symmetry under S_3 and components $\underset{\sim}{10}$ (3/2) and $\underset{\sim}{8}$ (1/2); and two $\underset{\sim}{70}$'s of M symmetry under S_3 and each with components $\underset{\sim}{10}$ (1/2), $\underset{\sim}{8}$(3/2), $\underset{\sim}{8}$ (1/2), and $\underset{\sim}{1}$ (1/2). In pion photoproduction we deal with only non-strange particles so any pieces containing an SU(3) $\underset{\sim}{1}$ will not be of interest nor will many of the states in the $\underset{\sim}{8}$'s and the $\underset{\sim}{10}$.

If the space states of the oscillators are studied, after the CM motion is removed, the following pattern emerges [38]. The ground state (N = 0) obviously has total angular momentum L = 0 and is symmetric, S, under S_3. The first level of excitation (N = 1) has L = 1 and A symmetry under S_3. For N = 2 there are many more possibilities: two sets of L = 2 states of M symmetry under S_3; a set of L = 2 states of S symmetry under S_3; a set of L = 1 states of A symmetry under S_3; two L = 0 states of M symmetry under S_3; and a L = 0 state of S symmetry. Since we are interested only in the lower

lying nucleon resonances, we stop at this level of excitation. The parity of the space state is given by $P = (-1)^N$ since the ground state has even parity and each excitation is accomplished by a vector operator. The actual form of these space states, of course, depends on the dynamical model used for the oscillators.

The space states can now be combined with the SU(6) states to give all the possible low-lying baryon states in this model. This process is again simplified by use of the S_3 Clebsch-Gordan series and by the requirement that the total state have S symmetry under S_3. The results are summarized in Table 8, which also gives a tentative identification [4] of the corresponding nucleon resonance. The notation used in listing these states is $[SU(6), L^P]_N {}^{2S+1}SU(3)_J$ where N is the level of excitation, L^P are the total angular momentum and parity of the space state, and S is the total quark spin which combines with L to give total angular momentum, J , of the state.

With these states, the photoexcitability of various nucleon resonances in the process $\gamma N \to \pi N$ can be calculated using the diagram in Figure 27. Thus, the process is viewed as a photon exciting a nucleon ground state $[\underset{\sim}{56}, 0^+]_0 {}^2\underset{\sim}{8}_{1/2}$ into some resonance $[SU(6), L^P)]_N$ $^{2S+1}SU(3)_J$ which then decays back into the ground state by emitting a pion. The actual details of such calculations are determined by the dynamics used for the harmonic oscillator potentials (i.e., by the actual form of the space states) and by the expressions used for the interaction at the two vertices γNN^* and $N^*N\pi$.

Feynman, et al. [4] have carried out such calculations. In their model the dynamics of the oscillators and the interactions at the ver-

tices (in Figure 27) are treated in a relativistically invariant manner. Such calculations automatically include the important recoil term neglected in many non-relativistic calculations. The relativistic model also gives the expected even spacing in mass-squared for Regge recurrences of the baryon resonances. Therefore, in spite of certain problems, such as the need to use cut-offs to avoid violations of unitarity, this essentially one-parameter model is particularly interesting to compare to phenomenological data on the nucleon resonances.

In making such comparisons for the photoexcitation of nucleon resonances, what Feynman, et al. actually calculate are the electromagnetic decay widths, $A^N_{1/2}$ and $A^N_{3/2}$, which are the amplitudes for a given resonance to decay into a photon and a neutron in helicity states 1/2 and 3/2, respectively. These amplitudes are easily related to the couplings, A and B respectively, discussed above by separating out the contribution of the pion vertex into a pion decay width and a Clebsch-Gordan coefficient for $N^* \rightarrow p + \pi^-$. These relations are given explicitly in Appendix F.4.

Feynman's results for $A^N_{1/2}$ and $A^N_{3/2}$ are given in Table 9 along with the results of the present analysis for the I = 1/2 resonances and the results of reference [15] for the I = 3/2 resonances. The results are seen to be in quite good agreement for many of these resonances. The specific agreements and disagreements will be discussed in the next section, but in general it may be said that this very basic and essentially parameterless model gives a surprisingly good

description of the photoexcitation from neutrons* of many nucleon resonances.

*The pattern of agreements is quite similar for photoexcitation from protons [4, 14, 15].

TABLE 4. Resonance Parameters

This table contains, for each resonance included in the analysis, the values of the parameters appearing in the Breit-Wigner formula (Appendix F. 4). The couplings, $A^{-}[N^{*}]$ for the $A_{\ell\pm}$ helicity element and $B^{-}[N^{*}]$ for the $B_{\ell\pm}$ helicity element, are in units of $\mu b^{\frac{1}{2}}$.

Resonant State	Resonant Helicity Element(s)	Energy W_o (BeV)	Width Γ_o (BeV)	ℓ	j_γ	X (BeV)	$A^{-}[N^{*}]$	$B^{-}[N^{*}]$
S_{11}	A_{0+}	1.530	.100	0	1	.350	$-0.35 \pm {}^{.15}_{.10}$	
S_{31}	A_{0+}	1.660	.150	0	1	.350	$-0.50 \pm {}^{.18}_{.12}$	
S_{11}	A_{0+}	1.700	.150	0	1	.350	$-0.10 \pm {}^{.12}_{.15}$	
P_{11}	A_{1-}	1.430	.230	1	1	.350	$-0.47 \pm {}^{.15}_{.20}$	
P_{11}	A_{1-}	1.650	.160	1	1	.350	$-0.30 \pm {}^{.20}_{.15}$	
P_{31}	A_{1-}	1.850	.230	1	1	.350	$-0.10 \pm .13$	
P_{33}	A_{1+}, B_{1+}	1.233	.120	1	1	.185	$1.20 \pm .035$	$2.52 \pm .05$
D_{13}	A_{2-}, B_{2-}	1.510	.120	2	1	.350	$0.60 \pm {}^{.10}_{.08}$	$-1.18 \pm {}^{.12}_{.10}$
D_{15}	A_{2+}, B_{2+}	1.650	.140	2	2	.350	$0.07 \pm {}^{.10}_{.08}$	$0.12 \pm {}^{.15}_{.12}$
F_{15}	A_{3-}, B_{3-}	1.688	.135	3	2	.350	$-0.07 \pm {}^{.10}_{.08}$	$0.00 \pm {}^{.14}_{.09}$

TABLE 4. Resonance Parameters (continued)

Resonant State	Resonant Helicity Element(s)	Energy W_o (BeV)	Width Γ_o (BeV)	ℓ	j_γ	X (Bev)	$A^-[N^*]$	$B^-[N^*]$
F_{35}	A_{3-}, B_{3-}	1.880	.250	3	2	.350	0.07 ± .07	0.03 ± .05
F_{37}	A_{3+}, B_{3+}	1.925	.200	3	3	.350	0.14 ± .07	-0.12 ± .03

For the I = 3/2 resonances the couplings are taken from reference [15]. The errors are determined by the method explained in Section 5.2. (For I = 3/2 resonances outside of the energy range of the present analysis the errors from reference [15] are also given.)

TABLE 5. Background Terms

This table gives the final values of the background contributions to the various helicity elements at the selected reference energies. The values of these contributions at other energies are then obtained by using the interpolation formula in Appendix F. 5$_1$. Re and Im stand for real and imaginary parts. The units are $\mu b^{\frac{1}{2}} \times 10^{-3}$ and again W is the total CM energy.

k_{lab} (BeV)	0.400	0.550	0.700	0.850	1.000	1.200
W (BeV)	1.272	1.383	1.481	1.573	1.660	1.770
Re A_{0+}	625	760	1050	1045	1150	850
Im A_{0+}	195	240	230	225	045	-030
Re A_{1-}	800	1150	1515	1300	1105	1020
Im A_{1-}	050	-050	110	160	040	080
Re A_{1+}	-040	-096	-077	-080	-083	-152
Im A_{1+}	017	-010	-030	-020	-050	-020
Re B_{1+}	230	380	540	630	670	780
Im B_{1+}	-035	085	120	118	-037	030
Re A_{2-}	-050	-080	-025	025	020	-165
Im A_{2-}	000	020	003	060	010	-045
Re B_{2-}	340	420	700	900	1150	1170
Im B_{2-}	070	070	070	020	060	060
Re A_{2+}	010	040	-015	-045	010	050
Im A_{2+}	015	-035	-080	-010	025	020
Re B_{2+}	-015	-018	025	-007	-035	000
Im B_{2+}	-015	-010	-020	-015	010	-005
Re A_{3-}	-010	005	020	025	010	020
Im A_{3-}	010	060	040	025	065	020
Re B_{3-}	-020	-038	-035	000	007	000
Im B_{3-}	000	014	000	-034	012	000
Re A_{3+}	010	012	027	000	024	-005
Im A_{3+}	-010	000	020	010	008	007

TABLE 5. Background Terms (continued)

k_{lab} (BeV)	0.400	0.550	0.700	0.850	1.000	1.200
W (BeV)	1.272	1.383	1.481	1.573	1.660	1.770
Re B_{3+}	-005	003	005	-009	-030	015
Im B_{3+}	000	-010	020	020	017	000
Re A_{4-}	-005	-025	-005	027	027	035
Im A_{4-}	010	010	010	018	012	007
Re B_{4-}	-005	-008	020	010	020	018
Im B_{4-}	005	010	015	008	-003	010

TABLE 6. χ^2's of the Fits

These are the χ^2's for the fits described in this section to the data on $\gamma n \rightarrow \pi^- p$. At each energy where a fit was made the number of data points not including parameters used as data*, N_{data}, the χ^2 of the fit, χ^2, and the χ^2 attainable by allowing variation of the final parameters*, χ^2_{free}, are given. W is the total CM energy.

k_{lab} (BeV)	W (BeV)	N_{data}	χ^2 **	χ^2_{free}
0.400	1.277	25	79	73
0.450	1.313	14	25	16
0.500	1.349	21	37	26
0.550	1.383	14	28	12
0.600	1.416	43	203	140
0.650	1.449	41	87	43
0.700	1.481	32	70	66
0.750	1.513	38	90	64
0.800	1.543	31	96	50
0.850	1.573	19	4.5	2
0.900	1.603	20	8.5	5
0.950	1.632	17	29	4
1.000	1.660	18	18	17
1.050	1.688	15	22	10
1.100	1.716	17	22	3
1.150	1.743	17	28	10
1.200	1.770	15	32	7

*See Section 5.2.

**A large value of χ^2 does not necessarily mean a bad fit, especially if χ^2_{free} is large, indicating inconsistencies in the data. But even if $\chi^2 >> \chi^2_{free}$, the fit is not always bad (see Figure 23), as the χ^2 can be due largely to 1 or 2 data points.

TABLE 7. Comparison of Resonance Results to Previous Studies

This table compares the "couplings" (see Section 5.2) of the resonances to the reaction $\gamma n \to \pi^- p$ as determined in the present analysis to the results of other, similar analyses. The couplings of these same resonances to the reaction $\gamma p \to \pi^+ n$ taken from reference [15] are also given for the I = 1/2 resonances.

Resonance	Helicity Amplitude	Present Analysis	Metcalf and Walker [15]	Moorhouse, et al. [14]	π^+ Coupling
$S_{11}(1530)$	A_{0+}	$-0.35^{+.15}_{-.10}$	$-0.48^{+.27}_{-.15}$	$-0.25 \pm .08$	$-0.60 \pm .12$
$S_{31}(1660)^*$	A_{0+}	$-0.50^{+.18}_{-.12}$	$-0.50^{+.20}_{-.15}$	$-0.36 \pm .03$	
$S_{11}(1700)^*$	A_{0+}	$-0.10^{+.12}_{-.15}$	$-0.17 \pm .20$	$-0.73 \pm .17$	$-0.11 \pm .18$
$P_{11}(1470)$	A_{1-}	$-0.47^{+.15}_{-.20}$	$-0.37^{+.20}_{-.40}$	$-0.28 \pm .11$	$-0.60^{+.20}_{-.12}$
$P_{11}(1650)$	A_{1-}	$-0.30^{+.20}_{-.15}$	$-0.26^{+.30}_{-.18}$	$-0.31 \pm .12$	$-0.37 \pm .20$
$P_{31}(1850)^*$	A_{1-}	$-0.10 \pm .13$	$-0.10 \pm .13$		
$P_{33}(1233)^*$	A_{1+}	$1.20 \pm .035$	$1.20 \pm .035$	$1.22 \pm .01$	
	B_{1+}	$2.52 \pm .050$	$2.52 \pm .050$	$2.59 \pm .01$	
$D_{13}(1510)$	A_{2-}	$0.60^{+.10}_{-.08}$	$0.53^{+.07}_{-.10}$	$0.70 \pm .06$	$-0.05^{+.05}_{-.07}$
	B_{2-}	$-1.18^{+.12}_{-.10}$	$-1.08^{+.13}_{-.08}$	$-1.16 \pm .02$	$-1.51^{+.09}_{-.10}$

*Values from reference [15] used in the present analysis.

TABLE 7. Comparison of Resonance Results to Previous Studies (continued)

Resonance	Helicity Amplitude	Present Analysis	Metcalf and Walker [15]	Moorhouse, et al. [14]	π^+ Coupling
D_{15} (1650)	A_{2+}	$0.07^{+.10}_{-.08}$	$0.02 \pm .07$	$-0.08 \pm .02$	$-0.05^{+.07}_{-.06}$
	B_{2+}	$0.12^{+.15}_{-.12}$	$0.03 \pm .10$	$0.16 \pm .02$	$0.14^{+.06}_{-.08}$
F_{15} (1688)	A_{3-}	$-0.07^{+.10}_{-.08}$	$-0.05^{+.09}_{-.12}$	$-0.14 \pm .02$	$-0.05^{+.05}_{-.08}$
	B_{3-}	$0.0^{+.14}_{-.09}$	$0.0^{+.16}_{-.10}$	$-0.18 \pm .02$	$-0.56 \pm .06$
F_{35} (1880)*	A_{3-}	$0.07^{+.05}_{-.08}$	$0.07^{+.05}_{-.08}$		
	B_{3-}	$0.03 \pm .05$	$0.03 \pm .05$		
F_{37} (1925)*	A_{3+}	$0.14 \pm .07$	$0.14 \pm .07$	$0.19 \pm ?$	
	B_{3+}	$-0.12 \pm .03$	$-0.12 \pm .03$	$-0.22 \pm ?$	

*Values from reference [15] used in present analysis.

TABLE 8. Quark Model States*

Quark State	Nucleon Resonance	Quark State	Nucleon Resonance
$[56, 0^+]_0\ {}^2 8_{1/2}$	nucleon	$[56, 0^+]_0\ {}^4 10_{3/2}$	P_{33} (1236)
$[70, 1^-]_1\ {}^2 8_{1/2}$	S_{11} (1530)**	$[70, 1^-]_1\ {}^4 8_{1/2}$	S_{11} (1700)**
$[70, 1^-]_1\ {}^2 8_{3/2}$	D_{13} (1510)**	$[70, 1^-]_1\ {}^4 8_{3/2}$	D_{13} (1700)**
$[70, 1^-]_1\ {}^2 10_{1/2}$	S_{31} (1660)	$[70, 1^-]_1\ {}^4 8_{5/2}$	D_{15} (1650)
$[70, 1^-]_1\ {}^2 10_{3/2}$	D_{33} (1700)†		
$[56, 0^+]_2\ {}^2 8_{1/2}$	P_{11} (1430)**	$[70, 0^+]_2\ {}^2 8_{1/2}$	P_{11} (1650)**
$[56, 0^+]_2\ {}^4 10_{3/2}$	P_{33} (1700)**†	$[70, 0^+]_2\ {}^4 8_{3/2}$	P_{13} (?)**†
$[56, 2^+]_2\ {}^2 8_{3/2}$	P_{13} (1850)**†	$[70, 0^+]_2\ {}^2 10_{1/2}$	P_{31} (?)**
$[56, 2^+]_2\ {}^2 8_{5/2}$	F_{15} (1688)**	$[70, 2^+]_2\ {}^2 8_{3/2}$	P_{13} (?)**†
$[56, 2^+]_2\ {}^4 10_{1/2}$	P_{31} (1850)**	$[70, 2^+]_2\ {}^2 8_{5/2}$	F_{15} (?)**
$[56, 2^+]_2\ {}^4 10_{3/2}$	P_{33} (?)**†	$[70, 2^+]_2\ {}^4 8_{1/2}$	P_{11} (?)**
$[56, 2^+]_2\ {}^4 10_{5/2}$	F_{35} (1880)**	$[70, 2^+]_2\ {}^4 8_{3/2}$	P_{13} (?)**†
$[56, 2^+]_2\ {}^4 10_{7/2}$	F_{37} (1925)	$[70, 2^+]_2\ {}^4 8_{5/2}$	F_{15} (?)**
$[70, 2^+]_2\ {}^2 10_{3/2}$	P_{33} (?)**†	$[70, 2^+]_2\ {}^4 8_{7/2}$	F_{17} (?)**†
$[70, 2^+]_2\ {}^2 10_{5/2}$	F_{35} (?)**		

*The notation used for the quark states is explained in Section 5.3. The nucleon resonances listed are possible candidates for these states.

**Mixing possible within same level of excitation.

†Not used in present analysis.

TABLE 9. Comparison of Resonance Results to Quark Model Predictions

This table compares the resonance couplings of the present analysis* to the quark model calculations of Feynman, et al. [4], herein referred to as the FKR values. For each resonance the table gives the probable quark state, indicating if mixing is possible, and the values of $A^N_{1/2}$ and $A^N_{3/2}$ (see Section 5.3 and Appendix F.4 for the relationship of these quantities to the "couplings" of Table 5). The units are $GeV^{-1/2} \times 10^{-3}$. The numerical values for the FKR model have been calculated by Moorhouse, et al. [14].

Resonance	Quark State**	$A^N_{1/2}$ FKR Value	$A^N_{1/2}$ Present Analysis	$A^N_{3/2}$ FKR Value	$A^N_{3/2}$ Present Analysis
S_{11} (1530)	$[\underset{\sim}{70}, 1^-]_1\ ^2\underset{\sim}{8}_{1/2}{}^\dagger$	-108††	$-37\ ^{+22}_{-15}$		
S_{31} (1660)	$[\underset{\sim}{70}, 1^-]_1\ ^2\underset{\sim}{10}_{1/2}$	47††	105 ± 29		
S_{11} (1700)	$[\underset{\sim}{70}, 1^-]_1\ ^4\underset{\sim}{8}_{1/2}{}^\dagger$	30††	$-11\ ^{+13}_{-17}$		
P_{11} (1470)	$[\underset{\sim}{56}, 0^+]_2\ ^2\underset{\sim}{8}_{1/2}{}^\dagger$	-18††	$54\ ^{+17}_{-23}$		
P_{11} (1650)	$[\underset{\sim}{70}, 0^+]_2\ ^2\underset{\sim}{8}_{1/2}{}^\dagger$	10††	$55\ ^{+33}_{-22}$		
P_{31} (1850)	$[\underset{\sim}{56}, 2^+]_2\ ^4\underset{\sim}{10}_{1/2}{}^\dagger$	-30††	-32 ± 65		
P_{33} (1233)	$[\underset{\sim}{56}, 0^+]_0\ ^4\underset{\sim}{10}_{3/2}$	-108	-140 ± 6	-187	-254 ± 7
D_{13} (1510)	$[\underset{\sim}{70}, 1^-]_1\ ^2\underset{\sim}{8}_{3/2}{}^\dagger$	-31††	$-76\ ^{+13}_{-10}$	-109	$-129\ ^{+13}_{-11}$
D_{15} (1650)	$[70, 1^-]_1\ ^4 8_{5/2}$	-38	$14\ ^{+20}_{-16}$	-53	$-36\ ^{+45}_{-36}$

TABLE 9. Comparison of Resonance Results ... (continued)

Resonance	Quark State**	$A^N_{1/2}$ FKR Value	$A^N_{1/2}$ Present Analysis	$A^N_{3/2}$ FKR Value	$A^N_{3/2}$ Present Analysis
F_{15} (1688)	$[\underset{\sim}{56}, 2^+]_2\ {}^2\underset{\sim}{8}_{5/2}$ #	30	$11\ ^{+16}_{-13}$	0	$0\ ^{+26}_{-17}$
F_{35} (1880)	$[\underset{\sim}{56}, 2^+]_2\ {}^4\underset{\sim}{10}_{5/2}$ †	-10 ††	47 ±67	-90 ††	-28 ±47
F_{37} (1925)	$[\underset{\sim}{56}, 2^+]_2\ {}^4\underset{\sim}{10}_{7/2}$	-50	-58 ±29	-70	-97 ±24

*The I = 3/2 resonances are the same as in reference [15].

**Notation defined in Section 5.3.

† Mixing possible within same level of excitation.

†† Both recoil and non-recoil terms contribute.

If this resonance is truly the Regge recurrence of the nucleon, there should be no mixing even though there are other states with these quantum numbers.

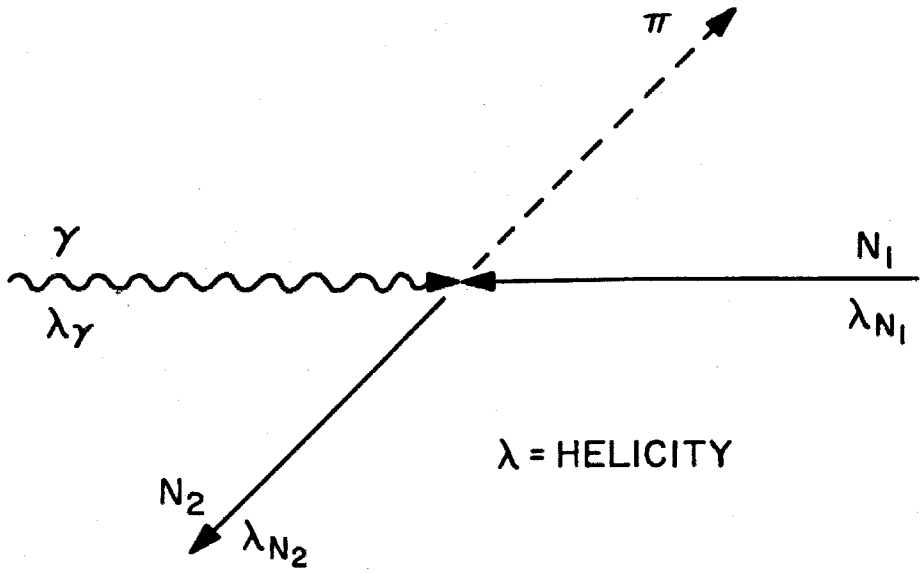

(a) Pion Photoproduction

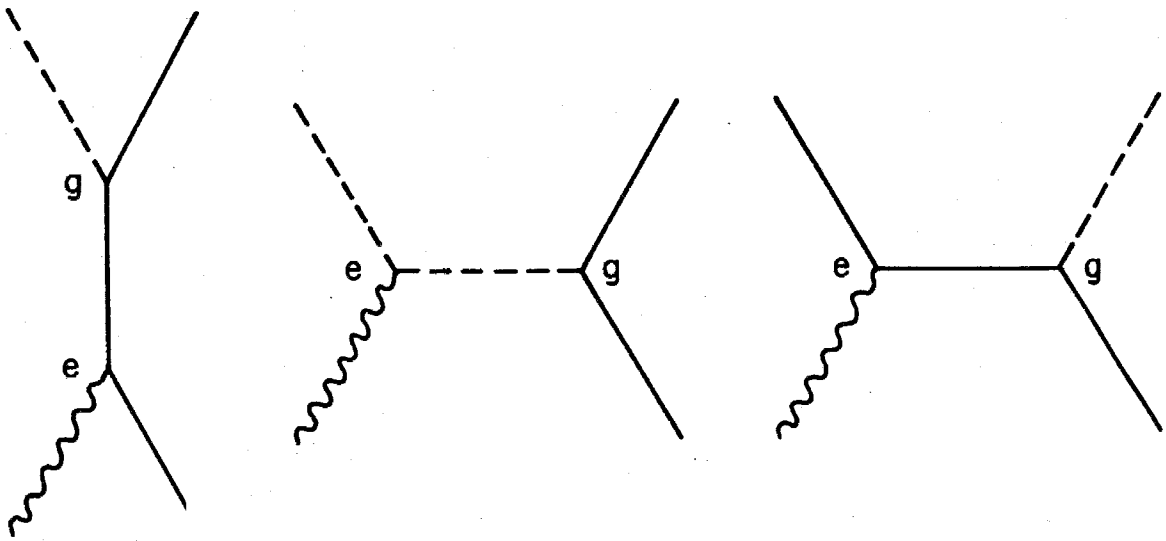

(b) The Electric Born Terms

FIGURE 19

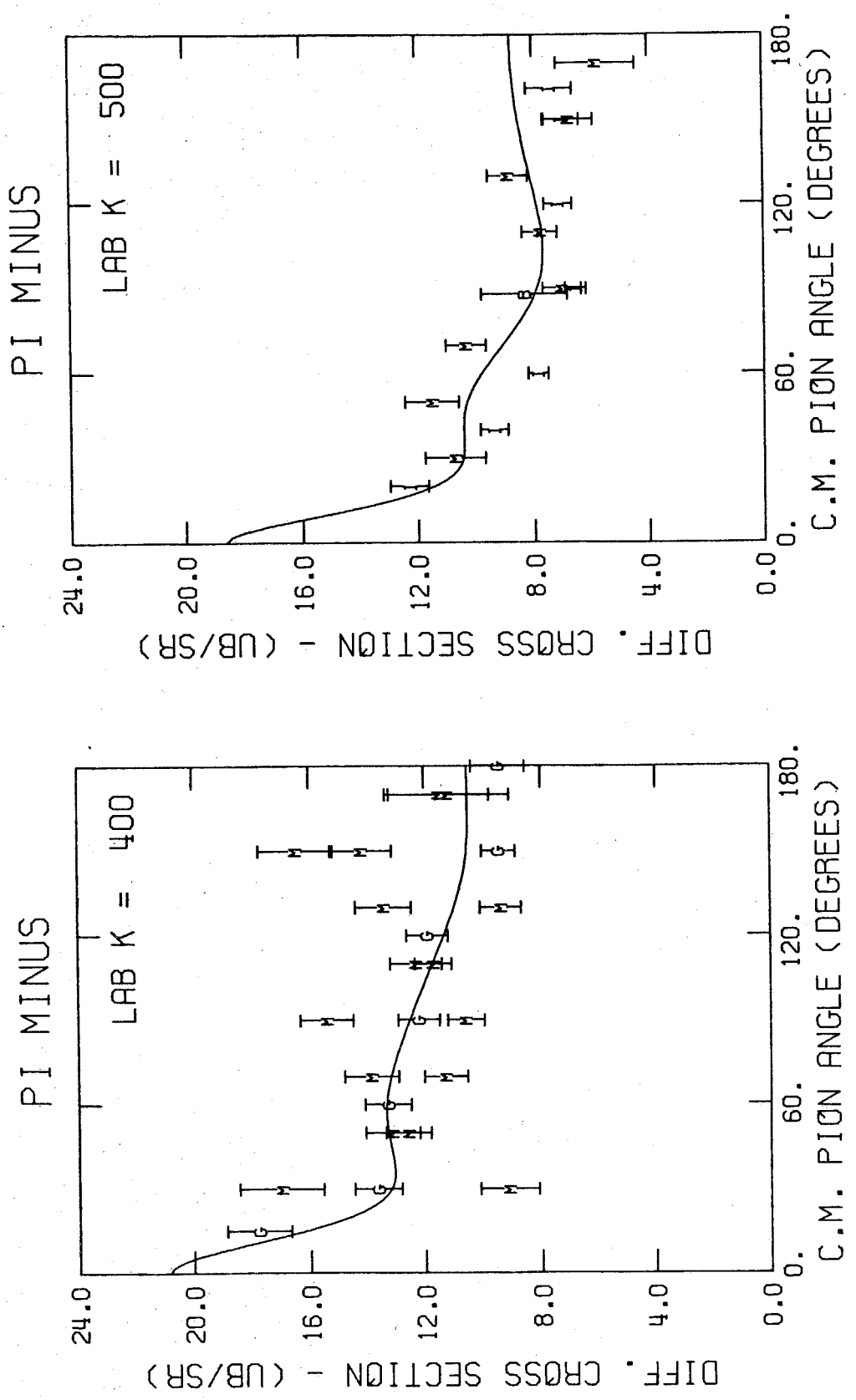
PI MINUS
LAB K = 500
DIFF. CROSS SECTION - (UB/SR)
24.0
20.0
16.0
12.0
8.0
4.0
0.0
0.
60.
120.
180.
C.M. PION ANGLE (DEGREES)
PI MINUS
LAB K = 400
DIFF. CROSS SECTION - (UB/SR)
24.0
20.0
16.0
12.0
8.0
4.0
0.0
0.
60.
120.
180.
C.M. PION ANGLE (DEGREES)

FIGURE 20

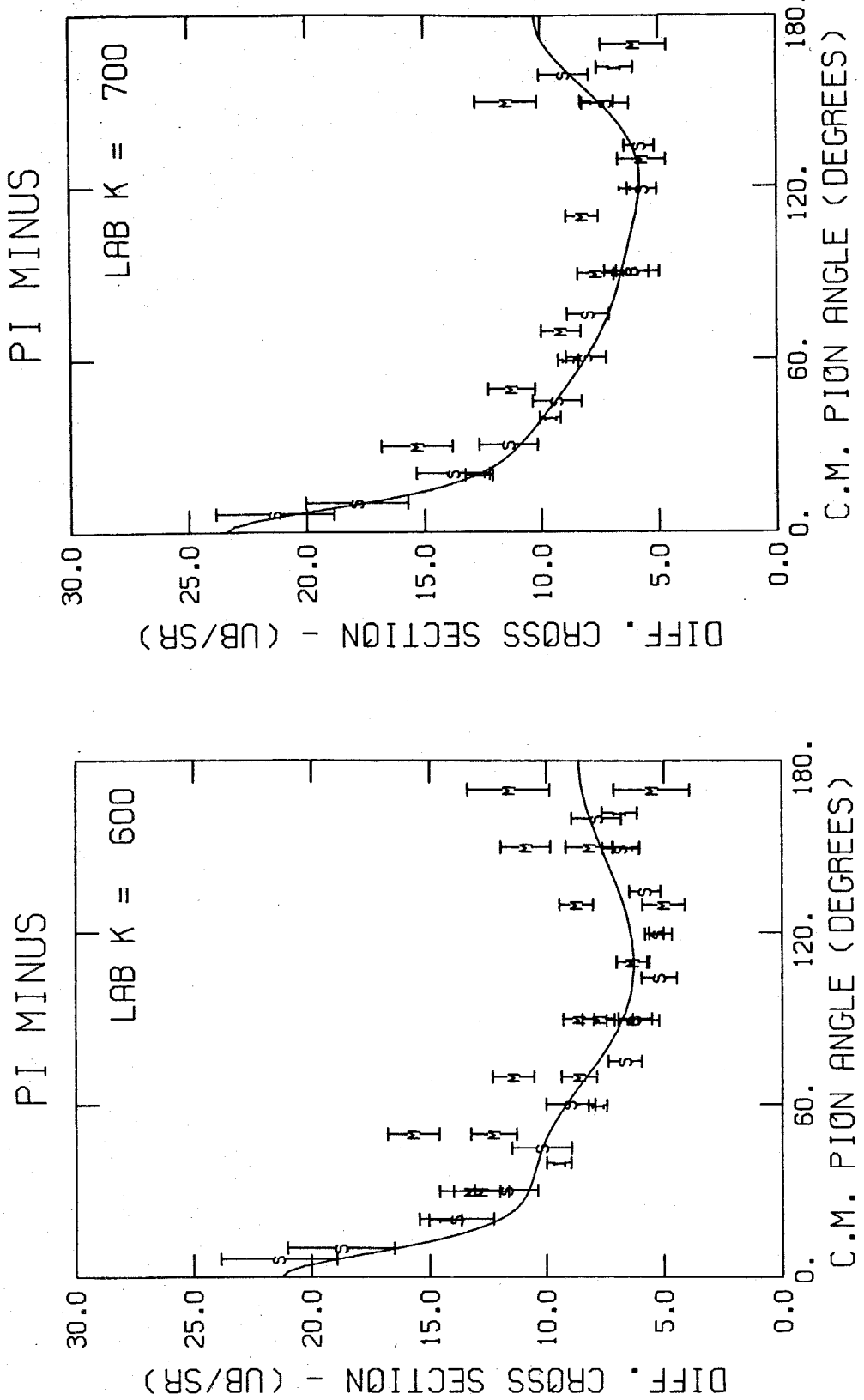
PI MINUS
LAB K = 700
DIFF. CROSS SECTION - (UB/SR)
C.M. PION ANGLE (DEGREES)
30.0
25.0
20.0
15.0
10.0
5.0
0.0
0.
60.
120.
180.
PI MINUS
LAB K = 600
DIFF. CROSS SECTION - (UB/SR)
C.M. PION ANGLE (DEGREES)

FIGURE 21

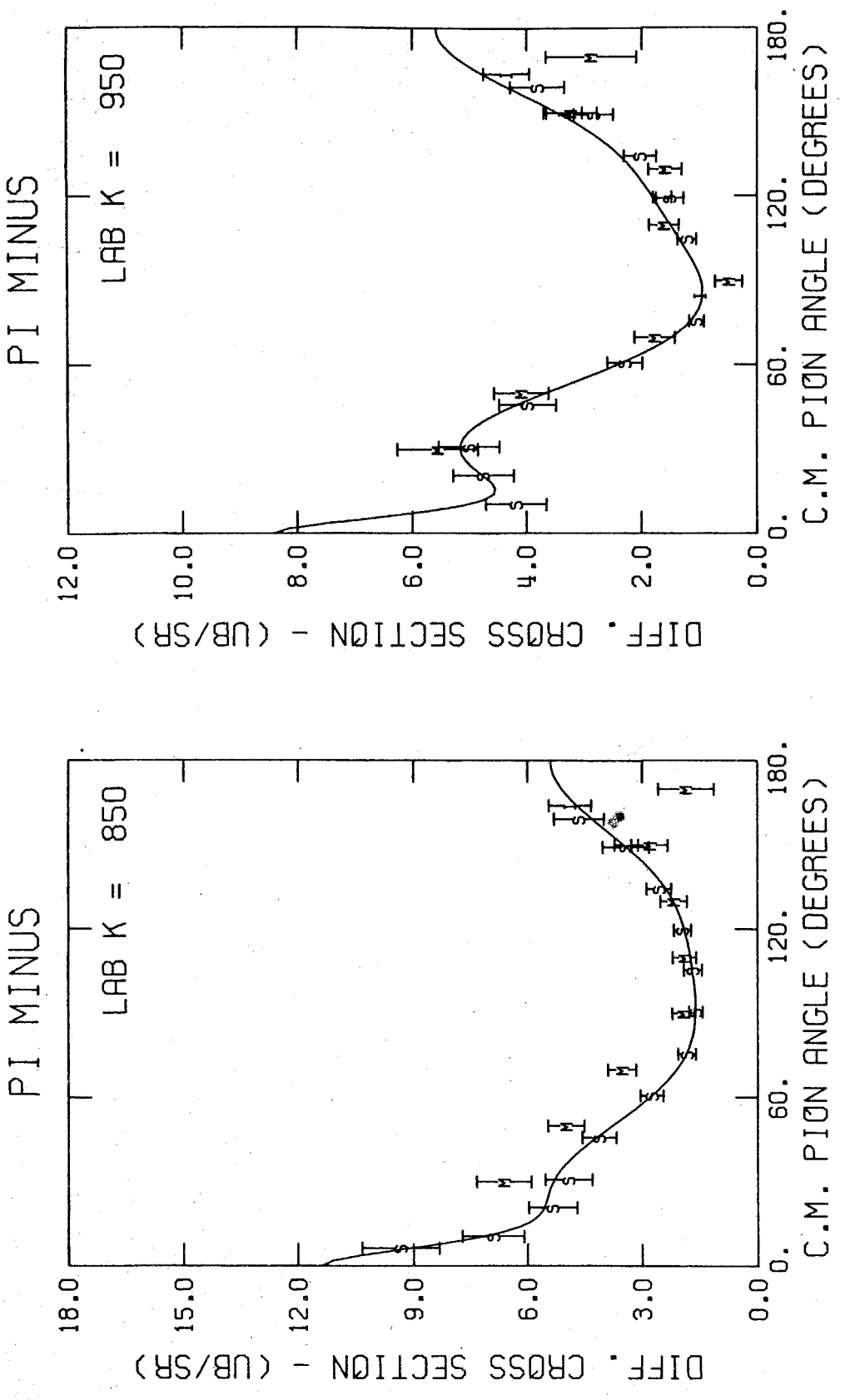
PI MINUS
LAB K = 950
DIFF. CROSS SECTION - (UB/SR)
12.0
10.0
8.0
6.0
4.0
2.0
0.0
0.
60.
120.
180.
C.M. PION ANGLE (DEGREES)
PI MINUS
LAB K = 850
DIFF. CROSS SECTION - (UB/SR)
18.0
15.0
12.0
9.0
6.0
3.0
0.0
0.
60.
120.
180.
C.M. PION ANGLE (DEGREES)

FIGURE 22

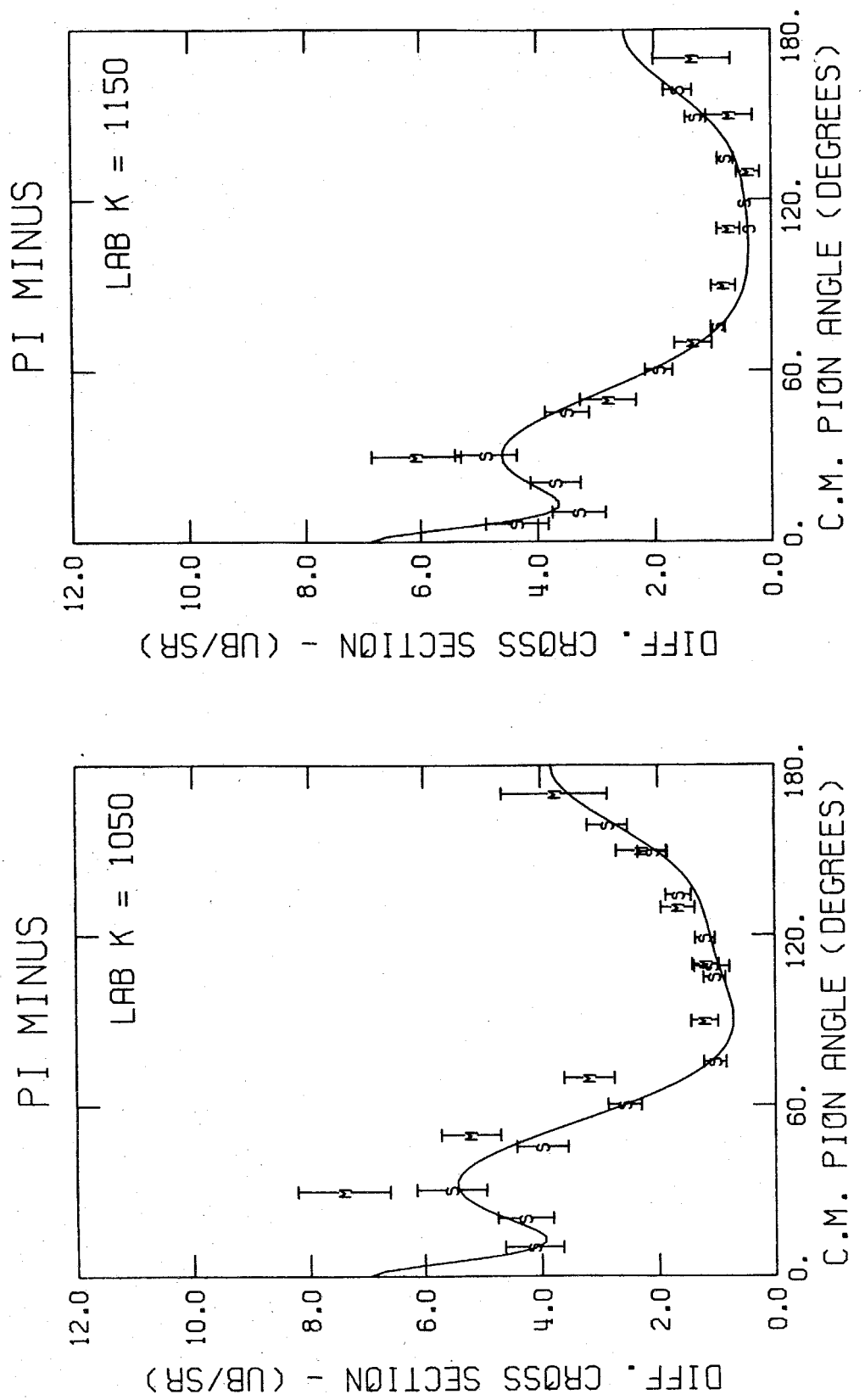
PI MINUS
LAB K = 1150
DIFF. CROSS SECTION - (UB/SR)
12.0
10.0
8.0
6.0
4.0
2.0
0.0
0.
60.
120.
180.
C.M. PION ANGLE (DEGREES)
PI MINUS
LAB K = 1050
DIFF. CROSS SECTION - (UB/SR)
12.0
10.0
8.0
6.0
4.0
2.0
0.0
0.
60.
120.
180.
C.M. PION ANGLE (DEGREES)

FIGURE 23

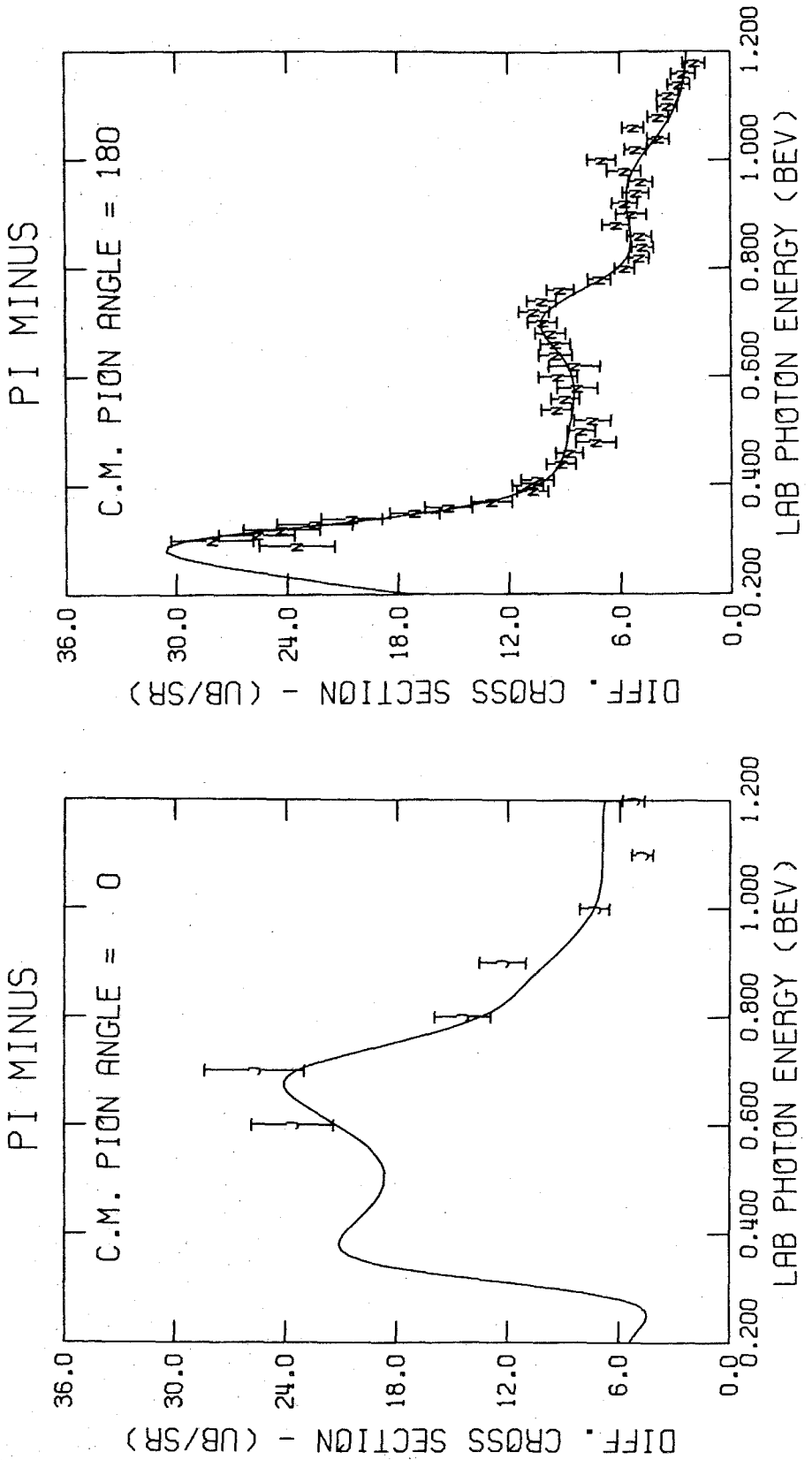
PI MINUS
C.M. PION ANGLE = 180
DIFF. CROSS SECTION - (UB/SR)
LAB PHOTON ENERGY (BEV)
PI MINUS
C.M. PION ANGLE = 0
DIFF. CROSS SECTION - (UB/SR)
LAB PHOTON ENERGY (BEV)

FIGURE 24

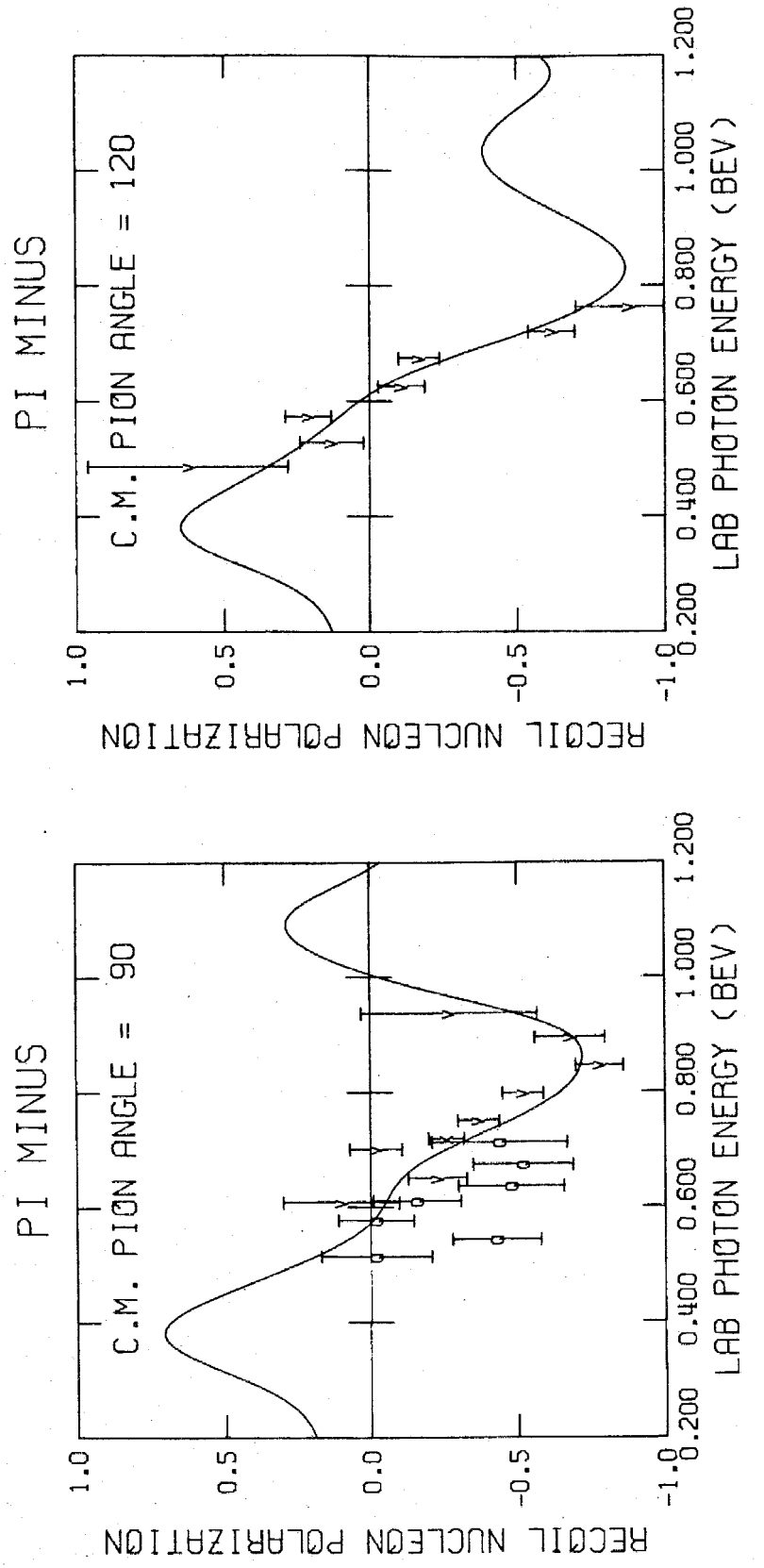
PI MINUS
C.M. PION ANGLE = 90
RECOIL NUCLEON POLARIZATION
LAB PHOTON ENERGY (BEV)
1.0
0.5
0.0
-0.5
-1.0
0.200
0.400
0.600
0.800
1.000
1.200
PI MINUS
C.M. PION ANGLE = 120
RECOIL NUCLEON POLARIZATION
LAB PHOTON ENERGY (BEV)

FIGURE 25

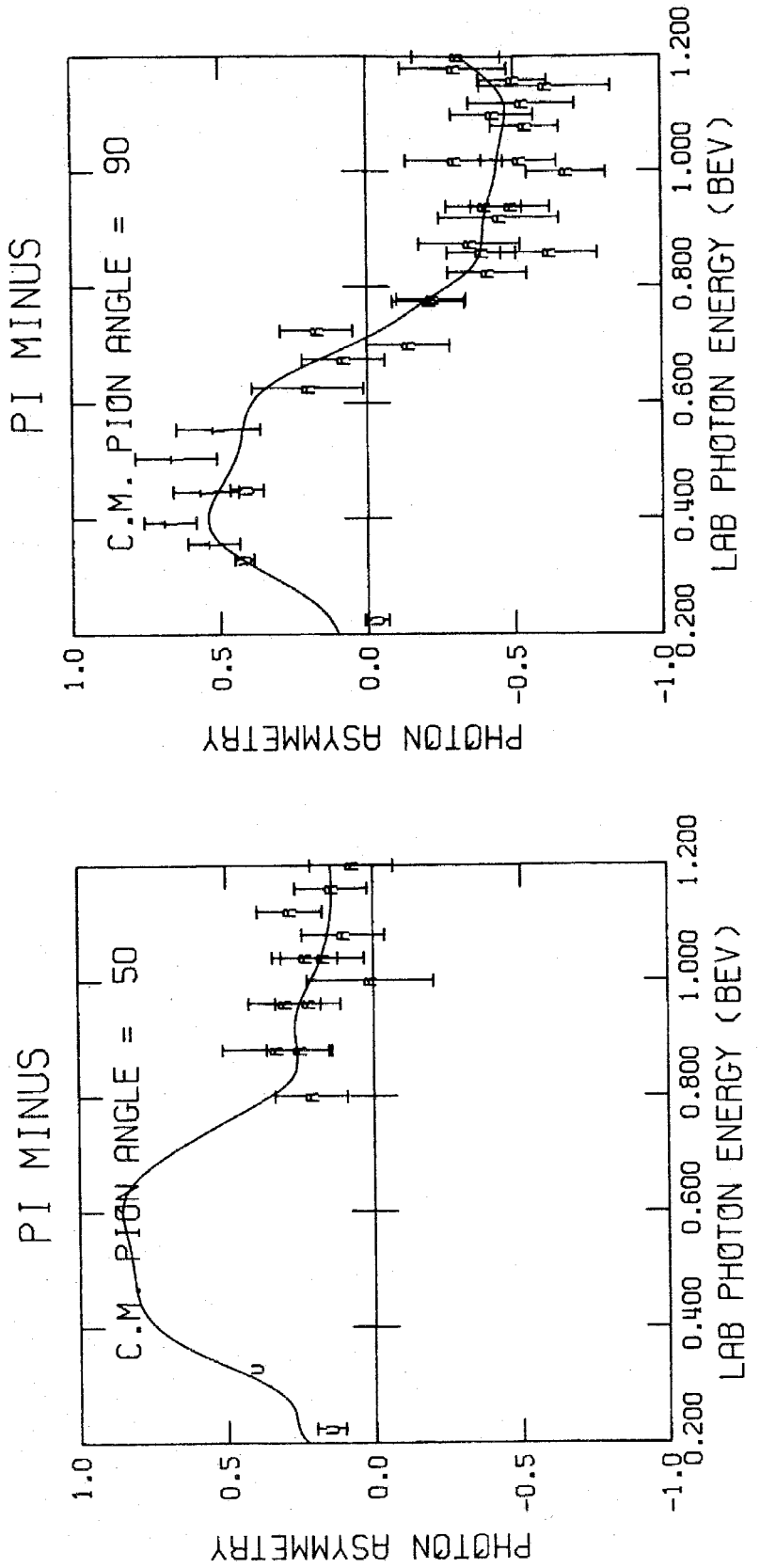
PI MINUS
C.M. PION ANGLE = 90
PHOTON ASYMMETRY
LAB PHOTON ENERGY (BEV)
1.0
0.5
0.0
-0.5
-1.0
0.200
0.400
0.600
0.800
1.000
1.200
PI MINUS
C.M. PION ANGLE = 50
PHOTON ASYMMETRY
LAB PHOTON ENERGY (BEV)

FIGURE 26

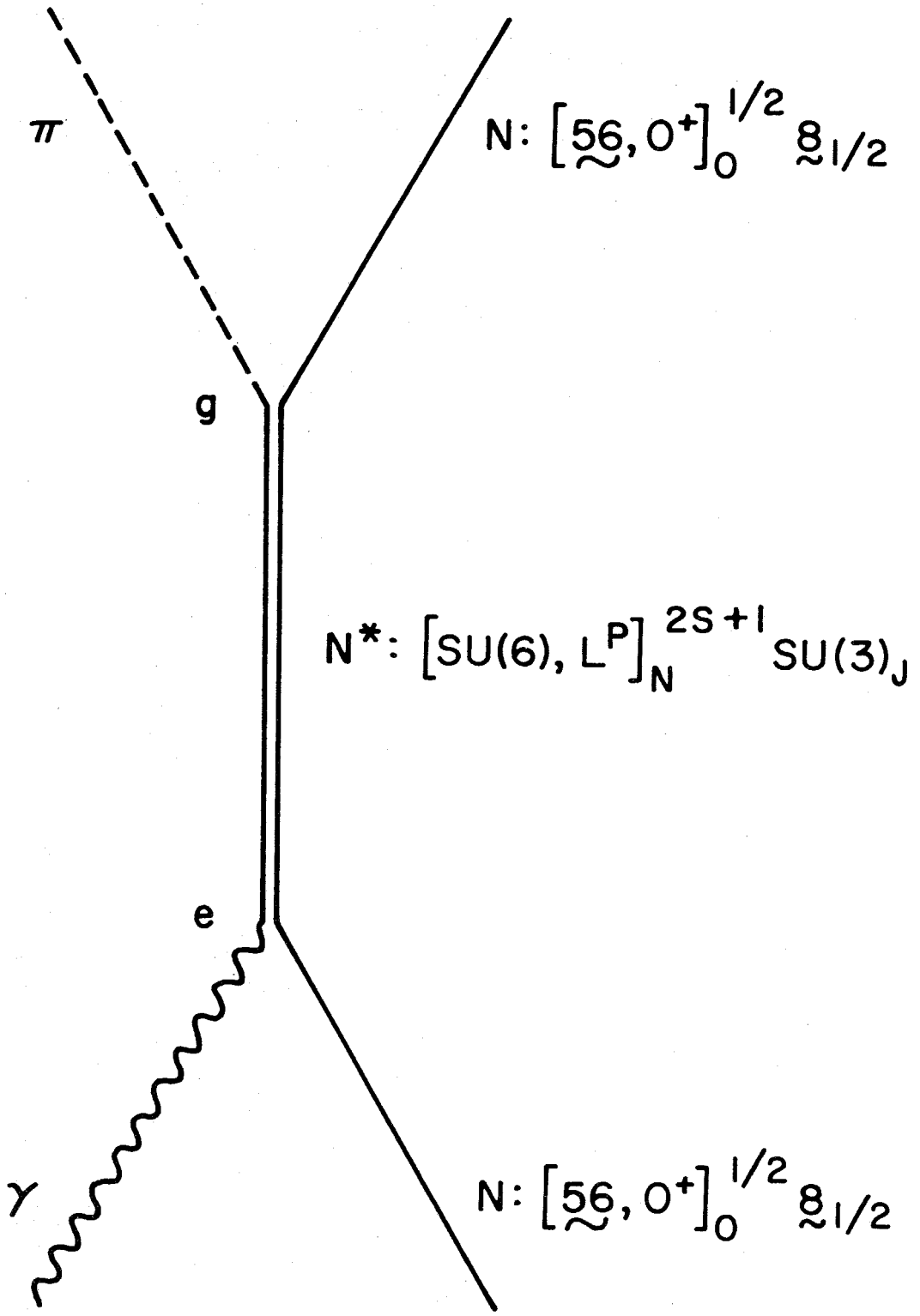

FIGURE 27

Pion Photoproduction in the Quark Model

6. DISCUSSION AND CONCLUSIONS

The purpose of the research described in this thesis has been two-fold. First it was desired to obtain a set of polarization measurements for the recoil proton in the reaction $\gamma n \rightarrow \pi^- p$ in the resonance region. Next it was hoped that these polarizations would make possible a better determination of the couplings of several nucleon isobars to the pion photoproduction reaction. Such improved determinations of these couplings would be quite useful, among other things, for comparison to quark model calculations of the electromagnetic decay widths of these isobars.

The initial goal, the determination of the recoil polarization values at CM pion angles of 90° and 120° in the region from 500 MeV to 900 MeV in lab photon energy, has been successfully attained. The analysis described in Sections 2 through 4 has yielded polarization values (Table 3) which are consistent, within the statistical and the systematic errors, with other polarization measurements for the reaction $\gamma n \rightarrow \pi^- p$. Our polarization values also agree reasonably well with the predictions of a phenomenological study of photoproduction which did not include these polarizations (see Figure 18). This indicates that our results are consistent with the other experimental data, of various types, which exist not only for the reaction $\gamma n \rightarrow \pi^- p$, but also for the related reactions $\gamma p \rightarrow \pi^+ n$ and $\gamma p \rightarrow \pi^o p$.

Using the results of this polarization experiment along with various other data on the reaction $\gamma n \rightarrow \pi^- p$ a phenomenological analysis of the reaction has been carried out (Section 5). With a

resonance-background model that had been used in several previous analyses [9, 15], the current analysis was able to extract the couplings to negative pion photoproduction of many of the I = $\frac{1}{2}$ nucleon resonances (in the energy region from 1.300 to 1.800 GeV). The results for these couplings are summarized in Table 4 and are compared to the results of similar analyses [14, 15] in Table 7. In general the present analysis agrees with the results of both these previous studies. The agreement with reference [15] is not surprising since the same model was used and the data, except for the new polarizations, were essentially the same. However, the couplings determined in the present analysis show a slightly better resolution, especially in the cases of the $P_{11}(1470)$ and the $S_{11}(1530)$ resonances. The fits to the data obtained in the present analysis were, on the whole, quite good (as indicated by Figures 20-26).

One interesting feature of the results in Table 7 is the size of the $S_{11}(1530)$ coupling compared to the helicity $\frac{1}{2}$ (i.e. A_{2-}) coupling of the $D_{13}(1510)$. At one time it was felt that the helicity $\frac{1}{2}$ coupling of the $D_{13}(1510)$ was quite small[9], as it is in $\gamma p \rightarrow \pi^+ n$, * and that therefore the structure of the 180° cross section (see Figure 24) in this region, which must be a helicity $\frac{1}{2}$ effect, was due to the $S_{11}(1530)$ which then had to be large, as it is in its π^+ coupling. This similarity in the couplings to $\gamma n \rightarrow \pi^- p$ and $\gamma p \rightarrow \pi^+ n$ indicated that these couplings were dominated by the isovector component

* The couplings of the I=$\frac{1}{2}$ nucleon resonances to the reaction $\gamma p \rightarrow \pi^+ n$ as determined in reference [15] are also included in Table 7 for comparison.

(see Equation 1.1). The more recent analyses (including the present one) shown in Table 7 all indicate a dramatic change from this point of view. All of these analyses, while being consistent with an isovector domination of the helicity 3/2 (i.e. B_{2-}) coupling of the $D_{13}(1510)$, indicate a large isoscalar contribution to the $S_{11}(1530)$ coupling as well as to the helicity 1/2, $D_{13}(1510)$ coupling.

This increase in the isoscalar contribution of the $S_{11}(1530)$, although it is certainly not dominant, is perhaps encouraging in view of the fact that a recent experiment [16] on the coherent photoproduction of η's from deuterium indicates a large isoscalar amplitude for this resonance, which dominates $\gamma N \rightarrow \eta N$ at threshold. On the other side of the coin, however, is the research of Heusch, et al. [40] on the reaction $\gamma N \rightarrow \eta N$ which agrees with a very small isoscalar amplitude for this resonance.

Among the other I = 1/2 resonances the isovector amplitude seems to dominate the $S_{11}(1700)$, $P_{11}(1650)$, the helicity 1/2 coupling of the $F_{15}(1688)$, and the helicity 3/2 coupling of the $D_{15}(1650)$, at least on the basis of the results of the present analysis, along with the π^+ couplings of reference [15]. The $P_{11}(1470)$ also shows a larger isovector contribution than in the other analyses in Table 7, which is interesting since this resonance is felt to be rather better determined, because of the new polarization data, than in the previous analyses. The extent to which these various behaviors agree with quark model predictions will now be examined.

The electromagnetic decay amplitudes of many of the nucleon resonances as predicted by the quark model of Feynman, Kislinger,

and Ravndal (which will be referred to as the FKR model) are given in Table 9 accompanied by the results of the present analysis.* In comparing these two sets of values it must be kept in mind that whereas the numerical value depends on details of the wavefunctions, etc. used in the model, the signs in both cases are fixed. The arbitrary sign of the intermediate state in the quark model calculations appears at both vertices and cancels out so that the overall sign in both cases is fixed relative to the Born (pole) terms. In many cases, however, the quark model value depends on the difference between the recoil and the non-recoil contributions and therefore depends on the details of the dynamics used. Furthermore, the quark state used for each resonance is often only one possible choice and in such cases mixing of an undetermined amount may occur. Therefore, in making specific conclusions about the FKR model it is important to first look at places where (1) no mixing occurs and (2) there is no interference between the recoil and non-recoil terms. In Table 9 these are the cases which do not have a dagger (†) after the quark state nor a (††) after the FKR value.

The first of these "definitive" comparisons is the $P_{33}(1233)$ which appears in the same SU(6) multiplet as the nucleon. In this case the FKR values are seen to agree with the present analysis in sign and to at least a reasonable degree in magnitude. The larger numerical values found in the phenomenological analysis agree with

---

* The couplings of Table 4 are converted into the decay amplitudes of Table 9 by dividing out the part due to pion vertex (see Appendix F. 4).

similar analyses [14, 15] and indicate that the details (i.e., the form of the wavefunctions, etc.) of the FKR model are not perfect, which is hardly surprising.

The $D_{15}(1650)$ is also free of possible mixing and interference effects and the agreement for the helicity 3/2 coupling is quite good. The helicity 1/2 coupling of this resonance, on the other hand, is a definite disagreement and it is hard to see how the uncertainty in the fitted value could be stretched to include the FKR value. There are, however, many nucleon resonances in this region (several not even included in the present analysis) and a change in this coupling is possible in a more refined analysis. Otherwise, a modification of the present quark model is indicated.

The $F_{15}(1688)$ is also a "definitive" case, assuming that it is the Regge recurrence of the nucleon, and its agreement is quite good. This is especially significant for the helicity 3/2 amplitude. The vanishing of this amplitude was predicted quite early in quark model studies [2] and the continued evidence of a zero value even with new data included is strong support for this model.

The final case without any mixing or interference is the $F_{37}(1925)$. As in the case of the $P_{33}(1233)$, the couplings of this resonance were determined by the analysis in reference [15], but its tail does affect the region of our analysis and the present results showed no desire to vary the values used. The agreement of these values with the FKR model for the $F_{37}(1925)$ is quite impressive. Thus in summary for these definitive tests 7 out of 8 signs agree with the FKR quark model and the magnitudes in 5 of these 7 cases

agree (or very nearly agree) within the quoted errors.

For the other resonances in Table 9 the agreement is not as impressive; however, in all these cases mixing is possible within the same level of excitation and in all but one of these cases the recoil and non-recoil terms have the opposite sign making the final sign dependent on the dynamical details of these two terms. Despite these ambiguities the signs agree for 7 of the remaining 10 couplings. This would indicate that (1) in general, mixing is not an important effect and (2) the FKR model describes the actual dynamics far better than one has a right to expect from such a naive model. This latter fact is supported by the numerical agreements among many of the "definitive" resonances.

In the case of the $D_{13}(1510)$ the close agreement in the helicity 3/2 amplitude indicates that there is little or no mixing for this resonance. This is supported by the fact that the signs agree for the helicity 1/2 amplitude. The numerical discrepancy in this amplitude could be easily accounted for by the uncertainties in the dynamical details. The $S_{11}(1510)$ also agrees in sign but in this case it is not obvious which effect might account for the numerical discrepancy. One disturbing feature of the $S_{11}(1530)$ and the helicity 1/2, $D_{13}(1510)$ couplings is that the FKR values tend to support the isovector dominance of these amplitudes in disagreement with the more recent phenomenological results indicated in Table 7 [4, 15].

Perhaps the largest disagreement in Table 9 is the $P_{11}(1470)$. All recent analyses (see Table 7) give a sign for this amplitude that disagrees with the FKR value as well as with the results of non-relativistic quark models [2, 3].* There are in this case, however, several good candidates for mixing and in view of the resolution in the present analysis it would seem that the time has come to investigate this possibility rather than citing the "elusive" nature of this resonance [9, 14] in photoproduction.

In summary the agreement in signs (14 out of 18) and on magnitudes (in the case of the 'definitive" resonances) shown in Table 9 is most impressive. The conclusion (especially when its many other successful predictions [3, 4, 14] are considered) is clearly that the quark model, despite a simplicity that frequently prevents it from being taken very seriously, presents a picture that is in many aspects very close to what the experimental data tell us about pion photoproduction in the resonance region. This model certainly deserves much closer study, at least until some better model is able to explain as much as this model does about the nature of the couplings of the nucleon resonances to photoproduction.

---

* It should be noted that non-relativistic quark models give results quite similar to the FKR model, especially in cases where the recoil term is not important.

APPENDIX A. EXPERIMENTAL APPARATUS

A.1 Beam and Target

The Bremstrahlung beam used in this experiment was produced by accelerating electrons in the main ring of the synchrotron up to an energy equal to the desired endpoint of the Bremstrahlung spectrum and then allowing them to strike a thin tantalum target. The resulting beam was collimated by a rectangular aperture in a lead wall after which it was passed through a set of scraping walls and a sweeping magnet to remove any charged particles. Next it passed through a target maintained by the UCLA experimental group after which it was again scraped and swept to remove debris from this target before directing it on our liquid deuterium target. The number of e^+e^- pairs at the target was decreased by covering much of the length between the last sweeping magnet and the target with a He bag. A diagram of the beam path is shown in Figure 1. The beam was 1.5" wide and approximately 1.8" high at the target. This beam had been used in many previous experiments and has been more fully described in other theses [41, 42].

The beam energy was monitored by integration of the charge it produced in various thin ionization chambers during a given run. These secondary monitors were periodically calibrated using a Wilson quantameter whose ionization properties were quite well measured. This description of beam monitoring has been very brief since it was used in the present experiment only to keep track of event rates in order to check for any problems with the counters or the electronic circuits. A more detailed discussion of beam monitoring

may be found in the thesis of Paul Scheffler [22]. The duty cycle on the synchrotron was some 15%, which made accidentals in the main trigger a negligible problem for the available beam intensities.

Our target was a three inch diameter vertical cylinder of .005" mylar. It was filled with liquid deuterium at a density of about .17 gm/cm^3. The liquid deuterium was contained in a sealed system surrounded by a liquid hydrogen bath to maintain its temperature and pressure.

A particle from the center of the target had to pass through 3.8 cm of liquid deuterium as well as .16 cm of aluminum, .005 cm copper, and .013 cm of mylar to get out of the target. The pions and recoil protons from the reaction being studied in this experiment had plenty of energy to do so with very little slowing down or loss from nuclear absorption (i.e., large angle scattering from the target material causing the particles to be lost from the detection system).

A.2 LEM Spectrometer

The spectrometer used in the present experiment was the 600 MeV/c low energy magnet (LEM) which had been used in many previous experiments. Its calibration and the properties of its counter system are well described in other theses (especially those of Thiessen [41] and Walden [21]) and the present discussion will be limited to a brief survey of its important properties as they affect this experiment.

The spectrometer system is shown diagramatically in Figure 28. The fan counters along the faces of the magnet were used to veto

events in which a particle scattered off of the pole tips of the magnet. The aperture of the system was defined by counter A which had a horizontal acceptance, $\Delta\theta$, of .0289 radians at the center of the target and a vertical acceptance, $\Delta\beta$, of .112 radians at the center of the target. Counters S1 and S2 were used for trajectory definition and particle identification. Counter P was a four channel (T, TC, BC, B) momentum hodoscope. Originally the LEM had a seven channel hodoscope but this resolution was felt to be too fine for an experiment using a deuterium target (due to the kinematical smearing caused by the Fermi motion in the deuterium nucleus). Therefore, P was rebuilt to be a four channel hodoscope with approximately the same total momentum range. This meant that $\Delta Q (Q \equiv \frac{P-P_o}{P_o}$ where P_o is the central momentum setting of the spectrometer) was now about 2.5% for each channel. The recalibration of the spectrometer's acceptances using the original field map data is discussed in Pat Walden's thesis [21]. The acceptance data for the LEM system are summarized in Table 10.

A particle was defined in the spectrometer system by a coincidence between counters A, S1, S2, and P with the fan counters in veto. Protons passing the time of flight criteria were then separated by their pulse heights in counters S1 and S2. The energy of any protons detected by the LEM in this experiment was below that required for minimum ionization and their large pulse heights distinguished them from minimum ionizing particles-pions, muons, and electrons entering the system. This separation was not perfect, as

shown by the proton efficiency curve in Figure 29.* The sharp rise in proton efficiency for high momentum settings does not present a problem, however, since the spectrometer was used to detect only negative particles in coincidence with the recoil proton. The minimum ionizing particle efficiency as shown by the pion curve in Figure 29 was quite good. Unfortunately the spectrometer had no mechanism for distinguishing among pion, muons, and electrons. The problems caused by this lack of particle identification are discussed in Appendix B and were not serious in this experiment.

A. 3 Proton Counter and Range-Scattering Chamber

The proton side of the apparatus consisted of a scintillation counter and a range-scattering chamber in which the p-C scatters occurred and in which protons were brought to rest. This part of the apparatus is illustrated in Figure 30.

The proton counter was an 8" wide x 10" high x .33" thick piece of scintillator. The signal from this counter was used in coincidence with the pion signal from the spectrometer side of the apparatus to trigger the spark chambers.

This counter distinguished protons from minimum ionizing particles by means of pulse height discrimination. The protons from the reaction being studied in this experiment had energies ranging from 90 to 330 MeV, and the pulse heights due to these heavily ionizing protons were much greater than those of minimum ionizing particles (mainly pions and electrons) passing through this counter. By taking pulse height spectra of this counter gating on the pion

* Figure 29 is based on measurements by Walden and Scheffler [21,22]

signal from the spectrometer the proton peak could be clearly identified and the amount of attenuation necessary to eliminate the minimum ionizing background determined. Such pulse height spectra were taken periodically during the running to maintain the proper level of attenuation for eliminating minimum ionizing particles without cutting into the proton peak. These checks were especially necessary because this counter was acting up through much of the running due to a faulty capacitor (it was discovered late in the run!).

It was felt that the π-proton coincidence obtained between the spectrometer and the proton counter was sufficiently clean that no other counters were necessary on the proton side, especially since the subsequent trajectory in the range chamber clearly tagged most accidentals. The size of the proton counter was chosen to limit the initial proton angles such that as small a fraction as possible of the events left the sides of the range chamber, while still maintaining a reasonable event rate.

The range-scattering chamber was the same one used in several previous experiments [23, 43] and, as with the spectrometer, only a brief discussion of its features will be given. This chamber consisted of intermixed carbon modules and sparking modules of the type shown in Figure 31. The sparking modules were independent of each other and consisted of three thin aluminum foils with .29" separations mounted on lucite frames. The outer foils were grounded and the high voltage was applied to the center foil. This meant that each module had two spark gaps, greatly reducing the inefficiency due to failure of a gap to spark.

The twenty-four carbon modules were constructed to have the same area (17.5" x 17.5") as the spark modules. They consisted of graphite covered by a thin aluminum foil to act as a ground and as a protection for the neighboring spark gap. The carbon plates had thicknesses of 1 cm and 1.5 cm and the chamber was constructed such that these plates and the spark modules could be shuffled like a deck of cards in order to achieve the best resolution in proton energy both before and after the p-C scatter. However, after such a configuration change several days were required to get the gas flowing smoothly in the chamber again and all the shielding, etc., back in place. Therefore, due to time limitation it was decided to maintain the same chamber configuration during the entire run. This configuration was designed for proton energies in the 90-230 MeV range and for kinematical settings with higher proton energies (the maximum was around 320 MeV) we simply placed enough carbon in front of the chamber to make reasonably sure that the proton stopped in the chamber.* At the time this was considered a reasonable decision; even though multiple scattering and vertex uncertainty due to this carbon lowered the resolution in proton energy and angles. Far more annoying, however, was the large increase caused in the number of events that scattered before they entered the range chamber. The only way in which these events could be reconstructed was to assume that they came from the center of the target and scattered in the center of the carbon in front of the chamber. As the amount of

* The amount of carbon necessary at each setting is indicated in Table I. Recall that in this experiment a knowledge of the proton's range, thus energy, is essential to the reconstruction of the kinematics.

carbon increased this assumption became more extreme and the resolution in proton energy and angles correspondingly degraded. A set of thin hodoscope chambers mounted in front of this extra carbon would have greatly helped these resolution problems, but such chambers were unavailable at the time we were running.

The number of tracks per exposure is determined by the delay between a particle's passage through the chamber and the appearance of a track (some 500 nsec) coupled with the counting rate in the proton counter. In the present experiment well over 90% of the pictures had only one track, excluding stray electrons which were clearly distinguishable. In order to get the maximum detection efficiency with the minimum number of background tracks, the voltage of the ion sweeping field was set at the value (50 V) where the chamber efficiency just begins to fall below 100% for the given trigger delay of some 500 nsec [43]. In order to further reduce the "memory" of the chamber, ethanol was added to the argon-helium gas mixture as a quenching agent.

Two large field lenses with focal lengths of 19' were used to allow the camera to see into the entire chamber. The distortion due to the lens and mirror system has been determined by a comparison of the fiducial system as measured in photographs to its known position [43]. This distortion is found to be very small compared to normal measuring errors and no special correction is made for it. The lenses and mirrors were carefully aligned to be sure that the camera was looking directly into the chamber in both views.

Reference fiducials for the range chamber consisted of crosses accurately machined on lucite strips. These strips were attached to a rigid aluminum frame which straddled the range chamber but was independent of it so that the whole spark chamber housing did not have to be resurveyed if this chamber was removed for any reason.

If the observed p-C scatters are to be accurately measured the absolute position of the apparatus in the laboratory must be accurately determined. This surveying was done in the following manner: (1) The desired proton lab angle was located using the previously surveyed photon beam line and a precision protractor mounted at the origin. The spark chamber housing was then centered along this proton line using a transit and a precision straight edge (see Figure 32). The position of the fiducials with respect to this line were then carefully measured; (2) the distance of the fiducials from the origin and their position with respect to the previously surveyed photon beam height were then carefully measured; (3) the spectrometer was already mounted on a track pivoting about the origin such that the pion lab angle could be quite accurately set.

The range chamber configuration as well as the fiducial and lens systems are illustrated in Figures 30 and 32.

A.4 Electronics

The electronics for this experiment are illustrated in Figures 33 and 34.

The LEM electronics were the same used by Walden and Scheffler[21,22]except that their accidental monitoring circuits

were not used and are not included in Figure 33. The basic trigger in the LEM system, called S, was a fast (10 nsec) coincidence $S=A\cdot S1\cdot S2\cdot P$, where P refers to the mixed output of the four momentum channels. A particle was then defined by the slightly slower coincidence $S\cdot\overline{FAN}$. This particle signal was split into proton (p) and pion (π) signals by the pulse heights in counters S1 and S2 (no attempt being made to split the π signal into pions, muons, or electrons). The π signal was put in slow coincidence (50 nsec) with the output of each momentum channel ($\pi\cdot T$, $\pi\cdot TC$, $\pi\cdot BC$, $\pi\cdot B$) to determine which channel the particle went through.

The results of these various concidences were counted on scalers and then recorded at the end of each roll of film in order to monitor the LEM for failures of counters or circuits so that such failures could be (hopefully!) quickly corrected.

In order to get the trigger for the spark chambers the LEM signals S and π were put in coincidence with the output of the proton counter, PR, after this latter signal had been pulse height discriminated to eliminate minimum ionizing particles. This reasonably fast coincidence (approximately 20 nsec) $\pi\cdot S\cdot PR$ was then used in the following ways: (1) It was put in coincidence with the momentum channel signals (T, TC, BC, B) to determine the momentum channel of the pion; and (2) It was used to trigger the spark chamber. This "triggering" of the spark chamber consisted of firing the spark gaps; flashing the fiducials; displaying a coded light to show which momentum channel the pion is counted in; photographing both views of the track, the event number and this coded light; and, finally, advancing

the picture frame and event counter. All this took some 300 msec limiting the picture taking to 1 frame per synchrotron pulse. The master coincidence $\pi \cdot S \cdot PR$ was therefore gated to prevent a second trigger during a given pulse. The signals $\pi \cdot S \cdot PR \cdot T$, etc., were also counted on scalers in order to monitor the proton side of the experiment for any troubles.

The counters used in the LEM system have been well described in other theses [21, 41]. The proton counter was, as mentioned above, simply a wrapped 8" X 10" X 1/3" piece of scintillator attached to a phototube by means of a lucite light pipe.

TABLE 10

LEM Acceptance Properties

9.5 x 2.75 inch aperture counter

1.25 inch momentum counters

Momentum Channel	Mean Q	$\Delta\beta$ radians	ΔQ	$\Delta\beta\Delta Q$ radians	$\Delta\theta$ radians	$\Delta\Omega$ steradians	$\Delta Q\Delta\Omega$ steradians
T	0.0384	0.1120	0.0262	0.00294	0.0289	3.24×10^{-3}	8.49×10^{-5}
TC	0.0112	0.1120	0.0250	0.00280	0.0289	3.24×10^{-3}	8.10×10^{-5}
BC	-0.0147	0.1120	0.0239	0.00268	0.0289	3.24×10^{-3}	7.74×10^{-5}
B	-0.0394	0.1120	0.0229	0.00257	0.0289	3.24×10^{-3}	7.43×10^{-5}

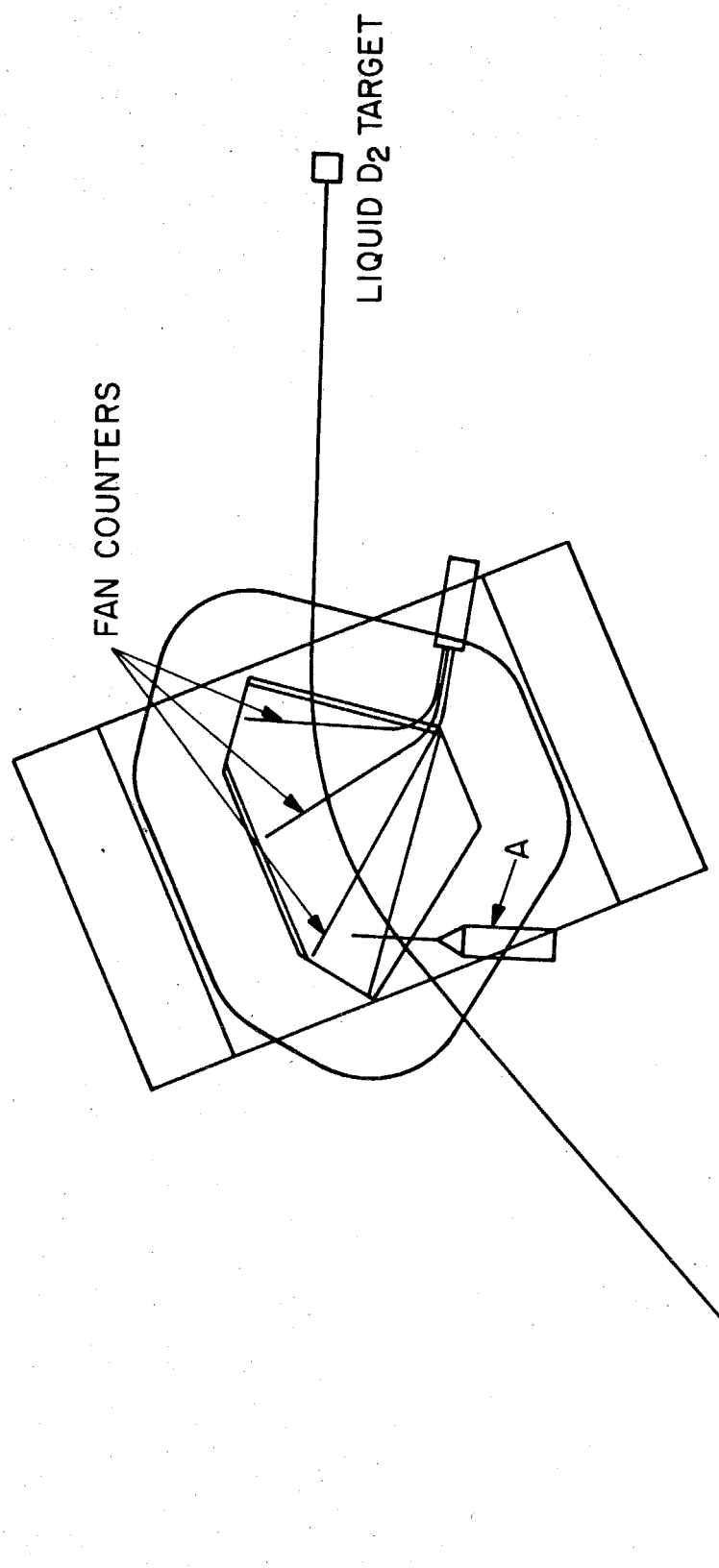

FIGURE 28

The LEM Spectrometer

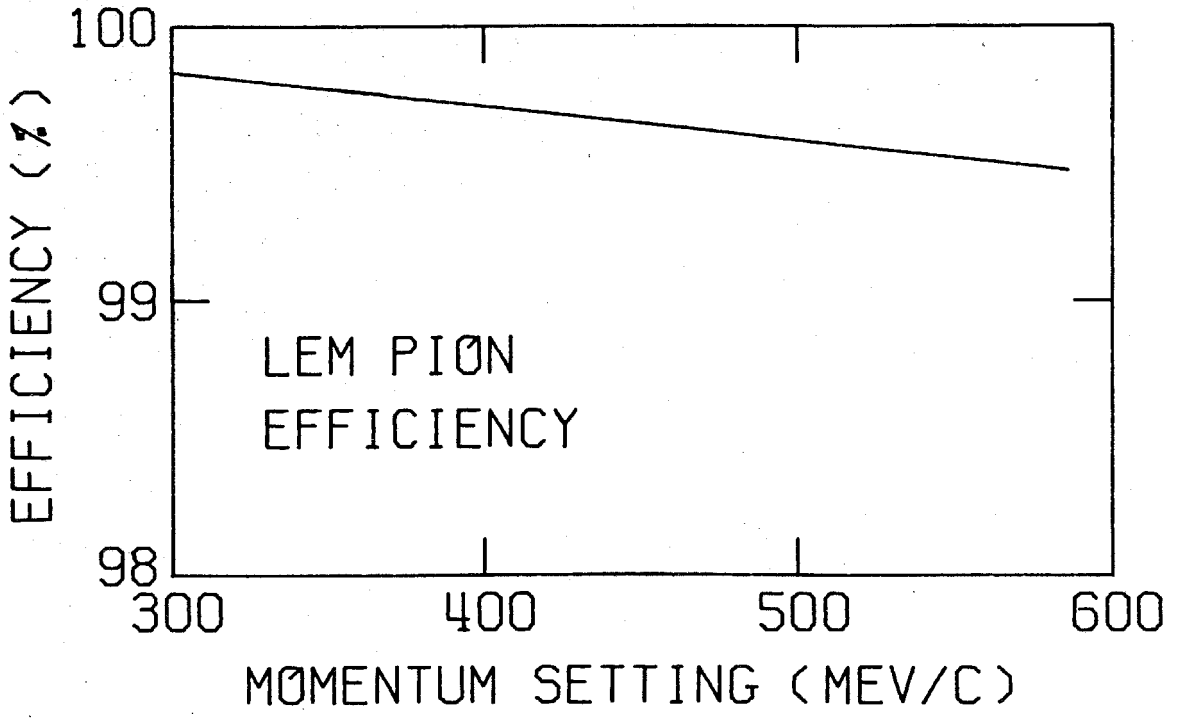
100
99
98
EFFICIENCY (%)
LEM PION
EFFICIENCY
300
400
500
600
MOMENTUM SETTING (MEV/C)

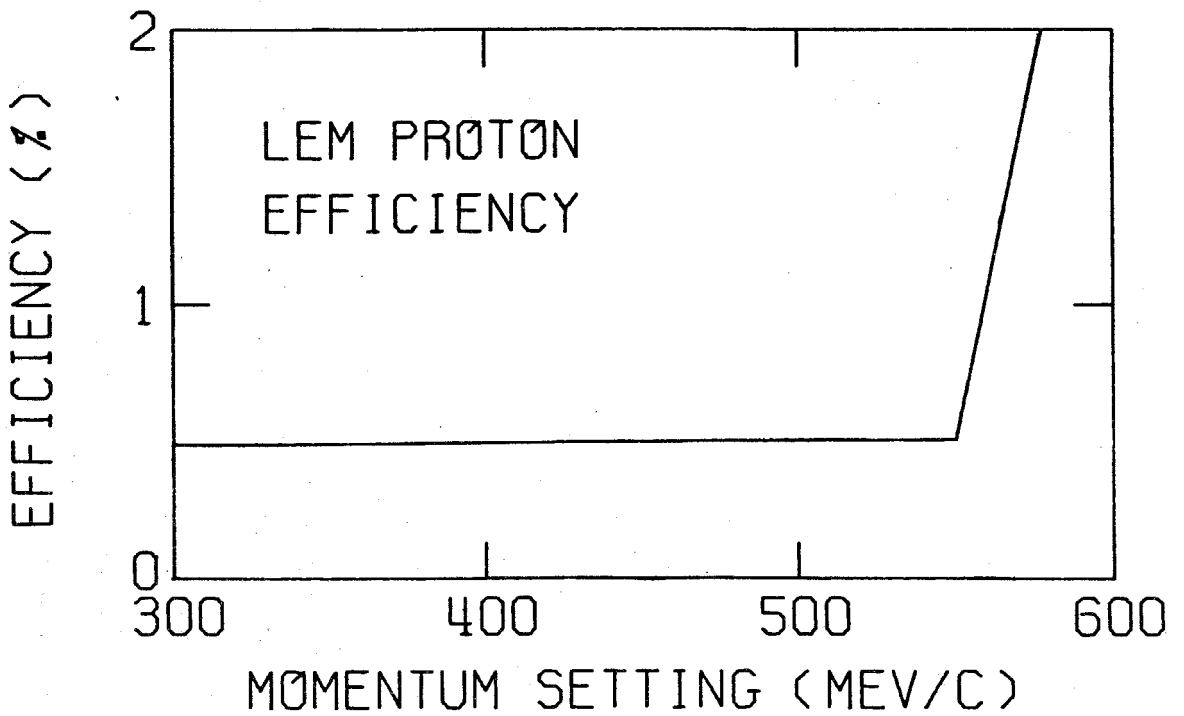
2
1
0
EFFICIENCY (%)
LEM PROTON
EFFICIENCY
300
400
500
600
MOMENTUM SETTING (MEV/C)

FIGURE 29

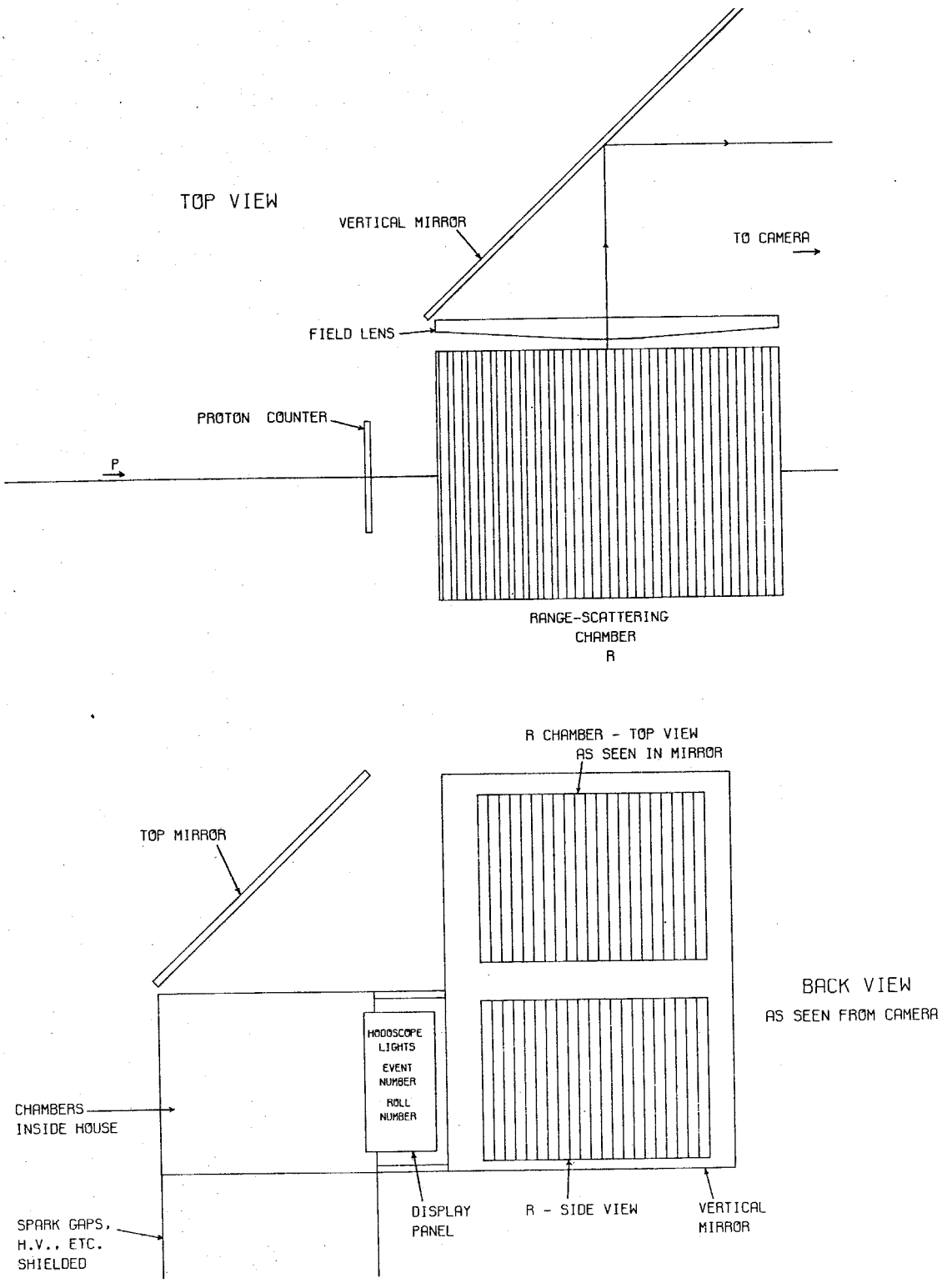

FIGURE 30 Range-Scattering Chamber Configuration

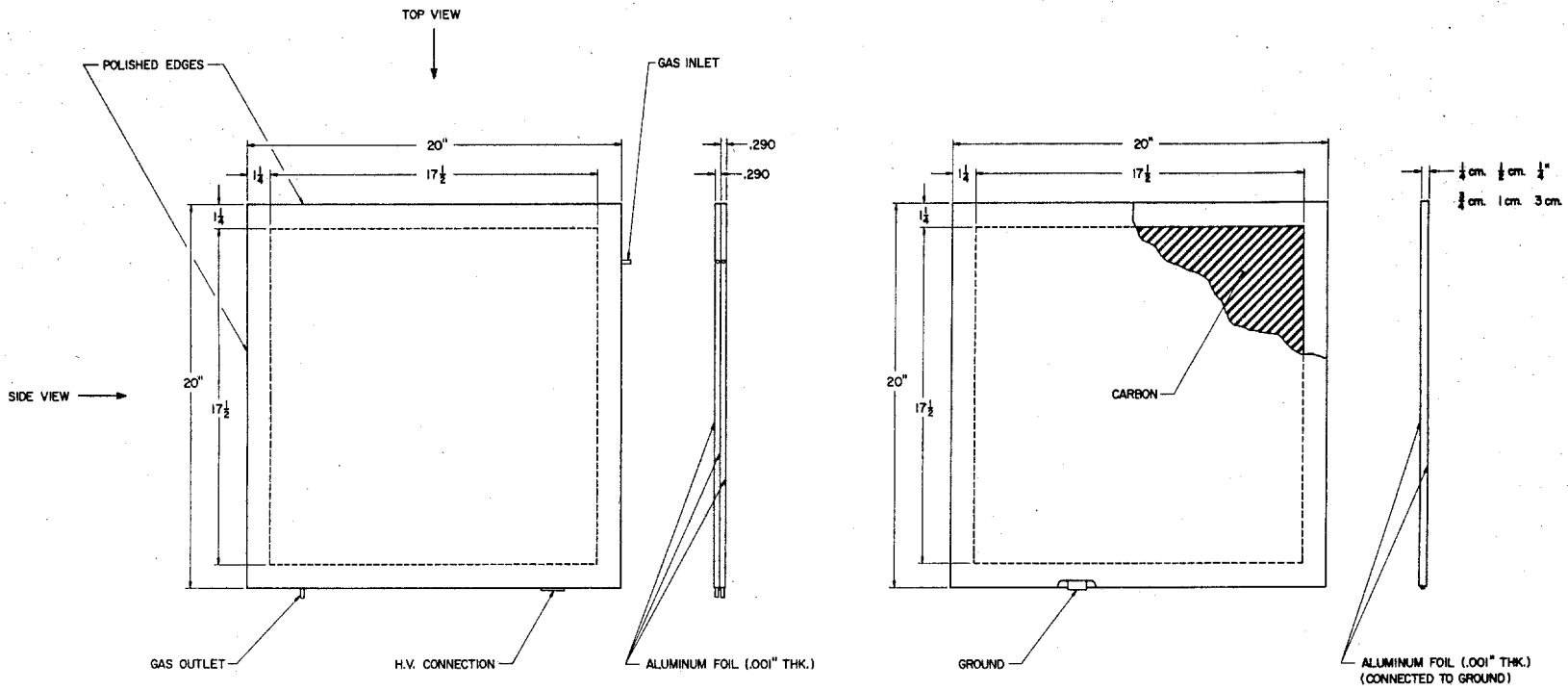

SPARKING MODULE

CARBON MODULE

FIGURE 31 Spark Chamber Modules

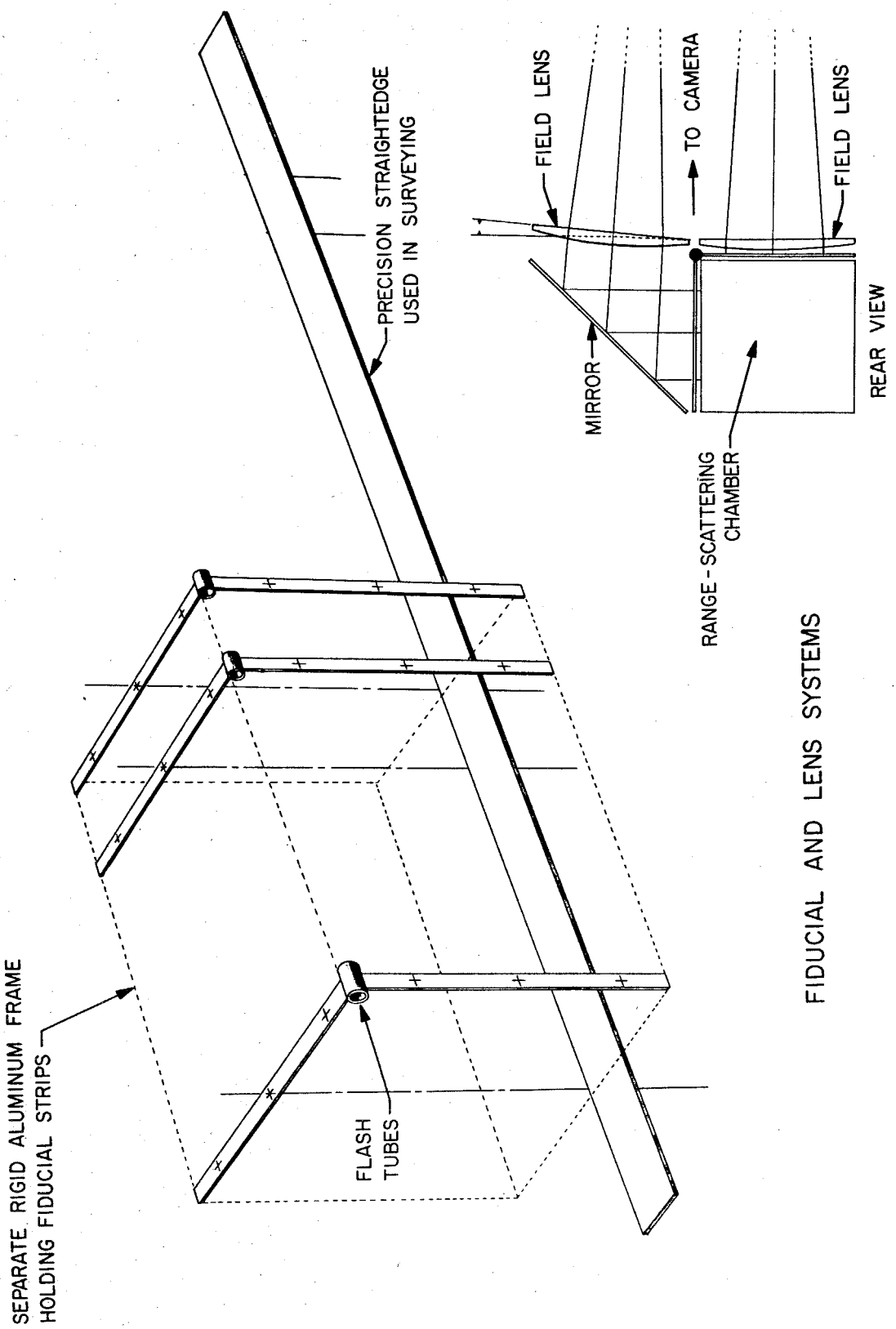

FIDUCIAL AND LENS SYSTEMS

FIGURE 32

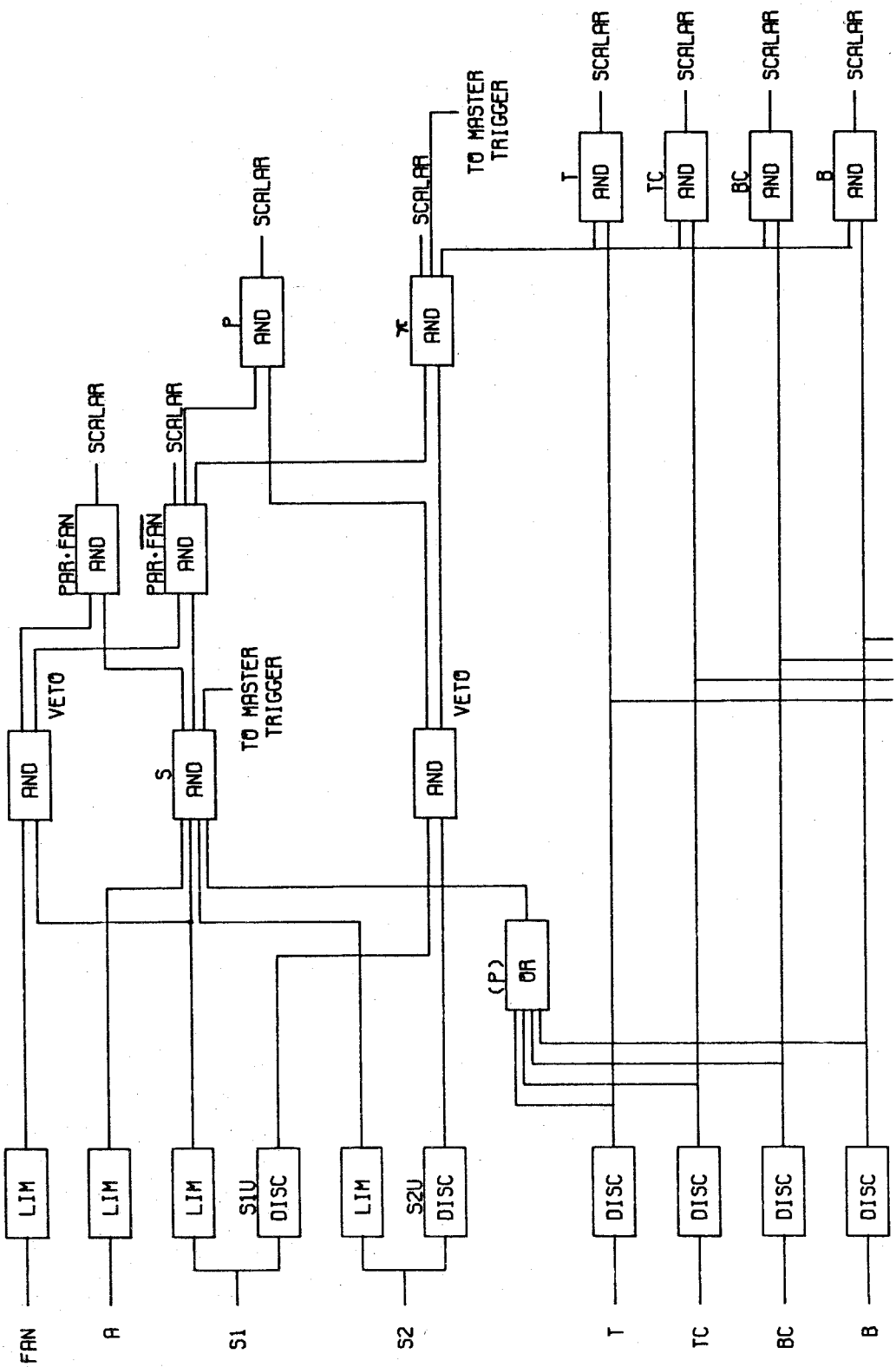

FIGURE 33 LEM Electronics

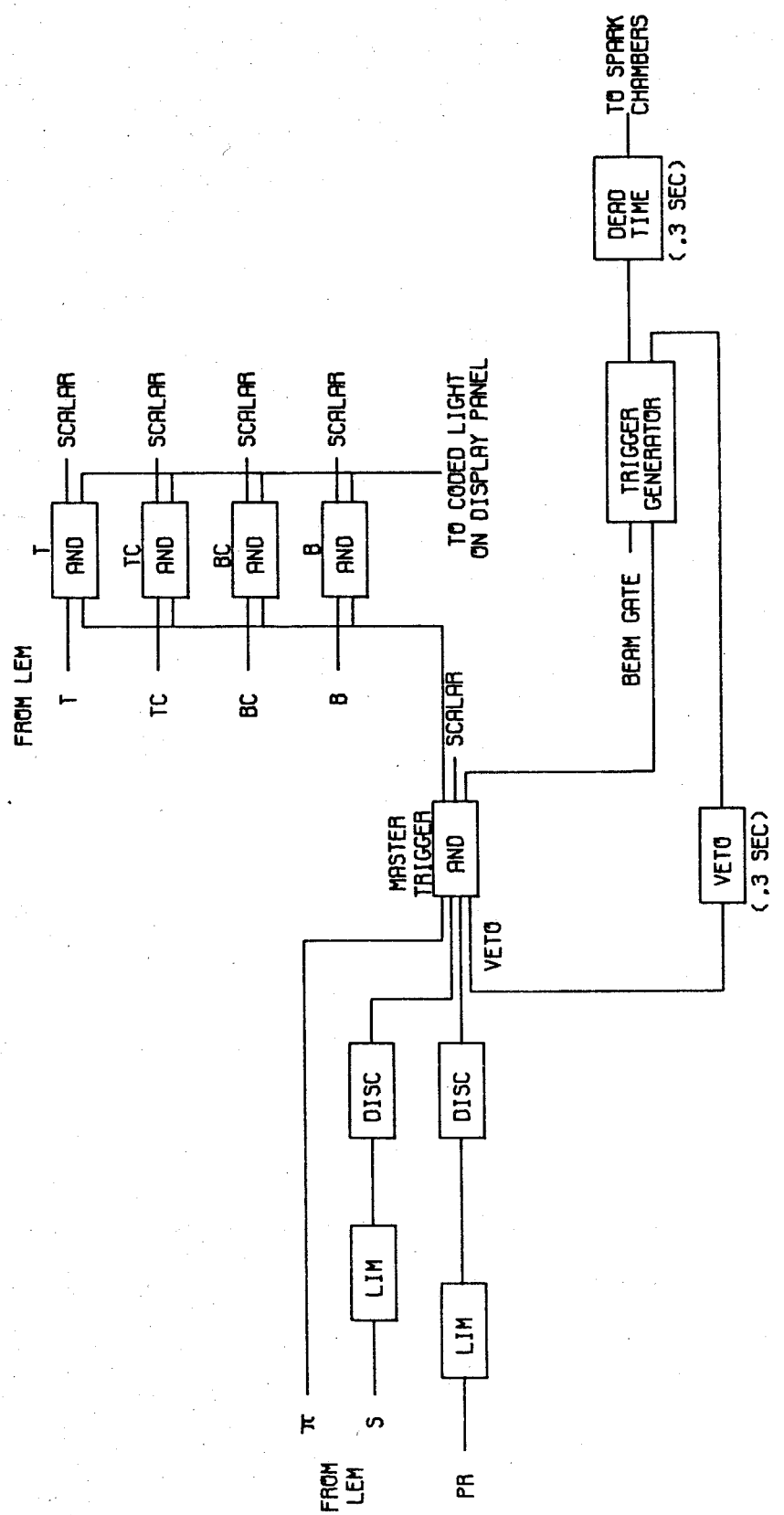

FIGURE 34

Spark Chamber Electronics

APPENDIX B. BACKGROUNDS

Any event which can trigger a coincidence between the proton counter in front of the range chamber and one of the momentum channels of the spectrometer, but which does not come from the reaction being studied is of course an unwanted background which could affect the value of the polarization.

One possible background would be a particle which wasn't a proton firing the proton counter and causing an accidental coincidence. However, even if such an event escaped the pulse height criteria on the proton counter it would be easily eliminated by the particle's subsequent track in the range chamber. Electrons are clearly distinguishable because of their undulating tracks and pions very rarely stop in the chamber, being minimum ionizing particles. Thus the only serious background on this side of the experiment would come from protons that didn't originate in the desired reaction, but were in coincidence with a pion in the spectrometer. Backgrounds of this type will be discussed below (Section B. 2).

Contamination from undesired particles is potentially more serious in the spectrometer. Protons are eliminated with almost 100% efficiency by the fact that the LEM was set up to detect negative, minimum ionizing particles. Pions which come from reactions other than the desired one are again a problem only if they are in coincidence with a proton on the spark chamber side of the experiment. Unfortunately the LEM is also unable to distinguish among pions, electrons, and muons. Contamination due to the latter two particles will be considered in the next section.

B.1 Muon and Electron Contamination in the LEM

At one time e^- contamination was felt to be a negligible problem for the lab pion angles at which the spectrometer was set in this experiment. However, the π^- cross section measurements of Walden and Scheffler [21, 22] show a serious discontinuity at CM pion angles of 90^o and greater which was felt to be due to electron contamination [22]. In fact their cross section determinations from detection of only the π^- had to be rejected for this reason. Fortunately their cross section determinations for cases where they detected the π^- and the recoil proton in coincidence did not show any such effect and agreed, without any correction for electron contamination, quite well with π^-/π^+ ratio measurements for the kinematical settings used in the present experiment [21]. Therefore, since a π^- - proton coincidence is required in the present experiment, it will be assumed that the electron contamination in the LEM is a negligible effect (less than 1%).

Muon events are not really a contamination in the sense that the primary source of such muons, especially when the proton coincidence is included, are pions from the reaction being studied. The probability that the pion will decay via $\pi^- \rightarrow \mu^- \nu$ before passing completely through the spectrometer counter system varies from about 5% for the highest pion momentum setting (600 MeV/c) to approximately 19% for the lowest pion momentum setting (250 MeV/c). If these muons were then lost to the system this effect could simply be ignored since the decay of the π^- is uncorrelated with the recoil proton polarization in the production reaction. However, there is non-zero

probability that this muon will then be detected by the spectrometer. The acceptance of the LEM for muons from the decay $\pi^- \rightarrow \mu^- \nu$, K_μ, has been calculated by Monte Carlo methods [21, 41]. The results are plotted in Figure 35 as a function of $m_\pi L_o / P_o c\tau$, where m_π is the mass of the pion, L_o is the distance from the center of the target to the last counter in the spectrometer system (about 430 cm), P_o is the central setting of the spectrometer, and $c\tau \simeq 781$ cm for the pion. K_π is the acceptance for detection of undecayed pions at this same spectrometer setting. The ratio K_μ / K_π is presumably not much affected by whether or not the recoil proton is detected.

The effect of these $\pi^- \rightarrow \mu^- \nu$ events is to cause a broadening of the resolution in pion momentum. This effect is shown in Figure 36 which shows (for a given momentum channel)* the acceptance for detecting $\pi^- \rightarrow \mu^- \nu$ events for a given pion momentum P. P_o is now the central momentum setting for the channel in question. The broad main peak is due primarily to pions which decay after passing through the magnet but before reaching the last spectrometer counter, and the long tail is primarily due to events that decay before reaching the magnet. The analogous curve for the acceptance of undecayed pions lacks this long tail and is much narrower. The ratio of the widths for the π-μ to pion acceptances is given by [21]

$$\sigma_\mu / \sigma_\pi = 7.22 - (0.00484) P_o$$

---

* The curves for other channels and for other values of P_o vary in size but are almost identical in shape. The curve in Figure 36 is based on the Monte Carlo calculations of Thiessen [41].

where again P_o is the central momentum setting of the spectrometer.

Therefore, when quoting the pion momentum resolution, it must be remembered that for some indistinguishable fraction of the events (about 10% in all) this resolution is considerably broader than the quoted value. Other than this broadening of the resolution, π-μ events are no problem in the present experiment since: (1) the π-μ acceptance curve (Figure 36) peaks at the pion momentum which the spectrometer is set to detect (within the resolution σ_π) so the kinematics are the same except for the broadening; and (2) the decay or non-decay of the pion before passing through the spectrometer system is, of course, uncorrelated to the polarization of the recoil proton in the production reaction since the spinless pion has no mechanism for "remembering" this polarization.

B.2 2π Background

The only potentially serious background involving both a π^- and a proton in the final state comes from 2π production reactions. In photoproduction experiments from hydrogen this contamination is largely overcome by setting the synchrotron endpoint below the 2π acceptance thresholds of the spectrometer channels.

For photoproduction from deuterium, however, the $\gamma d \rightarrow \pi\pi NN$ threshold ($E^{CM} = 2m_\pi + 2M_N$) is given by

$$k_{lab} = 2m_\pi \left(\frac{m_\pi + 2M_N}{2M_N}\right) ,$$

since

$$E^{CM^2} = (k+P_D)^2 = M_D^2 + k_{lab}\, M_D \text{ and } M_D \simeq 2M_N .$$

In this formula m_π, M_N and M_D are the pion, nucleon and deuterium masses respectively. This threshold is obviously lower than the $\gamma N \rightarrow \pi\pi N$ threshold from hydrogen which is

$$k_{lab} = 2m_\pi\left(\frac{m_\pi + M_N}{M_N}\right) .$$

Furthermore, the Fermi motion of the initial nucleons broadens the acceptances in the deuterium case. These factors, coupled with the normal fall-off of the photon spectrum near the endpoint, mean that it is impossible to set the endpoint below the 2π threshold for at least the lowest momentum channel. This effect is shown schematically in Figure 37* where the Bremstrahlung spectrum is plotted along with the single π and 2π spectrometer acceptances.

It was therefore feared that 2π contamination might be a serious effect in deuterium experiments. Pat Walden [21] has done extensive Monte Carlo calculations of this contamination in the kinematical region of the present experiment using a spectator model along with the available data on the reactions

$$\gamma N \rightarrow \rho N, \quad \rho \hookrightarrow \pi\pi$$

$$\gamma N \rightarrow N^* \pi, \quad N^* \hookrightarrow N\pi$$

and

$$\gamma N \rightarrow \pi\pi N \text{ (non-resonant)}.$$

---

* The separation of the spectrometer channels is slightly exaggerated in this figure and the resolutions shown are somewhat narrower than the actual acceptances, especially for the 2π channels.

When a π^- and proton are required in the final state the only significant background reactions are believed to be $(\gamma p)n \rightarrow (\pi^- \pi^+ p)n$ and $(\gamma n)p \rightarrow (\pi^- \pi^o p)p$. The calculations showed that, as expected, the 2π background was essentially zero except for the lowest spectrometer channel. What was perhaps unexpected was that even for this channel the contamination was quite small. In the kinematic region covered by the present experiment this background was below 1% [21]. One reason for this is that the 2π background was found to be greatly suppressed until there is sufficient energy to form a N^* along with a pion and a spectator nucleon.

In summary, it is felt that the total background contamination in this experiment is at most on the order of 2%. This is far below the statistical errors and the systematic error due to the experimental resolutions.

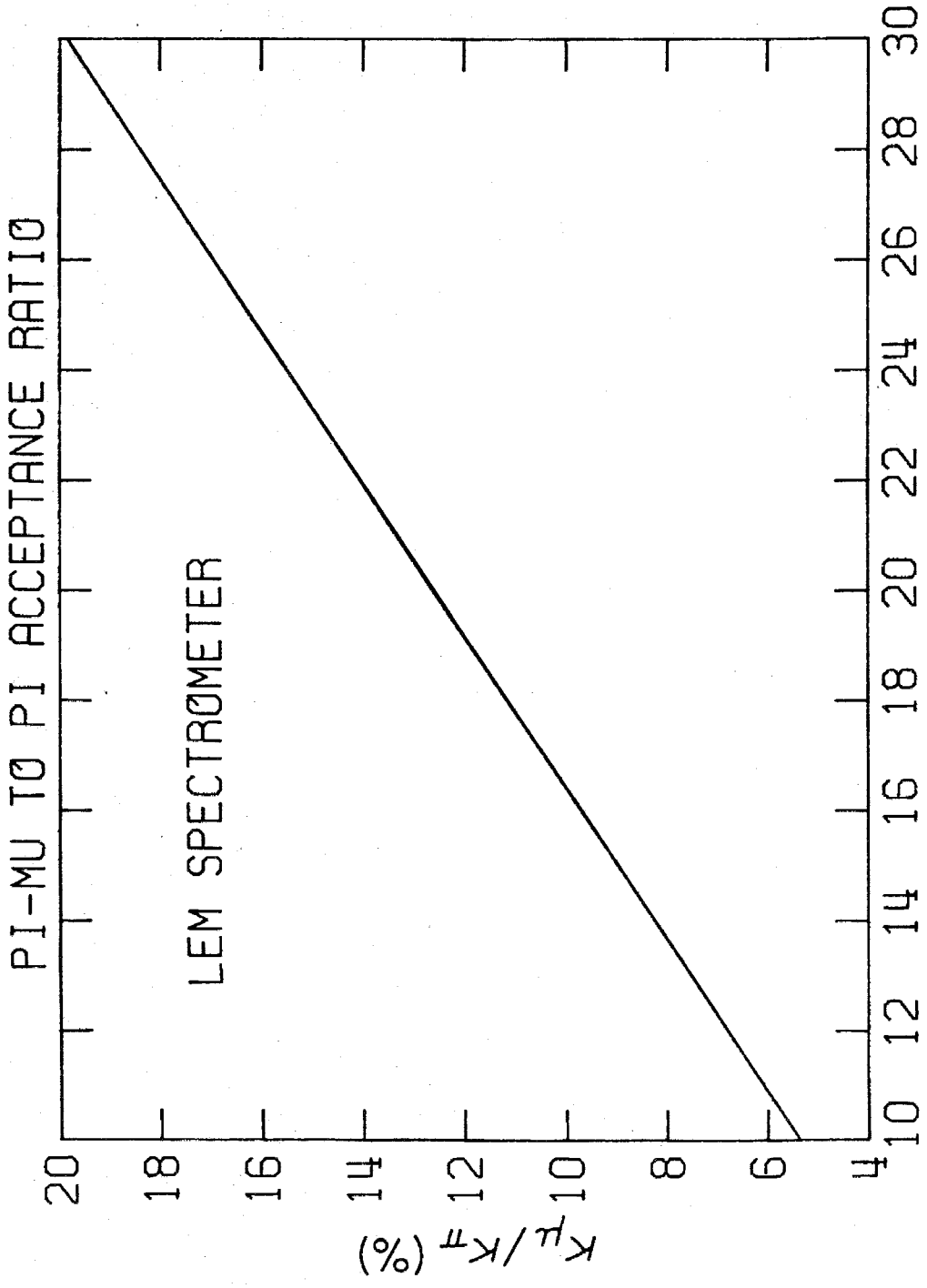
PI-MU TO PI ACCEPTANCE RATIO
LEM SPECTROMETER
K_μ/K_π (%)
$(m_\pi L/Pc\tau)\times 10^{+2}$
20
18
16
14
12
10
8
6
4
10
12
14
16
18
20
22
24
26
28
30

FIGURE 35

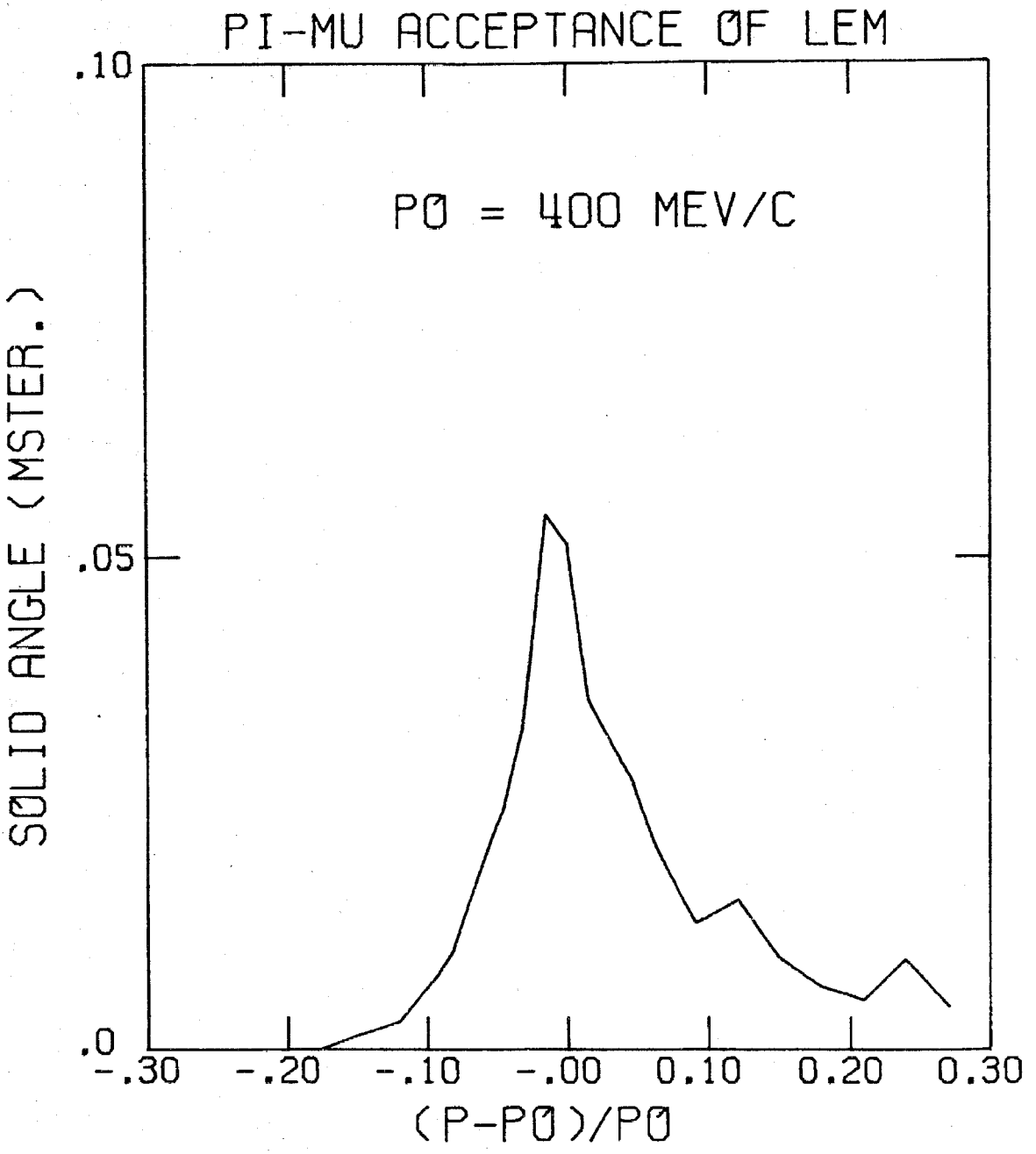
PI-MU ACCEPTANCE ØF LEM
PØ = 400 MEV/C
SØLID ANGLE (MSTER.)
.10
.05
.0
-.30
-.20
-.10
-.00
0.10
0.20
0.30
(P-PØ)/PØ

FIGURE 36

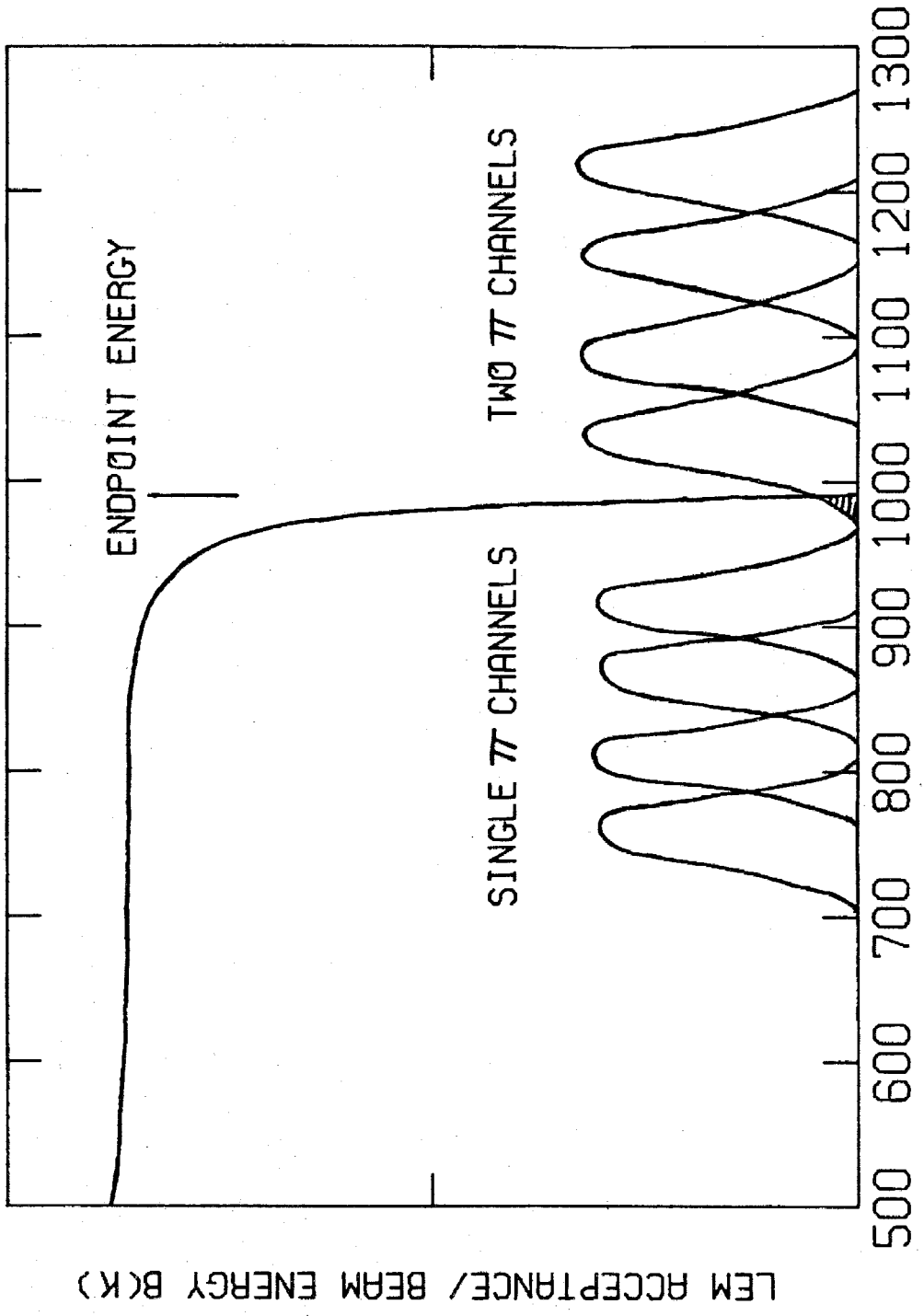

FIGURE 37 Schematic Representation of 2π Contamination

APPENDIX C. EXPERIMENTAL AND SCANNING BIASES

In order to obtain an accurate value for the polarization of the recoil proton any right-left bias in the analysis of the p-C scatters must be removed from the experimental and scanning procedures. One possible source of such a bias would be background contamination. However, as discussed in Appendix B, such contamination is believed to be very small compared to the statistical uncertainties in the present experiment. Therefore any possible polarization of this background will be ignored, except for a small contribution to the systematic error.

Other possible sources of bias come from the scanning procedures and from effects of the experimental procedure. These two effects will be discussed in the following paragraphs.

C.1 Scanning Efficiencies and Biases

To see how the scanning procedure could bias the polarization determination imagine that the film exposed during the experimental running contained N events that met scanning criteria (cf. Section 3.1). Then if the scanners of group I found N_1 of these events and those of group II found N_2 of them, the efficiencies, ϵ_i, of these scanners are defined by

$$N_i = \epsilon_i N \quad (i = 1, 2) \tag{C.1}$$

In order to make an estimate of these efficiencies the following assumptions will be made: (1) The process of finding an event is a statistical one with a "probability" $\epsilon_1(\epsilon_2)$ that scanner I(II) will find any given event; and (2) this probability is the same for all events.

With these assumptions the number of events found by both scanners I and II, N_{12} should be

$$N_{12} = \epsilon_1 \epsilon_2 N$$

Then the best estimate that can be made of ϵ_1 on the basis of the scanning results is

$$\epsilon_1 = N_{12}/N_2 \qquad \text{(C.2)}$$

with an analogous expression for ϵ_2.

To get the uncertainty in these numbers note that with assumptions (1) and (2) the distribution in N_{12} for a given N_2 is a binomial distribution [44]

$$P(N_{12}) = \frac{N_2!}{N_{12}!(N_2-N_{12})!} \epsilon_1^{N_{12}} (1-\epsilon_1)^{N_2-N_{12}}$$

and from the variance of this distribution, again assuming fixed N_2, we then get

$$\Delta\epsilon_1 = \sqrt{\frac{\epsilon_1(1-\epsilon_1)}{N_2}} \qquad \text{(C.3)}$$

with a similar expression for $\Delta\epsilon_2$.

The above assumptions about the statistical nature of scanning, especially assumption (2), ignore factors such as film quality, improvement of scanners with experience and familiarity with the film, and the fact that all events do not have the same "visibility." For example, p-C scatters with a large value of $\theta_{p'}$ are far easier to spot than events with a small value of $\theta_{p'}$.* This last effect is the only one easily taken into account and in calculating the scanning

* For the coordinate system used in defining p-C scattering events see Figure 2.

efficiencies for the present experiment the events are divided into two groups of different visibility--those events with p-C scatters of 4-6°* and those with p-C scatters of 6-30°. Within these groups it will be assumed that finding an event is a statistical process with roughly the same probability of detection for each scatter.

The efficiencies for scanner groups I and II in this experiment were calculated from a random sample of some 15% of the events at each setting and the results are shown in Table 11. For the 6-30° scatters the efficiencies from one kinematical setting to the next were consistent within the errors and so these settings are all lumped together to give overall efficiencies for left ($\cos \phi_{p'} > 0$) and right ($\cos \phi_{p'} < 0$) p-C scatters.† These efficiencies were somewhat lower than the 97-98% that had been hoped for and this is attributed to several factors: (1) the film quality was not as good as on some previous experiments [23, 43]; (2) the scanners had very little time to familiarize themselves with the film before serious scanning began; and (3) the group II scanners were relatively inexperienced at the beginning of the experiment.

---

* The actual scanning cut was for events of $\theta_{p'} > 3°$ in one of the two views, but only events with $\theta_{p'} > \sqrt{2} \times 3°$ were used in the polarization calculations.

† It might be expected that p-C scatters, especially small angle ones, which occurred before the proton entered the range chamber would be difficult for the scanners to locate and that the efficiencies for settings with a large number of such scatters would be lower. However, no significant effect of this nature was observed.

The efficiencies for the 4-6° scatters were also lower than the hoped for 75% and the left-scatter efficiency for group II was particularly poor for these low angle events. More will be said about this below. For these 4-6° scatters the spread in efficiencies from setting to setting was somewhat greater, but since there were too few of these events (in our 15% sample) at most settings to be statistically meaningful they have also been lumped together. The same factors as above contributed to the somewhat disappointing efficiencies. Also the fact that this experiment did not use thin foil chambers in front of the range chamber to help in definition of the initial trajectory made small angle scatters harder to pick out than in experiments that did use such chambers [23, 43].

Since the polarization is calculated by maximizing the probability of the observed distribution, the individual efficiencies are not especially critical as long as there is no right-left bias in the efficiency for events of roughly similar analyzing power. In order to test for such a bias we define an asymmetry parameter [43]

$$a \equiv \frac{\epsilon_R - \epsilon_L}{\epsilon_R + \epsilon_L} \qquad \text{(C.4)}$$

with

$$(\Delta a) = 2\,\epsilon_L \epsilon_R / (\epsilon_L + \epsilon_R)^2 \left[(\Delta\epsilon_R/\epsilon_R)^2 + (\Delta\epsilon_L/\epsilon_L)^2 \right]^{\frac{1}{2}}$$

The results for these asymmetry parameters for scanner groups I and II for both the 4-6° and the 6-30° scatters are given in Table 12. For all but one group this asymmetry is easily consistent

with zero. The only problem is the group II results for small angle scatters where the asymmetry is at least two standard deviations away from zero.* The only apparent explanation for this asymmetry is that, because of inexperience, the scanners in group II improperly used the grid which defined the trajectories of particles coming from the target and therefore rejected many of the actual 4-6° left-scatters as being less than 4°. Fortunately this asymmetry does not seriously affect the polarization for several reasons: (1) these 4-6° scatters make up no more than 10% of the event sample and at the settings where the asymmetry is the worst they average only 6% of the sample; (2) the analyzing power for these small angle scatters averages 30% (or less) of the analyzing power for the large angle scatters; and (3) more importantly, the more efficient scanners of group I did not show any significant asymmetry for these small angle scatters. Therefore, the bias of the group II scanners was greatly reduced in the verifying scan which resolved conflicts between the two groups. In summary, it is felt that the error resulting from this one non-zero asymmetry is well below the statistical errors and the systematic error due to the uncertainty in the analyzing power.

C.2 Experimental Bias

The main experimental worry as far as a right-left bias is concerned is that the efficiency of detecting a p-C scatter to the right

* This effect is present with roughly the same value at all but one of the individual kinematical settings. The lack of asymmetry for large angle scatters and for group I in general also holds for each individual setting within the statistical uncertainties.

or to the left could depend on the position of the scatter in the chamber, especially if the chamber was not exactly "centered" for a particular kinematical setting. Effects such as spark efficiency and optical distortion could contribute to such a bias. However, such effects are felt to be negligible for our apparatus [23, 43] and the main concern is, therefore, with events that might leave the chamber. As discussed in Section 3, such events must be rejected because in these cases the proton energy and, therefore, the kinematics of the event, are undetermined. Any right-left asymmetry in these rejections would, of course, introduce a bias. In order to avoid such a bias it is insufficient to simply reject events which leave the fiducial volume. An event must also be rejected if its reflection in $\phi_{p'}$ (i.e. an event with $\phi_{p'} \rightarrow \phi_{p'} + 180^{o}$) would have left the fiducial volume. Such an event is shown in Figure 38 (a). These events can clearly not be used in the determination of the polarization since they would have been rejected had they scattered "the other way."

Actually, as Bruce Winstein has pointed out [23], the above restriction is too stringent if one is interested only in the polarization along $\hat{k} \times \hat{p}_R$. In such cases an event can be used even if $\phi_{p'}+180^{o}$ leaves the chamber as long as $180^{o}-\phi_{p'}$ <u>doesn't</u> leave the chamber and $360^{o}-\phi_{p'}$ <u>does</u> (see Figure 38 (b)). Such a situation corresponds to being sensitive to only 1/2 of the total range in $\phi_{p'}$. In practice the modification of the likelihood calculation to account for this partial sensitivity in $\phi_{p'}$ is more trouble than the few events salvaged warrant. Furthermore, the more general criteria of $\phi_{p'}+180^{o}$ not leaving the chamber has the virtue that it also eliminates bias for the

polarization in the reaction plane ($\hat{k} \times \hat{p}_R$) which may be non-zero in this experiment (see Section 3.4). Therefore, this more general criterion has been used in this experiment.

As a final check on experimental bias the polarization perpendicular to the reaction plane was separately calculated for the right and left hand sides of the range chamber for each kinematical bin.* The results were consistent, within the statistical errors, for all cases except the 675-120° bin where the values differed by about two standard deviations. When the systematic error is included even this bin is not inconsistent.

* The kinematical bins are those defined in Table 3.

TABLE 11

Scanning Efficiencies*

Small angle p-C scatters ($4^{\circ} \leq \theta_{p'} \leq 6^{\circ}$)

Group I	Group II
$\epsilon_L = 64.3 \pm 4.4\%$	$\epsilon_L = 49.7 \pm 4.1\%$
$\epsilon_R = 68.6 \pm 4.2\%$	$\epsilon_R = 62.9 \pm 4.2\%$

Large angle p-C scatters ($6^{\circ} < \theta_{p'} \leq 30^{\circ}$)

Group I	Group II
$\epsilon_L = 95.0 \pm 0.91\%$	$\epsilon_L = 92.4 \pm 0.84\%$
$\epsilon_R = 94.6 \pm 0.65\%$	$\epsilon_R = 92.7 \pm 0.75\%$

* ϵ_L and ϵ_R are the efficiencies for left ($\cos \phi_{p'} > 0$) and right ($\cos \phi_{p'} < 0$) scatters respectively.

TABLE 12

Scanning Biases *

Small angle p-C scatters ($4^{\circ} \leq \theta_{p'} \leq 6^{\circ}$)

Group I	Group II
$a = 0.032 \pm 0.046$	$a = 0.117 \pm 0.052$

Large angle p-C scatters ($6^{\circ} < \theta_{p'} \leq 30^{\circ}$)

Group I	Group II
$a = -0.0021 \pm 0.0056$	$a = 0.0016 \pm 0.0061$

* $a \equiv \dfrac{\epsilon_R - \epsilon_L}{\epsilon_R + \epsilon_L}$

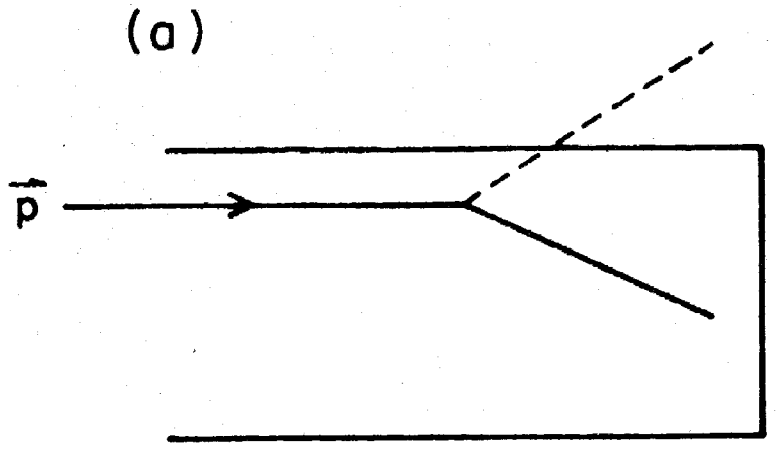

Diagram of Event Not Used in the Polarization Calculation

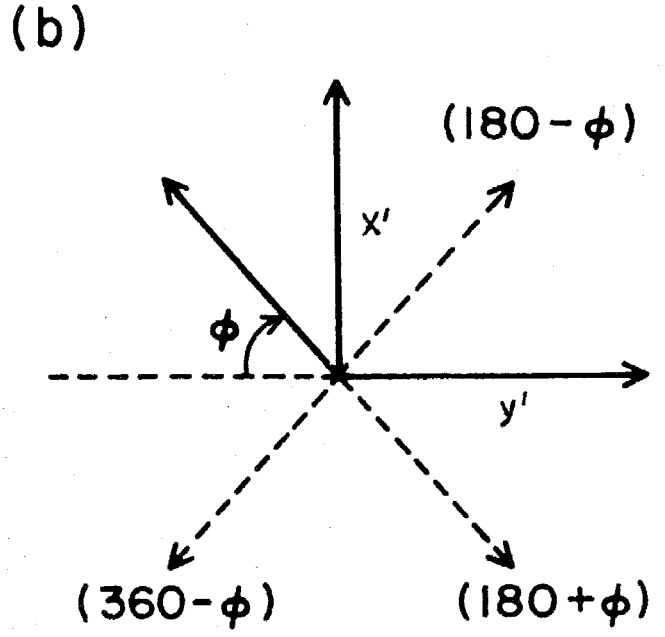

Representation of the ϕ Angle in a p-C Scatter

FIGURE 38

APPENDIX D. MONTE CARLO CALCULATIONS

The kinematics of the individual events in this experiment are barely determined by the quantities measured (see Section 3.3). Furthermore, the resolution in the energy of the recoil proton is quite broad due to the possible inelasticity in the p-C scatters. Therefore, although any backgrounds are expected to be quite small, there is no easy way to verify this assumption just from the quantities measured for each event. More importantly, there are no real checks that can be made on the overall reconstruction procedure from the data alone.

In order to provide such a check, Monte Carlo calculations have been made of the expected distributions in various kinematical quantities. These calculations, using the $\gamma n \rightarrow \pi^- p$ cross sections of Walden and Scheffler [21, 22], are discussed below. The results, described in Section 3.3, indicate that there are no obvious difficulties with the reconstruction analysis.

D.1 Rate Calculation

Consider the reaction $\gamma d \rightarrow \pi^- p_R p_S$ and let $K = (k, \vec{k})$, $P_D = (E_D, \vec{p}_D)$, $Q = (\omega, \vec{q})$, $P_R = (E_R, \vec{p}_R)$ and $P_S = (E_S, \vec{p}_S)$ be the four-momenta of the photon, deuteron, pion, recoil proton, and spectator proton respectively. The corresponding masses are 0, M_D, m_π, M_p and M_p. All wave functions will be normalized such that $\langle p' | p \rangle = 2E\, \delta(\vec{p}-\vec{p}')$.

The first step in generating distributions for this reaction is to express its rate in terms of known quantities or at least ones that

can be randomly selected from a known range. The differential cross section for $\gamma d \rightarrow \pi^- p_R p_S$, $d\sigma_D$, is given by [18]

$$d\sigma_D = \frac{|\langle \pi^- p_R p_S | M | \gamma d \rangle|^2}{v 2k 2E_D} (2\pi)^4 \delta(K + P_D - Q - P_R - P_S) \times$$
$$\times \delta(Q - m_\pi^2) \frac{d^4Q}{(2\pi)^3} \delta(P_R^2 - M_p^2) \frac{d^4P_R}{(2\pi)^3} \delta(P_S^2 - M_p^2) \frac{d^4P_S}{(2\pi)^3} \qquad (D.1)$$

where M is the invariant amplitude for this process. The relative velocity of the initial particles is v = c = 1 and therefore using the δ functions we get that in the lab system

$$d\sigma_D = \frac{|\langle \pi^- p_R p_S | M | \gamma d \rangle|^2}{2k 2M_D} \frac{d^3q}{2\omega(2\pi)^3} \frac{d^3p_R}{2E_R(2\pi)^3} \times$$
$$\times (2\pi)\delta(P_S^2 - M_p^2) \qquad (D.2)$$

with $K + P_D = Q + P_R + P_S$.

Now consider the matrix element $\langle \pi^- p_R p_S | M | \gamma d \rangle$ in terms of the diagram in Figure 39. The deuteron is just a proton (S) and a neutron (n) each with a momentum distribution given by the Hulthen wave function $\phi(p_S)$.* Therefore,

$$|d\rangle = \sqrt{2E_D}\, \phi(p_{S'}) \frac{|\vec{p}_{S'}\rangle}{\sqrt{2E_{S'}}} \frac{|\vec{p}_n\rangle}{\sqrt{2E_n}} \quad (\vec{p}_D = \vec{p}_n + \vec{p}_S)$$

or

$$\langle \pi^- p_R p_S | M | \gamma d \rangle = \langle \pi^- p_R | M' | \gamma n \rangle \langle \vec{p}_S | \vec{p}_{S'} \rangle \sqrt{2E_D}\, \phi(p_S) / \sqrt{2E_n 2E_S} \qquad (D.3)$$

where M' refers only to vertex V_2 in Figure 39 and the rest of the expression describes vertex V_1.

* $$\phi(p_S) = \left[\frac{\alpha}{\pi^2(1-\alpha\rho)}\right]^{\frac{1}{2}} \frac{(\beta^2 - \alpha^2)}{(\alpha^2 + p_S^2)(\beta^2 + p_S^2)} \qquad (D.3a)$$

where α = 45.69 MeV, β = 275.74 MeV, and ρ = 0.00882 MeV [22].

The spectator model, in its simplest form, now assumes that the spectator proton is unaffected by the interaction such that $\langle \vec{p}_S | \vec{p}_S' \rangle = 2E_S \, \delta(\vec{p}_S - \vec{p}_S')$. Using this and substituting (D. 3) and (D. 2) yields

$$d\sigma_D = \frac{|\langle \pi^- p_R | M' | \gamma n \rangle|^2}{2k\,2E_n} (2E_S |\phi(p_S)|^2)\, 2\pi\delta(P_S^2 - M_p^2) \times \times \frac{d^3q}{2\omega(2\pi)^3} \frac{d^3p_R}{2E_R(2\pi)^3} \tag{D.4}$$

The neutron in Figure 39 is virtual; however, assuming that it is on the mass shell* the matrix element $\langle \pi^- p_R | M' | \gamma n \rangle$ can be related to the cross section for the process $\gamma n \rightarrow \pi^- p_R$. Namely,

$$(d\sigma/d\Omega(\gamma n \rightarrow \pi^- p_R))_{CM} \equiv (d\sigma_N/d\Omega)_{CM} = q_{CM}/k_{CM} |\langle \pi^- p | M' | \gamma n \rangle|^2/(8\pi W)^2 \tag{D.5}$$

where

$$W \equiv (E_R + \omega)^2 - (\vec{p}_R + \vec{q}) \tag{D.6}$$

is the total energy of the pion and recoil proton in their center-of-mass frame and k_{CM} and q_{CM} are the photon and pion momenta in this frame. Substituting (D. 5) into (D. 4) gives $d\sigma_D$ in terms of the $\gamma n \rightarrow \pi^- p$ cross section,

$$d\sigma_D = \frac{2k_{CM}\, W^2}{(2\pi)^3 k E_n q_{CM}} \left(\frac{d\sigma_N}{d\Omega}\right)_{CM} \frac{q^2 dq d\Omega_q}{\omega} \frac{p_R^2 dp_R d\Omega_R}{E_R} \times \times \phi^2(p_S) E_S\, \delta(P_S^2 - M_p^2) \tag{D.7}$$

---

* This assumption means replacing the neutron's energy in its virtual state $E_n = M_D - E_S$ by $\sqrt{p_S^2 + M_n^2}$. This amounts to an error of at most 1.5% for the spectator momenta considered in this simulation ($p_s \leq 150$ MeV/c).

At this point we must digress to do some necessary kinematics. For the rest of this appendix quantities not specifically labelled CM will refer to the laboratory frame of the reaction $\gamma d \rightarrow \pi^- p_R p_S$ and quantities labelled CM will refer to the center-of-mass frame of the pion and the recoil proton.

In this CM frame

$$q_{CM} = (W^2 + m_\pi^2 - M_p^2)/2W \tag{D.8a}$$

To get k_{CM}, consider the invariant $K\cdot(Q+P_R) = K\cdot(P_D+K-P_S)$. Evaluating the left-hand side in the CM frame and the right-hand side in the lab frame gives

$$k_{CM} = \frac{k}{W}\,(M_D - E_S + p_S \cos\theta_S) \tag{D.8b}$$

where $\cos\theta_S = \hat{p}_S \cdot \hat{k}$. ($\hat{p}_S$ is calculated directly from $K+P_D = Q+P_R+P_S$ once the other four-vectors are known.)

Next consider the invariant

$$P_S^2 = (K+P_D-P_R-Q)^2 \tag{D.9}$$

Expanding this and differentiating with respect to k gives the expression

$$\partial P_S^2/\partial k = 2M_D - 2(\omega - q\cos\theta_\pi) - 2(E_R - p_R\cos\theta_R) \tag{D.10}$$

where $\cos\theta_\pi = \hat{q}\cdot\hat{k}$ and $\cos\theta_R = \hat{p}_R\cdot\hat{k}$. This expression is useful in relation

$$\delta(P_S^2 - M_p^2) = \delta(k-k') \left| \partial P_S^2/\partial k \right|^{-1}_{k=k'} \tag{D.11}$$

where k' is the value of k such that $P_S^2 = M_p^2$. But this is just the real lab photon energy, k, which can be obtained by going back to

to (D. 9) and setting $P_S^2 = M_p^2$. This gives

$$k = [M_D^2 + m_\pi^2 - 2M_D(E_R+\omega) + 2(\omega E_R - qp_R\cos\theta_{\pi R})]/2[(\omega - q\cos\theta_\pi) + (E_R - p_R\cos\theta_R) - M_D] \quad (D.12)$$

where the only previously undefined quantity is $\cos\theta_{\pi R} = \hat{q}\cdot\hat{p}_R$.

Finally, we consider two quantities which do not enter the cross section formula, but in terms of which the values of $(\frac{d\sigma_N}{\partial\Omega})_{CM}$ are reported [21]. The first is k_N, the energy a photon would need in striking a <u>free</u> neutron at rest in order to produce the observed value of W. This is just

$$k_N = (W^2 - M_n^2)/2M_n$$

The second is θ_π^{CM}, the pion angle in the CM frame. It is obtained by evaluating the invariant $K\cdot Q$ in the CM frame and in the lab frame,

$$(k_{CM}\omega_{CM} - k_{CM}q_{CM}\cos\theta_\pi^{CM}) = (k\omega - kq\cos\theta_\pi)$$

where all the quantities except for θ_π^{CM} have been previously defined.

Returning now to the rate calculation, we note that the number of events, C, expected at a given kinematical setting for a given spectrometer acceptance, $dqd\Omega_q$, and a given spark chamber configuration is

$$C = \int \Phi(k) \frac{d^2\sigma_D}{dq\, d\Omega_q}\, \eta L(RC)\, dq\, d\Omega_q\, dk \quad (D.14)$$

In this formula: η is the target density; L is the photon path length in the target; RC is a function with the value 1 if the recoil proton

stops in the range chamber after undergoing acceptable (see Section 3.1) p-C scatter and the value 0 otherwise; and $\Phi(k)$ is the number of photons of energy k to k+dk striking the target at this setting.

The Bremstrahlung-spectrum function, $B(k, E_o, x, y)$, is defined by

$$\Phi(k) = Q/E_o \int \frac{B(k, E_o, x, y)}{k} dxdy \qquad (D.15)$$

where E_o is the synchrotron endpoint energy, Q is the total energy in the beam for this setting, and x and y are the position in target (see Figure 2 for the coordinate system used). In terms of y and the target radius, R, $L = 2(R^2-y^2)^{\frac{1}{2}}$.

Substituting (D.15) and (D.7) into (D.14), and using (D.11) to do the integral over dk, we get

$$C = 2\eta Q/E_o \int \frac{B(k,E_o,x,y)}{k} \left[\frac{2k_{CM} W^2}{(2\pi)^3 k E_n q_{CM}} \left(\frac{d\sigma_N}{d\Omega}\right)_{CM} \frac{q^2}{\omega} \frac{p_R^2}{E_R} \phi^2(p_S) E_S \left| \frac{\partial P_S^2}{\partial k} \right|^{-1} \right] \times \qquad (D.16)$$

$$\times \quad dq \sin\theta_\pi d\theta_\pi d\phi_\pi dp_R \sin\theta_R d\theta_R d\phi_R dxdy (R^2-y^2)^{\frac{1}{2}} (RC)$$

D.2 Monte Carlo Distributions

Before using (D.16) to calculate the distributions in various kinematical quantities a few modifications are necessary. First of all, in the Monte Carlo integration of this equation we do not actually pick q but rather the vertical position, ξ, at which the particle went through the spectrometer hodoscope. q is then a function, $f_q(\xi, x)$, of ξ and of the x position in the target; so we must replace dq by $\frac{\partial f_q}{\partial \xi} d\xi$. Also, we don't pick p_R but rather the range, R_E, of the recoil proton in carbon. The energy of the recoil proton is then a

function, $f_E(R_E)$, of this range. Therefore, dp_R must be replaced by $\frac{\partial p_R}{\partial E_R} \frac{\partial f_E(R_E)}{\partial R_E} dR_E$. The quantity $\frac{\partial f_E(R_E)}{\partial E_R}$ can be empirically tabulated from carbon range-energy curves, the other material that the recoil proton passes through making a negligible contribution.

The most important modification is in the function (RC). Just picking p_R, it would be easy to check that the proton stopped in the range chamber but a formidable calculation to decide if it underwent an acceptable p-C scatter. Therefore, the following procedure is used to simulate the range chamber part of the experiment. As mentioned above, rather than using p_R as an integration variable we use the range of the proton in the chamber and calculate E_R from this. This improves the efficiency of the Monte Carlo process by ensuring that no protons leave the back of the chamber. The complicated process of deciding if the proton made an "acceptable" p-C scatter is then circumvented by demanding that this is so! That is to say, a p-C scattering angle, $\theta_{p'}$ and energy of scatter, $T_{p'}$, are specified within the acceptable scanning limits ($4^o \leq \theta_{p'} \leq 30^o$, and a range of at least 3 spark modules after the p-C scatter) and the event is then weighted by the cross section, $\sigma_c(T_{p'}, \theta_{p'})$, for such a scatter.

Including these modifications in (D.16) and dropping all constant factors (which will be irrelevant when distributions are calculated), we obtain

$$C = \int \frac{B(k, E_o, x, y)}{k} \left[\frac{k_{CM} W^2}{k E_n q_{CM}} \left(\frac{d\sigma_N}{d\Omega}\right)_{CM} \frac{q^2}{\omega} \frac{p_R^2}{E_R} \phi^2(p_S) E_S \left| \frac{\partial P_S^2}{\partial k} \right|^{-1} \right] \times$$

$$(R^2 - y^2)^{\frac{1}{2}} dx dy \frac{\partial f_q(\xi, x)}{\partial \xi} d\xi \sin\theta_\pi d\theta_\pi d\phi_\pi \times \qquad \text{(D.17)}$$

$$\frac{\partial p_R}{\partial E_R} \frac{\partial f_E(R_E)}{\partial R_E} dR_E \sin\theta_R d\theta_R d\phi_R \sigma_c(\theta_{p'}, T_{p'}) d\theta_{p'} dT_{p'}$$

This formula is now suitable for calculation of "theoretical" distributions to be compared to the observed distributions in order to check for any serious problems in the analysis. The procedure used in generating these distributions is the following.

(1) The target position x and y are selected from the allowable ranges and $(R^2 - y^2)^{\frac{1}{2}}$ is calculated.

(2) The position in the hodoscope, ξ, along with the pion angles, θ_π and ϕ_π, are selected from the ranges allowed by the spectrometer acceptance at a given lab angle and magnet setting. q is then calculated and a table of values [45] for $\frac{\partial f_q(\xi, x)}{\partial \xi}$ is interpolated to give the necessary differential.

(3) The range of the recoil proton, R_E, along with its angles, θ_R and ϕ_R, are selected from the values allowed by the spark chamber configuration. E_R is then calculated from the range-energy relation given in Section 3.2 and a table of emperically determined values for $\frac{\partial f_E(R_E)}{\partial R_E}$ is interpolated to give the differential.

(4) All of the quantities necessary to calculate the kinematical variables defined in equations (D.6) to (D.13) are now available. $\phi^2(p_S)$ is also calculated using equation (D.3a).

(5) Using the above variables a table of $B(k, E_o, x, y)$ [45] can be interpolated to give this factor. Similarly, a table of Scheffler and Walden's cross section results [45] can be interpolated to give the value of $(d\sigma_N/d\Omega)_{CM}$.

(6) $\theta_{p'}$ and $T_{p'}$ are selected from the desired ranges and the value of $\sigma_c(\theta_{p'}, T_{p'})$ calculated* (actually the range after the p-C scatter is selected and $T_{p'}$ calculated from the range-energy relation).

(7) All the factors in the integrand of (D.17) have now been calculated.† This integrand is the weight, WGT, of the event just generated. To get the distribution in some kinematical variable, A, all that is necessary is to decide which bin the value of A for the event just generated belongs in. (It is assumed that the limits on this distribution as well as the bin size have been specified.) The value of WGT for this event is then added to this bin.

By repeating this process many times and then normalizing to the observed number of events a "theoretical" distribution for the quantity A can be generated. Since the ratio of the number of events that scatter in the chamber to the number that scatter before the chamber cannot be simply calculated, these two types of events are generated independently and then mixed in the observed proportions. Some of the results of these calculations are illustrated in Figures 4

---

* $\sigma_c(T_{p'}, \theta_{p'}) = \sigma_o(T_{p'}, \theta_{p'}) [1+\sum_{i=1}^{4} R_i (T_{p'}, \theta_{p'})]$ where the quantities on the right-hand side of this equation are defined and discussed in Appendix E.

† There are also factors for pion decay and nuclear absorption in the spectrometer. These factors vary slowly enough in q that they are essentially constant for a given kinematical setting and are not shown in (D.17).

to 11. These results are discussed in Section 3.3 and no further discussion will be given here except to emphasize that a reasonable agreement in the type of curves shown in Figures 4 to 11 guarantees a similar agreement in all of the important kinematical variables.

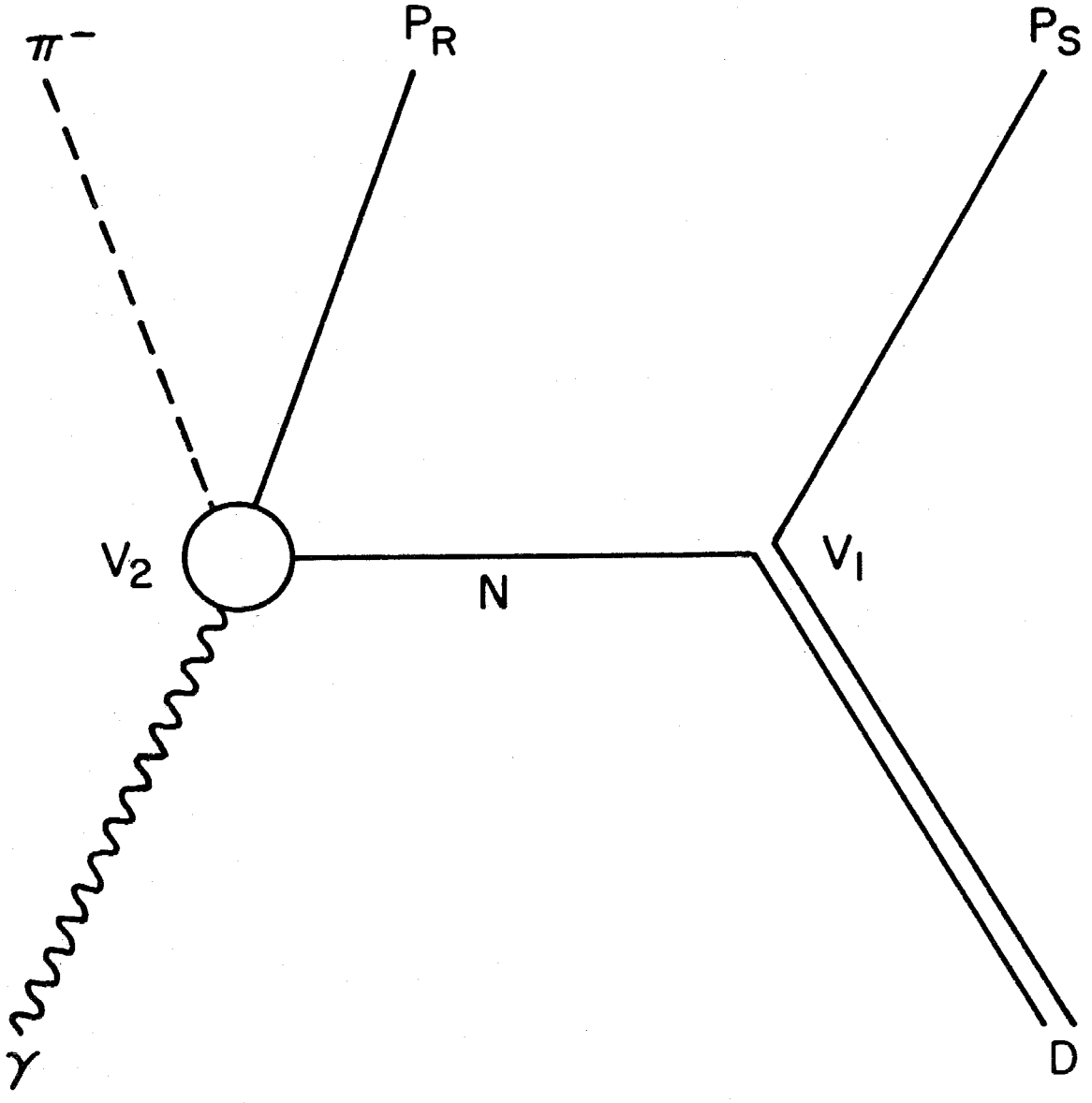

FIGURE 39 Spectator Model

APPENDIX E. THE ANALYZING POWER

Before indicating how the analyzing power of carbon was calculated for the individual p-C scatters in this experiment, a brief description will be given of how this analyzing power is measured. This may also clarify the concept of analyzing power as introduced in Section 2.2.

In Section 2.2 it was noted that the final density matrix, ρ_f, for a beam of protons with initial density matrix ρ_i and momentum $\vec{p}$, scattered from carbon, is given by

$$\rho_f = (f + \vec{\sigma}\cdot\hat{n}g)\ \rho_i (f + \vec{\sigma}\cdot\hat{n}g)^{+} \qquad \text{(E. 1)}$$

where f and g are functions of the proton energy, E, and the angle, θ, of the scatter. $\hat{n}$ is the normal to the scattering plane, $\hat{p} \times \hat{p}'$ with $\vec{p}'$ the final momentum. The cross section and the polarization of the final beam are then given by

$$d\sigma/d\Omega = \mathrm{Tr}\,\rho_f \qquad \text{(E. 2a)}$$

and

$$\vec{P} = \mathrm{Tr}\,\rho_f\vec{\sigma}/\mathrm{Tr}\,\rho_f \qquad \text{(E. 2b)}$$

respectively.

Now consider the following experiment: A beam of unpolarized protons, $\rho_i = \frac{1}{2}$, is elastically scattered from carbon at an angle θ such that the polarization of the scattered beam is given by

$$\vec{P} = 2\,\mathrm{Re}(f^{*}g)/(|f|^2+|g|^2)\,\hat{n} \equiv A_c(E,\theta)\hat{n} \qquad \text{(E. 3)}$$

where A_c is called the analyzing power of carbon. Now this beam is

allowed to scatter from carbon again at the same energy and with the same scattering angle. In this second scatter $\rho_i = \frac{1}{2}(1+\vec{P}\cdot\vec{\sigma})$ and therefore the cross section for this scattering is given by

$$\sigma(\theta, \phi) = \sigma_o(\theta)(1+A_c(E, \theta)|\vec{P}|\cos\phi) \qquad (E.4)$$

with $\cos\phi = (\hat{p}''\times\hat{p}')\cdot(\hat{p}'\times\hat{p})$ if $\hat{p}''$ is the momentum after the second scatter. $\sigma_o(\theta) = |f|^2 + |g|^2$ is the scattering cross section for an unpolarized beam. Substituting from (E. 3) for $|\vec{P}|$, we see that the asymmetry parameter

$$\epsilon \equiv (\sigma(\theta, \phi)|_{\cos\phi=+1} - \sigma(\theta, \phi)|_{\cos\phi=-1})/(\sigma(\theta, \phi)|_{\cos\phi=+1} + \sigma(\theta, \phi)|_{\cos\phi=-1})$$

has a value in this case of

$$\epsilon = A_c^2(E, \theta) \qquad (E.5)$$

Thus the magnitude of the analyzing power can be measured by the "right-left" asymmetry in such a double-scattering experiment. (Note that $|A_c| \leq 1$.) To get the sign of A_c an experiment is performed where carbon is used to polarize a beam of protons exactly as in the first step in the above experiment. These protons are then slowed down to very low energy (less than 10 MeV) in an absorber and allowed to scatter from He^4. The low energy p-He^4 phase shifts are well known so that the proton polarization and, therefore, the sign of A_c may be determined [23].

Unfortunately the above analysis is oversimplified, especially if the energy of the proton either before or after the carbon scattering is poorly determined. The problem arises from the fact that the

proton does not necessarily scatter elastically off of the carbon but can excite any of several nuclear levels, with each of these processes having its own cross section and analyzing power. In the present experiment the energy of the proton before the p-C scatter was quite poorly known due to the Fermi motion in deuterium. As a result of this poor resolution, the p-C scatter could have been elastic or could have proceeded via the excitation of any of the first four inelastic levels of C_{12} (with inelasticities of 4.43, 9.63, 15 and 19 MeV).*

Because of this uncertainty in exactly how the p-C scattering proceeded the best estimate that can be made for the analyzing power of a given p-C scatter is

$$A_c(T_{p'}, \theta_{p'}) = \frac{A_o(T_{p'}, \theta_{p'}) + \sum_{i=1}^{4} A_i(T_{p'}, \theta_{p'}) R_i(T_{p'} + E_i, \theta_{p'})}{(1 + \sum_{i=1}^{4} R_i(T_{p'} + E_i, \theta_{p'})} \quad . \qquad (E.6)$$

In (E.6) the following notation is used: $T_{p'}$ is the energy of the proton after the scattering as determined from its range in carbon; $\theta_{p'}$ is the angle of the scatter (see Figure 2); E_i is the energy of the i^{th} excited level of C_{12}; A_o is the analyzing power for elastic scattering and A_i is the analyzing power for the excitation of the i^{th} nuclear level; and finally, R_i is the ratio of the cross section for scattering with excitation of the i^{th} level to the cross section for

---

* There is also a contribution from the "inelastic tail" of levels above these four up to the maximum inelasticity consistent with our resolution. However, estimates of this contribution from available data indicate that it is less than the uncertainty in the A_c data for elastic scattering and for the lower inelastic levels. Therefore, this contribution is ignored in the analyzing power calculations, but it does add to the uncertainty in the proton energy.

elastic scattering. The quantity $T_{p'} + E_i$ appears because it is, of course, the energy before the scatter that matters.

The experimental data on A_o, A_i, and R_i necessary to use (E. 6) have been collected in the form of tables [46].* The tables give the experimental values at intervals of 1^o in $\theta_{p'}$ and 10 MeV in $T_{p'}$. The range covered by these tables is $4^o \leq \theta_{p'} \leq 30^o$ and 90 MeV $\leq T_{p'} \leq$ 300 MeV. For values outside of these limits the analyzing power is both small and poorly known and such events are not used in the polarization determination. The $4\text{-}6^o$ p-C scatters also have small analyzing power compared to scatters with $\theta_{p'} > 6^o$, which is fortunate considering the bias shown by one group of scanners in finding these small angle scatters (see Appendix C).

Obviously the polarization values obtained in an experiment of this nature are only as good as the knowledge of the analyzing power. There are three main sources of error in the analyzing power determination: (1) the errors in the analyzing power data in the above mentioned tables;† (2) the resolution errors in the quantities, $T_{p'}$ and $\theta_{p'}$, of which A_i and R_i are functions; and (3) the indeterminacy of the inelasticity in the p-C scatters, i.e., the error involved in having to use (E. 6) to estimate the carbon analyzing power.

---

* Actually the data on A_i for i=2, 3, 4 are not sufficient to construct the above mentioned tables. Therefore, simplifying assumptions have been made about the behavior of these A_i as functions of $T_{p'}$ and $\theta_{p'}$ on the basis of what data are available [46].

† The errors in R_i are far less ($\leq 10\%$) than those in A_i and are not considered in this estimate of the error in analyzing power.

The error in the experimental data on the carbon analyzing power averages ± .02 for elastic scatters and ± .1 for the inelastic scatters [46]. However, the values of R_i all average less than 1/5 for our kinematical region and therefore the inelastic scatters are far less important in determining the value of the analyzing power. Thus the typical error due to (1), weighted according to the importance of the data, is about .02 for each level.

The resolution in the quantities $T_{p'}$ and $\theta_{p'}$ for the various kinematical settings are given in Table 2. Using the analyzing power tables referred to above one can then see how much the analyzing power can change for changes in these variables on the order of their uncertainty.* The results of such studies show that the typical error in the analyzing power due to (2) ranges from approximately ± .035 to ± .065. The larger errors hold for bins in which a large number of events have a poor resolution in the initial trajectory.

The error from (3) can be as large as the difference between the effective analyzing power calculated using (E. 6) and the elastic analyzing power. This difference is as great as 35% for certain regions of $T_{p'}$ and $\theta_{p'}$; however, 20% (and usually less) is a more typical value for the $T_{p'}$ and $\theta_{p'}$ regions contributing most heavily to our results.

---

* This procedure is slightly complicated by the fact that events from a given kinematical "setting" contribute to several of the kinematical "bins" into which the results are divided. However, the number of events that a given setting contributes to a given bin is, of course, known and there is no difficulty in obtaining the correctly weighted uncertainty due to (2) for each bin.

The importance of inelastic p-C scatters in this experiment is indicated by Figures 40 and 41 which show the observed distributions in $\theta_{p'}$ for the $\theta_{\pi}^{CM} = 90^{o}$ and 120^{o} data plotted against both $\sigma(\theta_{p'})$, the integral over $T_{p'}$ of $\sigma_o(T_{p'}, \theta_{p'}) [1+\sum_{i=1}^{4} R_i(T_{p'}, \theta_{p'})]$, and $\sigma_o(\theta_{p'})$, the integral of $\sigma_o(T_{p'}, \theta_{p'})$.* The agreement between the data and $\sigma(\theta_{p'})$, especially when compared to the results for $\sigma_o(\theta_{p'})$, demonstrate how wrong it would be to simply ignore the inelastic scatters and use A_o, rather than the analyzing power calculated using equation (E.6), in each case.

In Section 4 the errors in the analyzing power discussed above are combined with the other relevant errors to obtain an overall systematic error for the final polarization values.

---

* These integrals are weighted according to the acceptance of our range chamber. The curves in Figures 40 and 41 incidentally indicate that the reconstruction of the $\theta_{p'}$ for each event must be free of any serious errors.

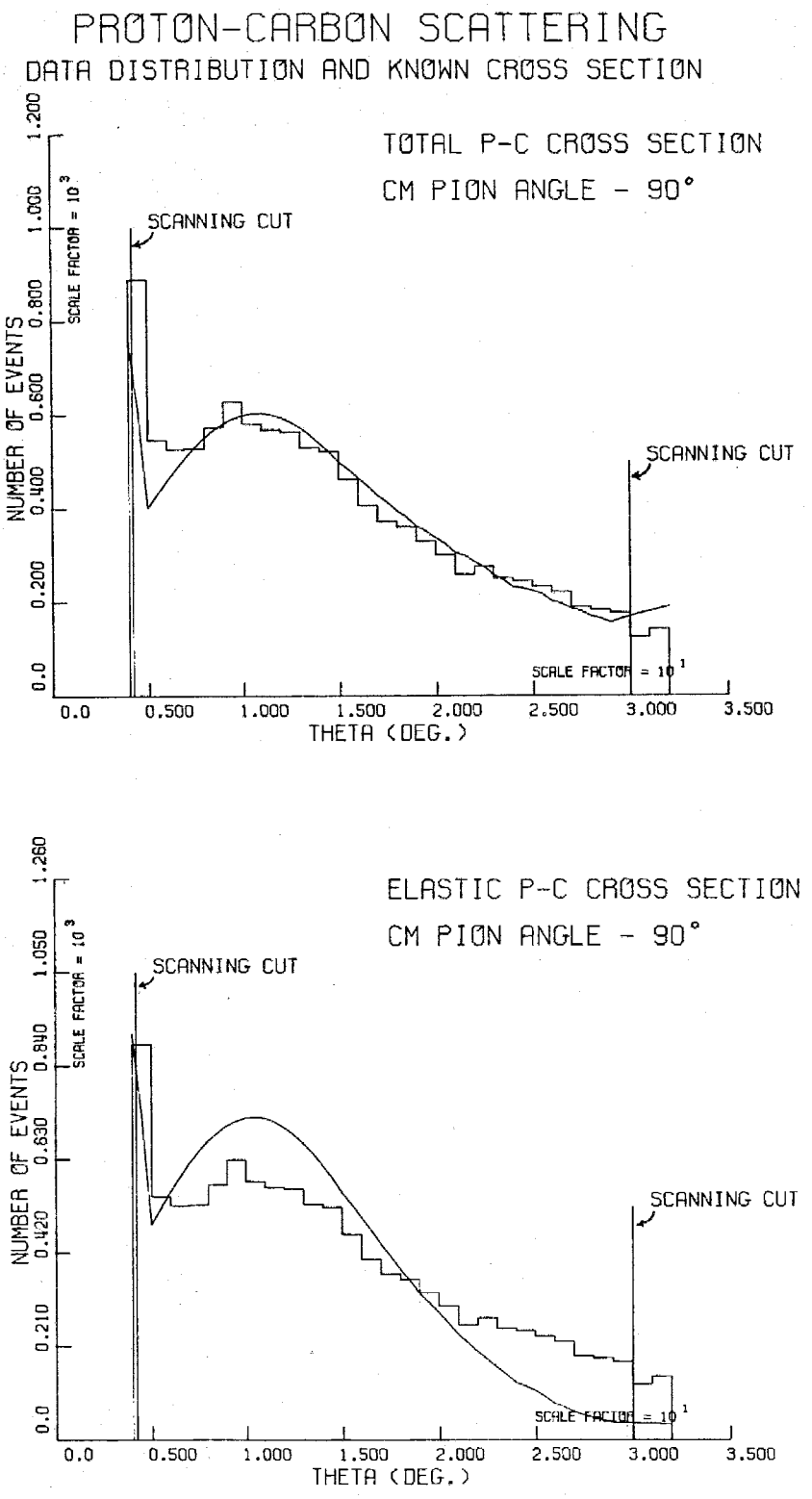
PROTON-CARBON SCATTERING
DATA DISTRIBUTION AND KNOWN CROSS SECTION
TOTAL P-C CROSS SECTION
CM PION ANGLE - 90°
SCANNING CUT
SCANNING CUT
SCALE FACTOR = 10^3
SCALE FACTOR = 10^1
NUMBER OF EVENTS
0.0
0.200
0.400
0.600
0.800
1.000
1.200
0.0
0.500
1.000
1.500
2.000
2.500
3.000
3.500
THETA (DEG.)
ELASTIC P-C CROSS SECTION
CM PION ANGLE - 90°
SCANNING CUT
SCANNING CUT
SCALE FACTOR = 10^3
SCALE FACTOR = 10^1
NUMBER OF EVENTS
0.0
0.210
0.420
0.630
0.840
1.050
1.260
0.0
0.500
1.000
1.500
2.000
2.500
3.000
3.500
THETA (DEG.)

FIGURE 40

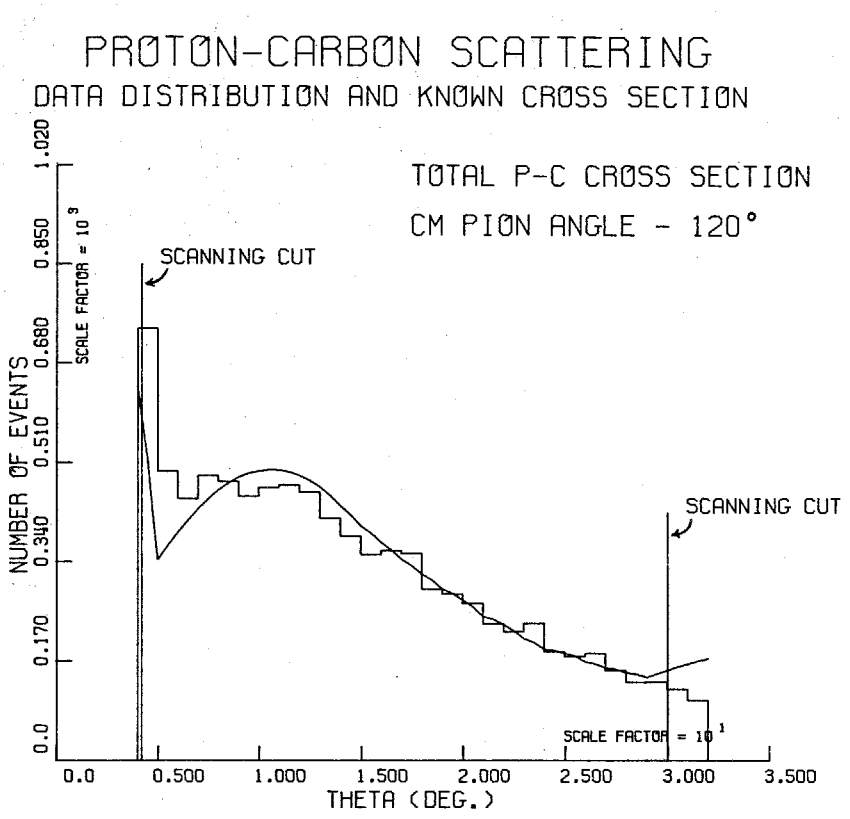
PROTON-CARBON SCATTERING
DATA DISTRIBUTION AND KNOWN CROSS SECTION
TOTAL P-C CROSS SECTION
CM PION ANGLE - 120°
SCANNING CUT
SCANNING CUT
SCALE FACTOR = 10 3
SCALE FACTOR = 10 1
NUMBER OF EVENTS
0.0
0.170
0.340
0.510
0.680
0.850
1.020
0.0
0.500
1.000
1.500
2.000
2.500
3.000
3.500
THETA (DEG.)

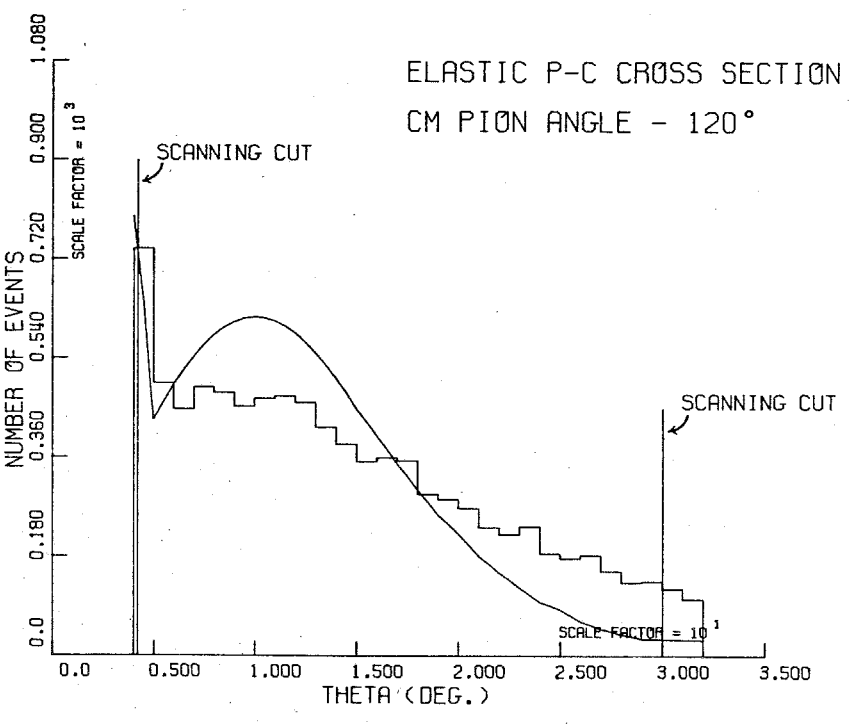
ELASTIC P-C CROSS SECTION
CM PION ANGLE - 120°
SCANNING CUT
SCANNING CUT
SCALE FACTOR = 10 3
SCALE FACTOR = 10 1
NUMBER OF EVENTS
0.0
0.180
0.360
0.540
0.720
0.900
1.080
0.0
0.500
1.000
1.500
2.000
2.500
3.000
3.500
THETA (DEG.)

FIGURE 41

APPENDIX F. PION PHOTOPRODUCTION FORMULAE

This appendix summarizes some of the formulae related to the model of pion photoproduction discussed in Section 5. Precise definitions will be given of the experimental quantities that are measured for the reaction $\gamma N \to \pi N$. Also, more details (especially quantitative expressions) are given for the contributions of the various pieces of the model to the photoproduction amplitudes. Finally, a brief discussion is given of the algorithm actually used in the χ^2 minimization step of the fitting procedure.

F.1 Experimental Observables in Pion Photoproduction

The helicity amplitudes $A_{\mu\lambda}$ defined in Section 5 are related to the S matrix for the process $\gamma N \to \pi N$ by the expression

$$S_{\mu\lambda} = \delta_{\mu\lambda} + i(2\pi)^4 \delta^4(K+P_{N_1}-Q-P_{N_2}) \frac{8\pi W}{\sqrt{16k\omega E_1 E_2}} A_{\mu\lambda} \qquad (F.1)$$

where $K=(k, \vec{k})$, $P_{N_1}=(E_1, \vec{p}_1)$, $Q=(\omega, \vec{q})$ and $P_{N_2}=(E_2, \vec{p}_2)$ are the four-momenta of the photon, initial nucleon, pion, and final nucleon respectively. W is the total energy in the CM frame and λ and μ are the initial and final helicities.

The first experimental observable, $\sigma(W, \theta)$, is just the differential cross section for an unpolarized beam and for unpolarized nucleons. With the normalization adopted in (F.1) this cross section as a function of W and of θ, the CM pion angle, is

$$\sigma(W, \theta) = \frac{1}{4} \frac{q}{K} \sum_{\text{spins}} |A_{\mu\lambda}|^2$$

$$= \frac{1}{2} \frac{q}{K} \left(|A_{\frac{1}{2}\frac{3}{2}}|^2 + |A_{\frac{1}{2}\frac{1}{2}}|^2 + |A_{-\frac{1}{2}\frac{3}{2}}|^2 + |A_{-\frac{1}{2}\frac{1}{2}}|^2 \right) . \qquad (F.2)$$

In this expression the fact that (due to parity conservation) $A_{-\mu,-\lambda}$ equals $A_{\mu,\lambda}$ within a phase* has been used.

The second observable is the recoil nucleon polarization. In the CM frame this polarization is directed along $\hat{k}\times\hat{q}$ due to parity conservation. Therefore if the coordinate system is oriented such that $\hat{k}\times\hat{q}$ is parallel to $\hat{y}$ we have, if $\hat{n} = \vec{k}\times\vec{q}/|\vec{k}\times\vec{q}|$,

$$P\hat{n} = \frac{\mathrm{Tr}(A^{+}\vec{\sigma}\cdot\hat{n}\,A)}{\mathrm{Tr}A^{+}A}\,\hat{n} \qquad (F.3a)$$

$$= \frac{1}{2}\frac{q}{k}\frac{1}{\sigma(W,\theta)}\mathrm{Tr}\;A^{+}\sigma_{y}A\;\hat{n}$$

If the matrix $A_{\mu\lambda}$ is written out, this expression gives [9]

$$P(W,\theta)\,\hat{n} = -\frac{q}{k}\frac{1}{\sigma(W,\theta)}\;\mathrm{Im}\left(A_{\frac{1}{2}\frac{3}{2}}A^{*}_{-\frac{1}{2}\frac{3}{2}} + A_{\frac{1}{2}\frac{1}{2}}A^{*}_{-\frac{1}{2}\frac{1}{2}}\right)\hat{n} \qquad (F.3b)$$

for both photon helicities ($\lambda_K = \pm 1$).

The next observable is the polarized photon asymmetry $\Sigma(W,\theta)$. If $\hat{\epsilon}_{\pm}$ are the polarization vectors for photon helicities $\lambda_K = \pm 1$ and if $\vec{k}$ is along $\hat{z}$, then for photons linearly polarized along $\hat{x}$ and $\hat{y}$ we have

$$\hat{\epsilon}_x \equiv \hat{\epsilon}_{\parallel} = -\frac{1}{\sqrt{2}}(\hat{\epsilon}_{+}-\hat{\epsilon}_{-})$$

$$\hat{\epsilon}_y \equiv \hat{\epsilon}_{\perp} = \frac{}{\sqrt{2}}(\hat{\epsilon}_{+}+\hat{\epsilon}_{-})$$

Combining the helicity amplitudes in this manner the cross sections for photons polarized along $\hat{x}$ and $\hat{y}$ are found to be

---

* This phase is given explicitly in Section 5.1.

$$\sigma_{\parallel}(W,\theta) = \tfrac{1}{2}\frac{q}{k}\left(\left|A_{\frac{1}{2}\frac{3}{2}}+A_{-\frac{1}{2}\frac{1}{2}}\right|^2+\left|A_{\frac{1}{2}\frac{1}{2}}-A_{-\frac{1}{2}\frac{3}{2}}\right|^2\right)$$

$$\sigma_{\perp}(W,\theta) = \tfrac{1}{2}\frac{q}{k}\left(\left|A_{\frac{1}{2}\frac{3}{2}}-A_{-\frac{1}{2}\frac{1}{2}}\right|^2+\left|A_{\frac{1}{2}\frac{1}{2}}+A_{-\frac{1}{2}\frac{3}{2}}\right|^2\right) \qquad \text{(F4.a)}$$

respectively. Then the polarized photon asymmetry, [9]

$$\Sigma(W,\theta) \equiv \frac{\sigma_{\perp}-\sigma_{\parallel}}{\sigma_{\perp}+\sigma_{\parallel}} = \frac{q}{k}\frac{1}{\sigma(\theta)}\,\mathrm{Re}\left(A_{\frac{1}{2}\frac{3}{2}}\,A^{*}_{-\frac{1}{2}\frac{1}{2}} - A_{\frac{1}{2}\frac{1}{2}}A^{*}_{-\frac{1}{2}\frac{3}{2}}\right) \qquad \text{(F.4.b)}$$

The other experimentally measured quantity in pion photoproduction is the polarized target asymmetry

$$T(W,\theta) \equiv \frac{\sigma_{+}-\sigma_{-}}{\sigma_{+}+\sigma_{-}} = \frac{q}{k}\frac{1}{\sigma(W,\theta)}\,\mathrm{Im}\left(A_{\frac{1}{2}\frac{3}{2}}A^{*}_{-\frac{1}{2}\frac{1}{2}}+A_{-\frac{1}{2}\frac{3}{2}}A^{*}_{-\frac{1}{2}\frac{1}{2}}\right)$$

where $\sigma_{\pm}$ are the cross sections for the target nucleon polarized along $\pm(\hat{k}\times\hat{q})$. Unfortunately no data of this type exist as yet for the reaction $\gamma n \to \pi^- p$.

F.2 Helicity Amplitudes and Elements

In Section 5.1 the partial wave decomposition of the helicity amplitudes was given in terms of helicity "coefficients," $a_{\mu\lambda}$, (see Equation (5.2)). The helicity elements $A_{\ell\pm}$, $B_{\ell\pm}$, were then defined in terms of these coefficients by Equation (5.3). Combining these two equations and expressing the $d^{j}_{\lambda\mu}$'s in terms of the derivatives of Legendre polynomials, we obtain the relations between the helicity amplitudes and elements. Namely,

$$A_{\frac{1}{2}\frac{3}{2}}(\theta,\phi) = \frac{1}{\sqrt{2}}\,e^{i\phi}\sin\theta\cos\frac{\theta}{2}\sum_{\ell=1}^{\infty}(B_{\ell+}-B_{(\ell+1)-})(P''_{\ell}-P''_{\ell+1})$$

$$A_{\frac{1}{2}\frac{1}{2}}(\theta,\phi) = \sqrt{2}\cos\frac{\theta}{2}\sum_{\ell=0}^{\infty}(A_{\ell+}-A_{(\ell+1)-})(P'_{\ell}-P'_{\ell+1}) \qquad \text{(F.5)}$$

(continued)

$$F_3 = g \frac{qk\, z_2}{W z_1} \left(\frac{e_\pi}{t-m_\pi^2} - \frac{e_2}{\mu - M_2^2} \right)$$

$$F_4 = -g \frac{q^2 z_1}{W z_2} \left(\frac{e_\pi}{t-m_\pi^2} - \frac{e_2}{\mu - M_2^2} \right)$$

The kinematical factors in these equations are related to the four-vectors of Section F.1 in the following manner

$$\begin{aligned} s &\equiv (K+P_{N_1})^2 \\ t &\equiv (K-Q)^2 \\ \mu &\equiv (K-P_{N_2})^2 \\ z_1 &\equiv (E_1+M_1)^{\frac{1}{2}} \quad \text{and} \quad z_2 \equiv (E_2+M_2)^{\frac{1}{2}} \end{aligned} \tag{F.8}$$

Also, e_π, e_1 and e_2 are the charges of the pion, initial nucleon, and final nucleon respectively. Finally, $g = \frac{G_{\pi^-}}{4\pi}$ with $G_{\pi^-} = \sqrt{2}\, G_{\pi^0 p} = -\sqrt{2}\, G$ (where $\frac{G^2}{4\pi} = 14.7$). The use of the minimal electromagnetic coupling without any anomalous magnetic moments is the reason for calling these the "electric" Born terms.

As stated in Section 5.1, no attempt is made to decompose the $(A_{\mu\lambda})_{\text{Born}}$ in order to get the contributions to the individual $A_{\ell\pm}$ and $B_{\ell\pm}$ of the Born terms. However, for convenience in comparing the Born contribution to the other parts of the model, Table 13 gives this decomposition for the reaction $\gamma n \to \pi^- p$ at several values of k_{LAB}.

F.4 The Resonances

Recall (from Section 5.1) that a resonance of mass W_o, width Γ_o, and spin-parity J^P will contribute to either the $A_{\ell+}$ (and $B_{\ell+}$ if $J \geq \frac{3}{2}$) or the $A_{\ell-}$ (and $B_{\ell-}$ if $J \geq \frac{3}{2}$) helicity element depending on the parity since $P = -(-1)^{\ell}$ and $\ell\pm$ means $J = \ell \pm \frac{1}{2}$.

The form of this contribution is parameterized by a Breit-Wigner dependence. Thus the contribution of, say, the $D_{13}(1510)$ to the B_{2-} helicity element for the reaction $\gamma n \to \pi^- p$ at a CM energy W is given by [9]

$$B_{2-}(W)_{RES} = B^-[D_{13}(1510)]\left(\frac{k_o q_o}{kq}\right)^{\frac{1}{2}} \frac{W_o \Gamma^{\frac{1}{2}} \Gamma_\gamma^{\frac{1}{2}}}{W_o^2 - W^2 - iW_o\Gamma}$$

with

$$\Gamma = \Gamma_o \left(\frac{q}{q_o}\right)^{2\ell+1} \left(\frac{q_o^2 + X^2}{q^2 + X^2}\right)^{\ell} \qquad \text{(F.9)}$$

and

$$\Gamma_\gamma = \Gamma_o \left(\frac{k}{k_o}\right)^{2j_\gamma} \left(\frac{k_o^2 + X^2}{k^2 + X^2}\right)^{j_\gamma}$$

In these formulae: k, q, and W are the photon momentum, pion momentum, and the total energy in the CM frame (and k_o, q_o, and W_o are their values at resonance); j_γ and the threshold factor X are parameters describing each particular resonance whose values are given in Table 4; ℓ is the orbital momentum of the final πN state (equal to 2 in the present case); and finally, $B^-[D_{13}(1510)]$ is the "coupling" of the $D_{13}(1510)$ resonance to the helicity 3/2 initial state of the reaction $\gamma n \to \pi^- p$. Analogous formulae hold for the contribution of the $D_{13}(1510)$ to the A_{2-} helicity element and for the contributions of the other resonances in Table 4 to the various helicity elements.

Figure 42 shows the Real (Re) and Imaginary (Im) parts of the $(B_{2-})_{RES}$ helicity element.

The couplings $A^-[N^*]$ and $B^-[N^*]$ for the $I = 1/2$ nucleon resonances[†] to the reaction $\gamma n \to \pi^- p$ are the most interesting quantities determined in the analysis described in Section 5. They can be related to the amplitudes $A^N_{\frac{1}{2}}$ and $A^N_{\frac{3}{2}}$ for the decay of these resonances into a neutron and a photon in helicity states 1/2 and 3/2 respectively, which are the numbers generally calculated in quark models of the photoexcitation of nucleon isobars. The relations among $A^N_{\frac{1}{2}}$, $A^N_{\frac{3}{2}}$, $A^-[N^*]$ and $B^-[N^*]$ are given by [3]

$$A^-[N^*] = \mp\left[\frac{1}{\pi}\,\frac{q}{k}\,\frac{1}{(2J+1)}\,\frac{M_n}{W_o}\,\frac{\Gamma_\pi}{\Gamma_o}\,\frac{1}{\Gamma_o}\right]^{\frac{1}{2}} C^-_{\pi N}\, A^N_{\frac{1}{2}}$$

and

$$B^-[N^*] = \pm\left[\frac{1}{\pi}\,\frac{q}{k}\,\frac{1}{(2J+1)}\,\frac{M_n}{W_o}\,\frac{\Gamma_\pi}{\Gamma_o}\,\frac{1}{\Gamma_o}\right]^{\frac{1}{2}} \times \qquad \text{(F.10)}$$

$$\times\ [16/((2J-1)(2J+3))]^{\frac{1}{2}}\ C^-_{\pi N}\, A^N_{\frac{3}{2}}$$

Most of the quantities in these equations have already been defined above. Γ_π/Γ_o is the branching ratio of the resonance into πN and $C^-_{\pi N}$ is the Clebsch-Gordan coefficient for $N^* \to \pi^- p$ which equals $-\sqrt{\frac{2}{3}}$ for $I = 1/2$ resonances and $\sqrt{\frac{1}{3}}$ for $I = 3/2$ resonances.

[†] For $I=3/2$ resonances $B^-[N^*] = B^+[N^*]$ and $A^-[N^*] = A^+[N^*]$ where B^+ and A^+ are the couplings for π^+ photoproduction. In these cases the values determined in a recent fit [15] to π^+ photoproduction data are used since these data are far more numerous and generally better in quality than the π^- data.

F.5 The Background Terms

The final contribution to the helicity elements and the one which is actually varied in order to minimize the χ^2 in a given fit to the experimental data is the background contribution. The background contributions to each helicity element ($\mathrm{Re}A_{\ell\pm}$, $\mathrm{Im}A_{\ell\pm}$, $\mathrm{Re}B_{\ell\pm}$, and $\mathrm{Im}\,B_{\ell\pm}$) are parameterized by specifying their values at several reference energies $W_1, W_2, \ldots, W_N$.[†] The initial value of a particular background, say the $\mathrm{Re}\,A_{o+}$, for an energy W such that $W_{n-1} < W < W_n$ is obtained from its values at these reference energies by the following interpolation

$$\mathrm{Re}\,A_{o+}(W)_{BACK} = \eta(W)\,[(1-X)A_1 + X\,A_2] \qquad (F.11)$$

with $\eta(W) = q(W)^{\ell}/[q(W)^2 + (0.35)^2]^{\frac{1}{2}}$

$$X = \frac{W-W_{n-1}}{W_n-W_{n-1}}$$

and

$$A_1 = \frac{(W-W_{n-1})(W-W_n)}{(W_{n-1}-W_{n-2})(W_n-W_{n-2})}\left(\frac{\mathrm{Re}\,A_{o+}(W_{n-2})}{\eta(W_{n-2})}\right) +$$

$$+\frac{(W-W_{n-2})(W-W_n)}{(W_{n-1}-W_{n-2})(W_{n-1}-W_n)}\left(\frac{\mathrm{Re}A_{o+}(W_{n-1})}{\eta(W_{n-1})}\right) +$$

$$+\frac{(W-W_{n-2})(W-W_{n-1})}{(W_n-W_{n-2})(W_n-W_{n-1})}\left(\frac{\mathrm{Re}A_{o+}(W_n)}{\eta(W_n)}\right)$$

[†] The values of these reference energies for the fits described in Section 5 are given in Table 5 where the background contributions to the final solution are summarized.

and A_2 given by a similar expression only with each index incremented by one. q(W) is the pion momentum. If $W \leq W_2$, n = 3 and x = 0.0. If $W \geq W_{N-1}$, n = N-1 and x = 1.0. The computer program that does the fitting then varies this initial value as well as that of all of the other background contributions in order to obtain the best fit to the data at this energy.

In the end, however, it is the initial values of these backgrounds which determine the solution. That is, when a set of initial values for all the background elements has been obtained which gives a satisfactory fit at each energy, this is the final solution. No variation is made in this final solution when calculating the final values for the experimental observables. One weakness of the parameterization used is that it does not extrapolate well to energies outside of the range covered by the present fits.

F.6 The Fitting Algorithm

In the analysis described in Section 5.2 a well known algorithm [22] for non-linear least-square fitting was used. The goal was to fit the experimental data points, X_i,* in terms of helicity amplitudes which are in turn functions of the background helicity elements $A_{\ell\pm}$ and $B_{\ell\pm}$. Thus, we were trying to fit the quantities X_i as non-linear functions, f_i, of the complex numbers $A_{\ell\pm}$ and $B_{\ell\pm}$.†

---

* X_i can be a cross section, a recoil nucleon polarization, or a polarized beam asymmetry.

† The $A_{\ell\pm}$ and $B_{\ell\pm}$ of course also contain contributions from the Born terms and the resonances but these are constant as far as the χ^2 minimization procedure is concerned.

One possible fitting procedure would be to linearize the dependence on the A's and B's by expanding each function f_i in a Taylor's series in these parameters and truncating the series after the second term. The χ^2 would then be minimized by setting its derivitives equal to zero. This procedure is sensible only if the parameters are close to their final values and therefore is most useful in the final stages of the fitting. We will call this "Method 1" and briefly outline how it works.

Let X_i be the experimental points with their errors σ_i. Also, let f_i be the theoretical expression for the i^{th} data point, depending on the variables $a_1, \ldots, a_n$ which have initial values $a_1^o, \ldots, a_n^o$. (a_i can stand for any one of the quantities $\mathrm{Re}\,A_{\ell\pm}$, $\mathrm{Im}A_{\ell\pm}$, $\mathrm{Re}B_{\ell\pm}$, or $\mathrm{Im}B_{\ell\pm}$ for any $j \leq \frac{7}{2}$). Then for N data points

$$\chi^2 = \sum_{i=1}^{N} \frac{1}{\sigma_i^2} (X_i - f_i)^2$$

$$= \sum_{i=1}^{N} \frac{1}{\sigma_i^2} \left\{ X_i - f_i(a_1^o, \ldots a_n^o) - \sum_{j=1}^{n} \frac{\partial f_i}{\partial a_j}\Big|_{a_j^o} (a_j - a_j^o) - \sum_{j=1}^{n}\sum_{k=1}^{n} \frac{1}{2} \frac{\partial^2 f_i}{\partial a_j \, \partial a_k}\Big|_{a_j^o, a_k^o} \times \right. \tag{F.12}$$

$$\left. \times \quad (a_j - a_j^o)(a_k - a_k^o) - \ldots \right\}^2$$

If $f_i(a_1^o, \ldots a_n^o) \equiv f_i(0)$ and $\delta a_j \equiv (a_j - a_j^o)$, the minimization condition becomes

$$\frac{\partial \chi^2}{\partial a_\ell} = 0 = \sum_{i=1}^{N} \frac{2}{\sigma_i^2} \left\{ (X_i - f_i(0)) \left(- \frac{\partial f_i}{\partial a_\ell}\Big|_{a_\ell^o} \right) \right. \tag{F.13}$$

$$\left. + \sum_{j=1}^{n} \left(\frac{\partial f_i}{\partial a_\ell}\Big|_{a_\ell^o} \frac{\partial f_i}{\partial a_j}\Big|_{a_j^o} - (X_i - f_i(0)) \frac{\partial^2 f_i}{\partial a_\ell \partial a_j}\Big|_{a_j^o, a_\ell^o} \right) \cdot \delta a_j + \ldots \right\}$$

Keeping only the terms linear in $\delta \vec{a}_j$, i.e., using our linearization approximation, this condition becomes

$$\sum_{i=1}^{N} \frac{2}{\sigma_i^2} (X_i - f_i(0)) \left.\frac{\partial f_i}{\partial a_\ell}\right|_{a_i^o} = \sum_{i=1}^{N} \sum_{j=1}^{n} \frac{2}{\sigma_i^2} \left(\left.\frac{\partial f_i}{\partial a_j}\right|_{a_j^o} \left.\frac{\partial f_i}{\partial a_\ell}\right|_{a_\ell^o} - (X_i - f_i(0)) \left.\frac{\partial^2 f_i}{\partial a_j \partial a_\ell}\right|_{a_j^o, a_\ell^o} \right) \delta a_j$$

or in matrix notation

$$C_\ell = D_{\ell j}\, \delta a_j \qquad \text{(F.14a)}$$

where $$C_\ell \equiv \sum_{i=1}^{N} \frac{2}{\sigma_i^2} (X_i - f_i(0)) \left.\frac{\partial f_i}{\partial a_\ell}\right|_{a_\ell^o} \qquad \text{(F.14b)}$$

and $$D_{\ell j} \equiv \sum_{i=1}^{N} \frac{2}{\sigma_i^2} \left(\left.\frac{\partial f_i}{\partial a_j}\right|_{a_j^o} \left.\frac{\partial f_i}{\partial a_\ell}\right|_{a_\ell^o} - (X_i - f_i(0)) \left.\frac{\partial^2 f_i}{\partial a_j\, \partial a_\ell}\right|_{a_j^o, a_\ell^o} \right).$$

Equation (F14.a) can then be solved for δa_j.

By repeating this procedure, each time letting $a_j^o \rightarrow a_j^o + \delta a_j$, one hopes to approach the best solution (i.e., the minimum in χ^2) but unless you are already close this approach can be very slow.

Another complementary method which will be called "Method 2" is the gradient search. It is very efficient when the a_j are far from their "best" values but becomes less so as a solution is approached. Instead of trying to move <u>directly</u> to the minimum in χ^2 as method 1 does, method 2 simply moves <u>toward</u> it proceeding along the path of steepest negative gradient. Along this path δa_j is directly proportional to $-\frac{\partial \chi^2}{\partial a_j}$. It is only a matter of choosing the constant of proportionality, d, such that a change $\delta a_j = -d\left(\frac{\partial \chi^2}{\partial a_j}\right)$ causes the χ^2 to decrease. If δa_j is small equations (F.13) and

(F.14b) show $\frac{\partial \chi^2}{\partial a_j} \simeq -C_j$. Therefore, for small d method 2 just uses $\delta a_j = dC_j$. Inserting scale factors $(D^{-1})_{jj}$ into this relation has no effect, so method 2 can be said to seek the minimum in χ^2 via changes in the parameters given by

$$\delta a_j = (D^{-1})_{jj} \, d C_j \qquad \text{(F.15)}$$

where D_{jj} and C_j are defined above.

The algorithm actually used in the present fitting [22] combined methods 1 and 2 to obtain a method that would (hopefully!) be efficient both near to and far from the solution. Thus, the changes in the parameters for each iteration were obtained from the equation

$$\delta a_j = (G^{-1})_{j\ell} \, C_\ell \qquad \text{(F.16)}$$

where

$$G_{j\ell} = D_{j\ell} + F_{j\ell}$$

and

$$F_{j\ell} = b \, \delta_{j\ell} \, D_{j\ell} \qquad (b = 1/d)$$

The elements of the diagonal matrix F determined whether method 1 or 2 dominated the fitting procedure. If $b \ll 1$ the algorithm was essentially that of method 1 and if $b \gg 1$ it was essentially that of method 2.

The actual fitting procedure used was as follows:

(1) Compute χ^2 using the initial parameters a_j^o and set $b = 0.1$.

(2) Compute C_ℓ, $D_{j\ell}$, and $F_{j\ell}$ from the parameters a_j^o and the current value of b.

(3) Solve for δa_j and compute χ^2 using $a_j = a_j^o + \delta a_j$;

If $\chi^2(a_j) > \chi^2(a_j^o)$, increase b by a factor of 10 and go to step (2);

If $\chi^2(a_j) \leq \chi^2(a_j^o)$, let $a_j^o \rightarrow a_j^o + \delta a_j$, decrease b by a factor of 10 and go to step (2);

If $\chi^2(a_j) \leq \chi^2(a_j^o)$ and the change δa_j in each parameter a_j is less than the error in this parameter calculated via the error matrix, the solution has converged.

Therefore, if the preceding step seemed to have gone in the wrong direction, the algorithm stressed method 2 in order to get the solution headed in the right direction again. As long as the χ^2 continued to decrease, method 1 was stressed. In practice it was found that if the solution had not converged after three or four iterations, it generally went into an unstable loop alternating between bigger and smaller values of χ^2. In this case one could only hope that when the changes indicated by the results of the current iteration were made the new set of parameters would give a better convergence. This was always the case unless one of the resonances had a coupling value very different from the one sought by the data in which case the unstable solutions in the region of this resonance were a convenient indication of this fact.

Table 13: Born Approximation

The helicity element projections of the electric Born terms (Figure 19 (b)) for the reaction $\gamma n \rightarrow \pi^- - p$ are given at several energies for comparison to the background terms in Table 5. Re stands for the real part. The imaginary parts are, of course, zero. The units are $\mu b^{\frac{1}{2}}$ and W stands for the CM energy.

k_{lab}(Bev)	0.400	0.600	0.800	1.000	1.200
W(Bev)	1.277	1.416	1.543	1.660	1.770
Re A_{0+}	-2.575	-2.147	-1.900	-1.728	-1.598
Re A_{1-}	-1.466	-1.497	-1.456	-1.398	-1.340
Re A_{1+}	-0.046	0.085	0.160	0.207	0.239
Re B_{1+}	-1.392	-1.442	-1.441	-1.425	-1.404
Re A_{2-}	0.313	0.340	0.352	0.358	0.362
Re B_{2-}	-1.231	-1.363	-1.394	-1.395	-1.382
Re A_{2+}	-0.139	-0.129	-0.124	-0.123	-0.124
Re B_{2+}	-0.194	-0.187	-0.167	-0.146	-0.126
Re A_{3-}	0.055	0.031	0.006	-0.016	-0.034
Re B_{3-}	-0.161	-0.169	-0.156	-0.139	-0.121
Re A_{3+}	-0.050	-0.049	-0.036	-0.024	-0.014
Re B_{3+}	-0.068	-0.081	-0.085	-0.086	-0.087
Re A_{4-}	0.042	0.048	0.048	0.048	0.049
Re B_{4-}	-0.056	-0.083	-0.080	-0.083	-0.084

Table 14

Experiments Used in the π^- Fits

The following list gives the plotting symbol used in referring to various experiments in Figures 20-26. The type of data* and the reference are also given for each experiment.

Plotting Symbol	Type of Data	Reference
B	σ	M. Beneventano, F. de Notaristefani, P. Monacelli, L. Paoluzi, F. Sebastiani and M. Severi, Nuovo Cimento Letters, 1, 113 (1968).
G	σ	G. von Holtey, G. Knop, H. Stein, J. Stümpfig and H. Wahlen, "The π^-/π^+ Ratio of Photoproduction on Deuterium for Energies between 240 and 440 MeV," Bonn Preprint PIB 1-166 (1972).
I	σ	Gerry Neugebauer, Walter Wales, and R. L. Walker, Phys. Rev. 119, 1726 (1960).
J	σ	A. Ito, R. Loe, E. C. Loh, A. Ramanauskas, D. Ritchie, and W. Schmidt, Phys. Rev. Letters, 24, 687 (1970).
M	σ	Gerhard Knies, Private Communication on ABHHM-Collaboration data.
N	σ	Fumihiko Takasaki, "Negative Pion Photoproduction off Neutron at 180° in the Energy Range between 300 and 1200 MeV," Tokyo Experimental Report (Thesis), INS-J-126 (1971).
S	σ	P. L. Walden, Private Communication as well as references [21] and [22].
R	A	J. Alspector, D. Fox, D. Luckey, C. Nelson, L. S. Osborne, G. Tarnopolsky, Z. Bar-Yam, J. de Pagter, J. Dowd, W. Kern, and S. M. Matin, Phys. Rev. Letters 28, 1403 (1972).
T	A	Kunitaka Kondo, Tetsuji Nishikawa, Toshio Suzuki, Koji Takikawa, Hajime Yoshida, Yoshitaka Kimura and Masaaki Kobayashi, JPSJ 29, 13 (1970).

* σ refers to cross section or ratio data, A to photon asymmetry data, and P to recoil polarization data.

Table 14 (Continued)

Plotting Symbol	Type of Data	Reference
U	A	F. F. Liu, D. J. Drickey, and R. F. Mozley, Phys. Rev. 136, B1183 (1964).
Q	P	M. Beneventano, S. d'Angelo, F. de Notaristefani, P. Monacelli, L. Paoluzi, F. Sebastiani, M. Severi and B. Stella, Nuovo Cimento Letters 3, 840 (1970).
V	P	Present Experiment
X	P	J. R. Kenemuth and P. C. Stein, Phys. Rev. 129, 2259 (1963).

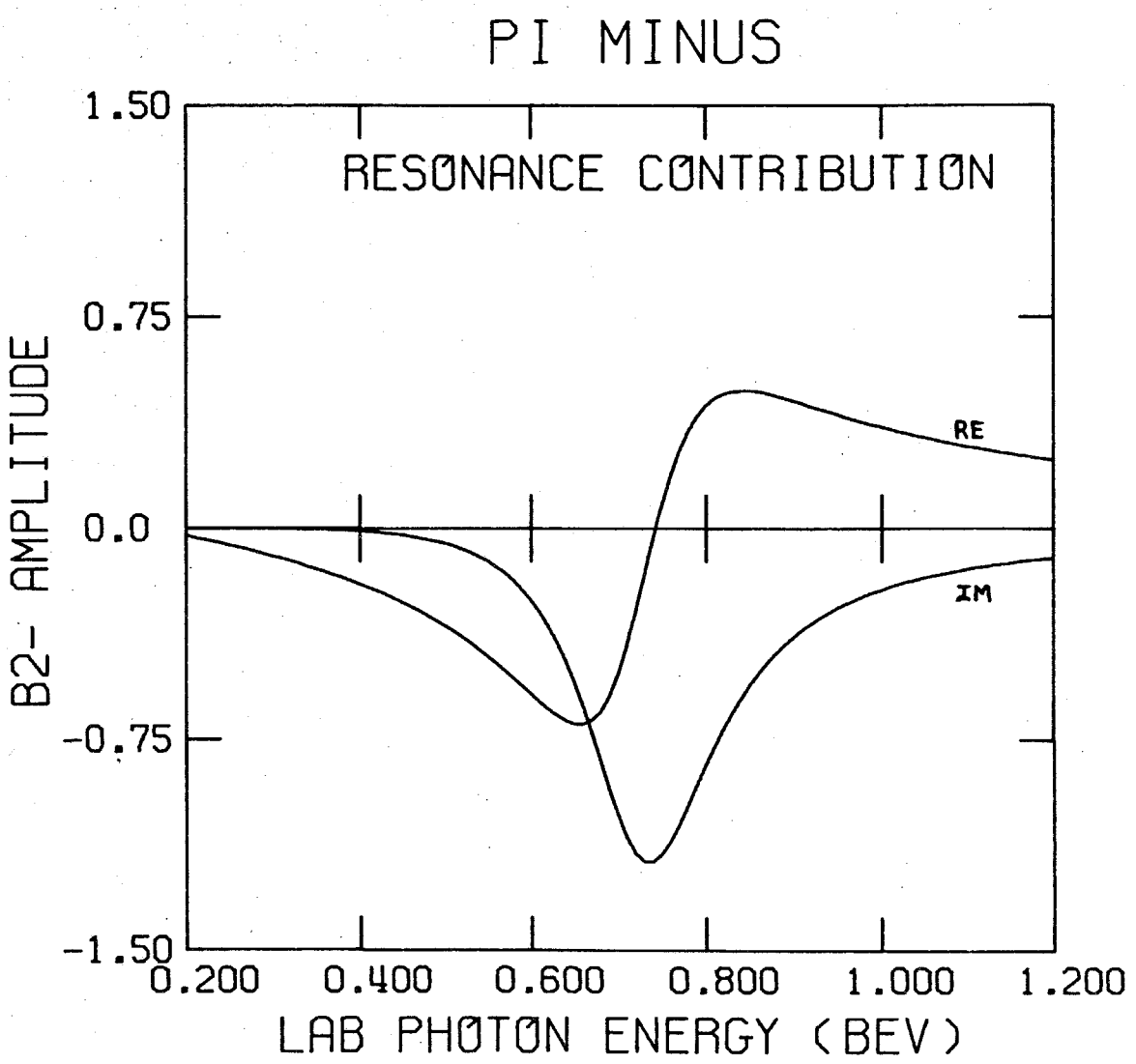
PI MINUS
RESONANCE CONTRIBUTION
1.50
0.75
0.0
-0.75
-1.50
B2- AMPLITUDE
RE
IM
0.200
0.400
0.600
0.800
1.000
1.200
LAB PHOTON ENERGY (BEV)

FIGURE 42

REFERENCES

1. D. Faiman and A. W. Hendry, Phys. Rev. 173, 1720 (1968) and Phys. Rev. 180, 1572 (1969).

2. L. A. Copley, G. Karl, and E. Obryk, Physics Letters 29B, 117 (1969).

3. R. L. Walker, in International Symposium on Electron and Photon Interactions at High Energies, Liverpool, England, 1969, edited by D. W. Braben and R. E. Rand (Daresbury Nuclear Physics Laboratory, Daresbury, Lancashire, England, 1970).

4. R. P. Feynman, M. Kislinger, and F. Ravndal, Phys. Rev. D3, 2706 (1971).

5. Y. Fujimoto and H. Miyazawa, Progr. Theoret. Phys. 5, 1052 (1950).

6. K. A. Brueckner and K. M. Case, Phys. Rev. 83, 1141 (1951).

7. M. Gourdin and Ph. Salin, Nuovo Cimento 27, 193 (1963).

8. Y. C. Chau, N. Dombey, and R. G. Moorhouse, Phys. Rev. 163, 1632 (1967).

9. R. L. Walker, Phys. Rev. 182, 1729 (1969).

10. G. Höhler and W. Schmidt, Ann. Phys. (N.Y.) 28, 34 (1964).

11. A. Donnachie and G. Shaw, Ann. Phys. (N.Y.) 37, 333 (1966).

12. F. A. Berends, A. Donnachie, and D. L. Weaver, Nucl. Phys. B4, 54 (1967).

13. A. Donnachie and G. Shaw, Daresbury Report, DNPL/P79 (1971).

14. R. G. Moorhouse, H. Oberlack, and A. H. Rosenfeld, Berkeley Preprint, LBL-1590 (1973).

15. W. J. Metcalf and R. L. Walker, Caltech Preprint, Calt-68-425 (1974).

16. R. L. Anderson and R. Prepost, Phys. Rev. Letters 23, 46 (1969).

17. J. J. Sakurai, Invariance Principles and Elementary Particles (Princeton University Press, Princeton, New Jersey, 1964).

References (Continued)

18. Gunnar Källén, Elementary Particle Physics (Addison-Wesley Publishing Company, Inc., Reading, Massachusetts, 1964).

19. H. G. Hilpert, et al., Nucl. Phys. B8, 535 (1968).

20. B. Musgrave, in Proceedings of Conference on Phenomenology in Particle Physics, California Institute of Technology, Pasadena, California, 1971, edited by C. B. Chiu, G. C. Fox, and J. G. Hey (California Institute of Technology, Pasadena, California, 1971).

21. P. L. Walden, Ph.D. Thesis, California Institute of Technology (1972).

22. P. E. Scheffler, Ph.D. Thesis, California Institute of Technology (1972).

23. B. D. Winstein, Ph.D. Thesis, California Institute of Technology (1970).

24. W.S.C. Williams, An Introduction to Elementary Particles (Academic Press, New York, 1971).

25. R. J. Glauber, Phys. Rev. 100, 242 (1955); see also Reference 20.

26. W. Franco and R. J. Glauber, Phys. Rev. 142, 1195 (1966) and Phys. Rev. 156, 1685 (1967).

27. Nathan W. Dean, Phys. Rev. Letters, 27, 276 (1971).

28. David I. Julius, Nucl. Phys., B27, 269 (1971).

29. Kirk McDonald, 'Properties of Final State Polarization in the Reaction $\gamma n \rightarrow p \pi^-$', Caltech Internal Report, CTSL-50 (1970).

30. J. R. Kenemuth and P. C. Stein, Phys. Rev. 129, 2259 (1963).

31. M. Beneventano, S. d'Angelo, F. de Notaristefani, P. Monacelli, L. Paoluzi, F. Sebastiani, M. Severi, and B. Stella, Nuovo Cimento Letters 3, 840 (1970).

32. R. G. Moorhouse and W. A. Rankin, Nucl. Phys. B23, 181 (1970).

33. A. Proia and F. Sebastiani, Nuovo Cimento Letters 3, 483 (1970).

References (Continued)

34. R. C. E. Devenish, R. H. Lyth, and W. A. Rankin, Daresbury Report, DNPL/P109 (1972).

35. M. Jacob and G. C. Wick, Ann. Phys. (N.Y.) 7, 404 (1959).

36. Riccardo Levi-Setti and Thomas Lasinski, Strongly Interacting Particles (The University of Chicago Press, Chicago, Illinois, (1973)).

37. K. M. Watson, Phys. Rev. 95, 228 (1954)

38. R. L. Walker, Private Communication. Prof. Walker in turn acknowledges the aid of Jon Mathews for showing him this useful technique.

39. D. L. Katyal and A. N. Mitra, Phys. Rev. D1, 338 (1970).

40. C. A. Heusch, C. Y. Prescott, L. S. Rochester, and B. D. Winstein, Phys. Rev. Letters 25, 1381 (1970).

41. H. A. Thiessen, Ph.D. Thesis, California Institute of Technology (1967).

42. F. B. Wolverton, Ph.D. Thesis, California Institute of Technology (1968).

43. E. D. Bloom, Ph.D. Thesis, California Institute of Technology (1967).

44. E. Fett, in Methods in Subnuclear Physics, Vol. I, edited by M. Nikolic (Gordon and Breach, New York, 1968).

45. P. L. Walden, Private Communication.

46. W. A. McNeely, Jr., 'Proton Polarization in the Scattering of 90 to 300 MeV Protons from C^{12}', Caltech Internal Report, CTSL-30 (1967).